FORENSIC CHARACTERIZATION OF RF CIRCUITS

A Dissertation

Submitted to the Faculty

of

Purdue University

by

Anthony Frank Martone

In Partial Fulfillment of the

Requirements for the Degree

of

Doctor of Philosophy

December 2007

Purdue University

West Lafayette, Indiana

To my mother, Susanne Martone. Without her guidance and steadfast belief in me, this document would not have been written.

ACKNOWLEDGMENTS

During the past five years at Purdue University, graduate school has been an exciting and challenging experience. I would like to take this opportunity to thank those who have provided support, encouragement, and friendship.

My advisor Professor Edward J. Delp has been a mentor and motivator during my time at Purdue University. I attribute my success to his ongoing encouragement and challenging approach to learning. Professor Delp's repeated appeals for me to "think like a scholar" and not like an "undergraduate" has finally come to realization, though the journey has seemed long at times. Special thanks for his patience, guidance, and assistance with writing this dissertation. To him, I owe my sincere gratitude.

I would like to thank my committee members, Professor Charles Bouman, Professor Michael Zoltowski, and Professor Zygmunt Pizlo for their guidance and advice. I would also like to thank Professor DeCarlo for his detailed teaching of "Lumped System Parameters" and jovial humor, Professor Mireille (Mimi) Boutin for her excellent coverage of "Pattern Recognition," and Professor Mark Bell for his insightful lessons on "Radar Systems."

I would like to thank the research group of the SIAMES project. Special thanks to Professor Steer, Professor Gard, Professor Chappell, Greg Mazzaro, Andrew Christianson, and Justin Henrie for their research collaboration. Special thanks to Dr. Dev Palmer and ARO for supporting this research.

I would like to thank the microwave branch at ARL for the summer internship opportunity. I learned much during my internship and have applied that knowledge to this research. Special thanks to Karl Kappra, Ken Ranney, Marc Ressler, and Brian Stanton.

I would like to thank my office-mates and friends at Purdue University: Dr. Eugene Lin, Dr. Cuneyt Taskiran, Dr. Yuxin (Zoe) Liu, Dr. Hyung Cook Kim, Dr.

Jinwha Yang, Dr. Sahng-Gyu Park, Dr. Zhen Li, Dr. Yajie Sun, Dr. Greg Cook, Dr. Hwayoung Um, Dr. Josep Predes, Dr. Thomas Talavage, Aravind Mikkilineni, Jennifer Talavage, Limin Liu, Ashok Mariappan, Hakeem Ogunleye, Deen King-Smith, Golnaz Abdollahian, Fengging (Maggie) Zhu, Carlos Wang, Ying Chen, Ka Ki Ng, Liang Liang, Nitin Khanna, Anand Mariappan, Marc Bosch, Oriol Guitart Pla, Rafael Villoria, Pau Sabria, Alex Lipka, Simone Caroti, and Gioia Massa. Special thanks to Nitin Khanna, Ying Chen, Maggie Zhu, and Golnaz Abdollahian for their help in depositing the thesis. Special thanks to Dr. Eugene Lin, Dr. Cuneyt Taskiran, and Aravind Mikkilineni for their camaraderie in the trenches of EE-32 and the VIPER lab. Special thanks to Alex Lipka, Simone Caroti, and Gioia Massa for their friendship and support.

I would especially like to thank all my family for their love and support. Thanks to Héctor, Tara, Niklas, and René Polanco for their support and philosophy of why engineers are inspired. Thanks to Ginger and Terry Monson for their ongoing encouragement and support. Special thanks to my parents, Susanne and Frank Martone. My father has always provided friendship, love, and support during these challenging years at Purdue and for which I am eternally grateful. My mother always encouraged me to “follow my dreams” and “never give up.” This dream has taken a long time to follow, but, WE DID IT! Most importantly, I would like to thank my wife Lindsey (Pepper) Martone. Throughout these five years at Purdue University, Pepper has provided me with unconditional encouragement and love, and without this, I could not have finished this dissertation. Her love, support, and guidance has made me a better researcher and, most importantly, a better person.

This research was supported by a grant from the U.S. Army Research Office as a Multi-disciplinary University Research Initiative on Standoff Inverse Analysis and Manipulation of Electronic Systems under grant number W911NF-05-1-0337.

TABLE OF CONTENTS

Page

Page

LIST OF TABLES

LIST OF FIGURES

Figure Page

ABBREVIATIONS

RF	Radio Frequency
FOD	First Order Distortion
IMD	Intermodulation Distortion
dB	Decibels
PIMD	Passive Intermodulation Distortion
IMR	Intermodulation Distortion Ratio
UWB	Ultra Wideband
FCC	Federal Communication Commission
SVM	Support Vector Machine
BT	Binary Tree
PW	Parzen Window
K-NN	K-Nearest Neighbor
EMIS	Electromagnetic Induction Spectroscopy
CBCD	Content-Based Copy Detection
EP	Electrophotographic
PRNU	Photoresponse Nonuniformity
ISM	Industrial Scientific Medical
GHD	Gaussian Harmonic Distortion
CART	Classification and Regression Tree
SNR	Signal to Noise Ratio
MHz	Megahertz
ns	Nanoseconds

ABSTRACT

Martone, Anthony F. Ph.D., Purdue University, December, 2007. Forensic Characterization of RF Circuits. Major Professor: Edward J. Delp.

Given the wide use of Radio Frequency (RF) devices for applications ranging from data networks to wireless sensors, it is of interest to identify the types of RF devices that are located in an environment. For example, one could be on campus at a university and would want to prevent their RF device from interfering with other devices. There are currently two techniques that are used to identify RF devices in the environment, which are known as passive and active fingerprinting. These fingerprinting techniques require that the RF device comply to some transmission standard (IEEE 802.11) and can therefore only be used to identify a subset of RF devices.

We propose an approach that can theoretically be used to identify any RF device. The proposed approach is used to determine sources of nonlinearities and identify filters that are present in the RF device. In our approach, a probe signal is transmitted to the RF device. The RF device retransmits or reradiates a return signal in response to the probe signal. The properties of the return signal are measured and these properties can be shown to contain distinct information that is inherent to sources of the nonlinearities and the filters of the RF device. This information constitutes features that can be used to identify the RF device.

In an effort to identify sources of nonlinearities, we will analyze the output signal obtained from a RF circuit model when the input is either a two-tone probe signal or a windowed linear chirp probe signal. It will be shown that the power spectral density of the output signal contains distinct features caused by nonlinearities in the RF circuit. These features are used to identify the nonlinearity and consequently the

RF device. In addition, we will analyze the output signal from the bandpass filter in the RF circuit when the input is either a windowed linear chirp probe signal or a linear chirp probe signal.

In this dissertation, we will use simulations to verify our methods. For each simulation, several RF circuit models are considered, where each circuit model contains a unique nonlinearity and bandpass filter. The features are classified using statistical pattern recognition techniques. Some of our results indicate that our simulation approach needs further investigation to validate it against actual measurement data.

1. INTRODUCTION

Given the wide use of Radio Frequency (RF) devices for applications ranging from data networks to wireless sensors, it is of interest to identify the types of RF devices that are located in an environment. For example, one could be on campus at a university and would want to prevent their RF device from interfering with other devices. This becomes the problem of determining the properties of an RF device/circuit by sending it a carefully designed signal, known as the probe signal $p(t)$. It can be shown that this probe will encounter the RF circuit and will be reradiated by the circuit, whether it is powered or not [1]. By examining the reradiated signal, which will be referred to here as the return signal $r(t)$, one can determine the type of RF device that is in the environment. Forensic characterization, or characterization, of the RF device refers to determining the make, model, configuration, and other characteristics of the device based on observations of the return signal that the device produces. The characteristics of the return signal that identify the RF device are known as a device signature.

To forensically characterize an RF device, we consider the distortions that are generated in the circuitry of the device in response to the probe signal, where the distortion will be defined as a modification of the original probe signal characteristics [2]. The distortion considered in this research is generated by nonlinear components, such as mixers, transistors, diodes, and passive connectors. An overview of the nonlinear sources that are commonly found in RF devices is presented in Section 1.2. When stimulated by the probe signal, the nonlinearity generates distortions at a priori frequency locations in the return signal spectrum. The amplitude/power at these frequency locations are distinct to the nonlinearity, and the device, and can therefore be used to characterize the RF device. For example, consider a two-tone probe signal, which is defined as

$$p(t) = A_1 \cos(2\pi f_1 t + \alpha_1) + A_2 \cos(2\pi f_2 t + \alpha_2) \tag{1.1}$$

where A_1 and A_2 are constant amplitudes, f_1 and f_2 are the probe frequencies of the two-tone signal, and α_1 and α_2 are phase angles. Let the probe frequency $f_2 = f_1 + \Delta$, where Δ is the frequency offset. When the two-tone signal is input into a nonlinearity, the nonlinearity generates distortion at the following discrete frequencies [3]

$$f_D(n_1, n_2) = n_1 f_1 + n_2 f_2 \tag{1.2}$$

where n_1 and n_2 are positive integers. The order of the distortion is defined as

$$O = |n_1| + |n_2| \tag{1.3}$$

For the case when $\{n_1 = 1, n_2 = 0\}$ or $\{n_1 = 0, n_2 = 1\}$, distortion occurs at the probe frequencies and is known as first order distortion (FOD). For the case when $n_1 = 0$ or $n_2 = 0$ in Equation 1.2 and $O > 1$ in Equation 1.3, the distortion is known as harmonic distortion [4] of the two-tone signal and is located at [5]

$$f_{har}(n_1) = n_1 f_1 \tag{1.4}$$

$n1 > 1$ and $n_2 = 0$,

$$f_{har}(n_2) = n_2 f_2 \tag{1.5}$$

when $n_2 > 1$ and $n_1 = 0$. The harmonic distortion that occurs at $O = n$ is known as the n^{th} order harmonic, where n is a positive integer and $n > 1$. For the case when $n_1 \neq 0$ and $n_2 \neq 0$ in Equation 1.2, the distortion is known as intermodulation distortion (IMD) [6] and is located at [7]

$$f_{imd}(n_1, n_2) = n_1 f_1 + n_2 f_2 \tag{1.6}$$

when $n_1 \neq 0$ and $n_2 \neq 0$. The IMD that occurs at $O = n$ will be referred to as the n^{th} order IMD, where n is a positive integer and $n > 1$.

Another way to forensically characterize an RF device is to analyze the response from an individual device component. As will be shown later, a linear chirp probe signal, or linear chirp signal, is used to characterize the frequency response [8], or filter response, of a bandpass filter in the RF device. The linear chirp signal is defined as

$$p(t) = A\cos(2\pi(f_0 + \frac{(f_1 - f_0)}{2t_1}t)t) \tag{1.7}$$

where A is the amplitude, f_0 is the initial frequency at time $t = 0$, f_1 is the final frequency at time t_1, and t_1 is the offset time between f_0 and f_1. The linear chirp signal probes a continuum of frequencies, or probe frequencies, from f_0 to f_1. As will be discussed in Section 1.1, the filter response is assumed to be known a priori. For example, consider the return signal $r(t)$ that is generated in response to a Chebyshev 4^{th} order bandpass filter. This type of filter is used in the experiments of Section 5.4.1 of Chapter 5. The power spectrum of $r(t)$ is shown in Figure 1.1 and defined as [9]

$$P_r(f) = R(f)R^*(f) \tag{1.8}$$

where $R^*(f)$ is the complex conjugate of $R(f)$, and $R(f)$ is the Fourier transform [9]

$$R(f) = F[r(t)] = \int_{-\infty}^{\infty} r(t)e^{-i2\pi ft}dt \tag{1.9}$$

As shown in Figure 1.1, distinct oscillation patterns are present in the filter passband. This pattern can be used to characterize the RF device. The amplitudes in Figure 1.1 are measured in units of decibels (dB), where for an arbitrary power value P_a

$$P_{dB} = 10log_{10}(\frac{P_a}{P_{ref}}) \tag{1.10}$$

where P_{ref} is the reference power level. It is also possible to express power in dBm, where $P_{ref} = 0.001$ watts, which is decibels referenced at 1 milliwatt of power.

1.1 Our Approach to RF Device Characterization

The approach presented in this dissertation is used to characterize/identify a finite number of RF devices. Each RF device type is assumed to be known a priori. We therefore have knowledge of each source of nonlinearity and knowledge of the filter properties in each RF device. This a priori information is used in the design of probe signals. The probe signal is designed such that, when input into the RF device, a

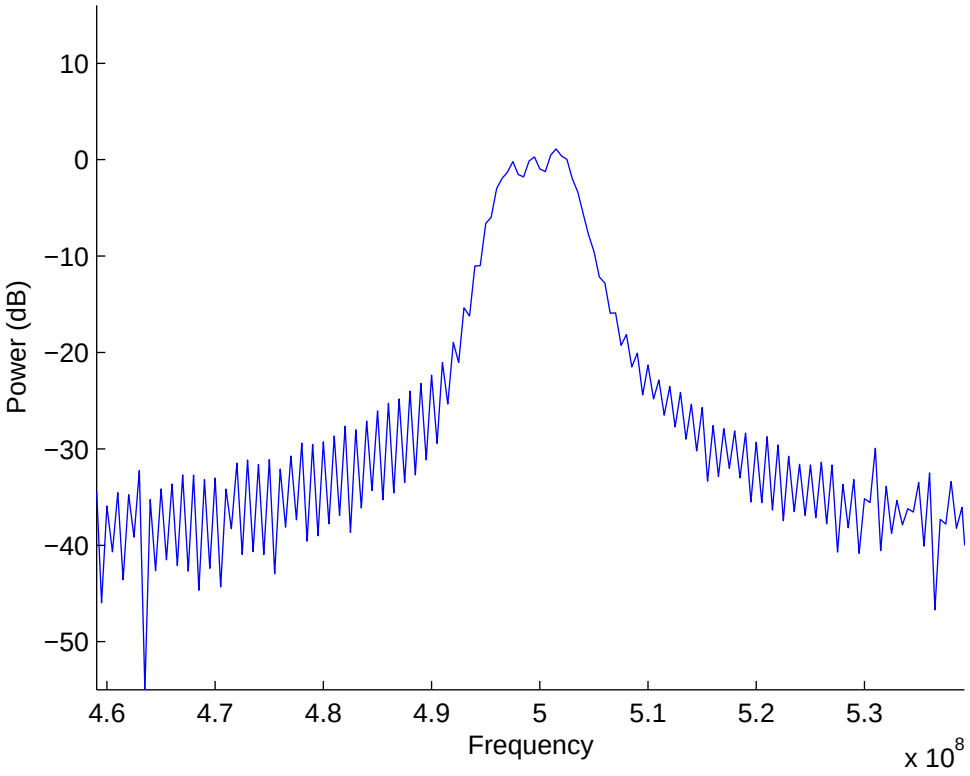

Fig. 1.1. Example Filter Response of a Chebyshev Bandpass Filter. A Distinct Oscillation Pattern is Shown in the Passband of the Filter Response.

unique signature is generated at specified frequency locations in the return signal. For example, if a two-tone probe signal is input into a nonlinearity, IMD/power is produced at known frequency locations in the return signal and are used as the RF forensic device signature. As another approach to forensic analysis developed here, consider the filter shown in Figure 1.1 (presented above). Since the filter is known a priori, the frequency range of the passband is known a priori. Therefore, the probe signal can be designed to estimate the response of the filter and use this as a forensic signature.

1.2 Sources of Nonlinearities

A variety of nonlinearities exists in an RF device. Common nonlinearities include mixers, transistors, diodes, and passive components such as connectors and cables. Mixers are commonly used circuit components in superheterodyne RF receivers and constitute the primary sources of nonlinear distortions [10] in RF devices. The mixer operation is designed to move or translate the input signal in the frequency domain [11]. This operation is known as down conversion. A mixer is essentially a multiplier where the received signal (or probe signal) is multiplied by a sinusoid known as the local oscillator signal. For example, consider $X_1 = \cos(2\pi f_1 t)$ as the probe signal and $X_2 = \cos(2\pi f_2 t)$ as the local oscillator signal. The mixer operation then becomes $Y = X_1 X_2 = \cos(2\pi f_1 t)\cos(2\pi f_2 t) = 0.5(\cos(2\pi(f_1 - f_2)t) + \cos(2\pi(f_1 + f_2)t))$. The result of the multiplication is a sum of two cosine functions with "mixed" frequencies at $f_1 - f_2$ and $f_1 + f_2$. By low pass filtering Y, one can obtain the downconverted signal with a frequency of $(f_1 - f_2)$. When X_1 and X_2 are multiplied in a circuit, mixing currents are created in the mixer at harmonic multiples [12], thereby leading to the nonlinear operation of the mixer. This nonlinear behavior has been used to characterize and model the mixer [13] [14].

In addition to mixers, diodes are also sources of nonlinearities. Diodes are fabricated as the union of two doped semiconductors [2]. The junction of these two

semiconductors is a distinct nonlinearity [2]. Transistors are also sources of nonlinearities. For example, bipolar transistors are a union of multiple semiconductors and have a distinct nonlinearity [2]. The nonlinear behavior of transistors is used to characterize the transistors performance. For example, the IMD can be used to characterize, model, and measure the performance of transistors [15] [16] [17].

When a two-tone signal is input into passive components, passive intermodulation distortion (PIMD) is generated [3] [18]. The actual mechanisms that cause nonlinear effects are not well understood [19]. However, the following have been identified to generate PIMD [20]: electron tunnelling at metallic contacts [21], planer transmission lines [22], coaxial connectors [23], micro discharge in metallic structure, dirt on metal surfaces, resistivity of carbon fiber, hysteresis effects of ferromagnetic materials, loose connections, cracks in metals, and oxidation at joints. PIMD generation is therefore highly dependent upon the quality and structure of the material. Any defect in the material can lead to the unwanted generation of PIMD. The PIMD has been used to measure the defects in the material and also used to characterize sources of the passive components [24].

1.3 RF Device Characterization Using Two-Tone Probe Signals

As discussed in Section 1.2, RF devices contain a wide variety of nonlinearities. The nonlinearities generate information in response to probe signals that can be used to characterize the RF device. Several probe signals have been used for RF device characterization purposes [25] [26]. One commonly used probe signal is the two-tone signal [27]. The two-tone signal was defined in Equation 1.1 and can be used to probe the nonlinearity. As discussed, the two-tone probe signal, $p(t)$, is input into an RF device and the response signal, $r(t)$, is returned. If nonlinearities are present in the RF device, then distortion is generated at the frequency locations specified by Equation 1.2. This distortion consists of first order distortion (FOD), harmonic

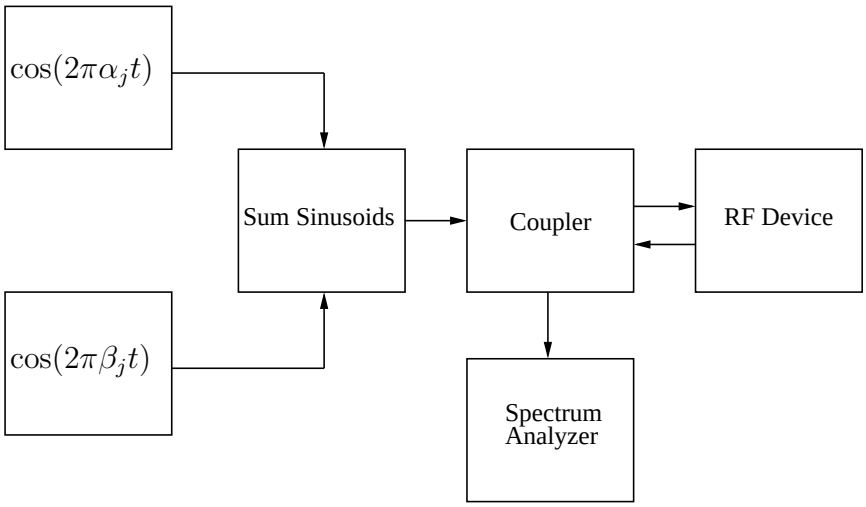

Fig. 1.2. RF Device Measurement System for the Walkie-Talkie.

distortion, and intermodulation distortion (IMD). The power spectrum of the return signal is used to analyze this distortion.

To study the distortion, consider the set of measured power spectrums of return signals $P_r = \{P_{r_1}(f), ...P_{r_{517}}(f)\}$ [28]. These power spectrums were generated by a "walkie-talkie"[1] in response to the following set of two-tone probe signals $\{p_1(t), ...p_{517}(t)\}$, where $p_j(t) = \cos(2\pi\alpha_j t) + \cos(2\pi\beta_j t)$, and $\alpha_j = 240.5x10^6 + \frac{j}{2}$, $\beta_j = \alpha_j + 0.1x10^6$, and $j \in \{1, 2, ...517\}$. α_j and β_j are the probe frequencies of $p_j(t)$.

The system used to measure P_r is shown in Figure 1.2 [2]. For iteration i, the waveform $p_i(t)$ is generated and sent to the RF device through the coupler. The return signal is sent to a spectrum analyzer through the coupler. The spectrum analyzer measures 216840 samples between 240MHz and 500MHz.

Example power spectrums for $j = 19$, $\alpha_{19} = 250$MHz, and $\beta_{19} = 250.1$MHz are shown in Figure 1.3. As shown in the Figure, the amplitudes of the FOD, located at $\alpha_{19} = 250$MHz and $\beta_{19} = 250.1$MHz, are -31.5 dBm and -30.33dBm.

[1]A walkie-talkie is a hand-held RF device (receiver and transmitter) that transmits and receives information to and from other walkie-talkies.

[2]The set of power spectrums were generated at North Carolina State University.

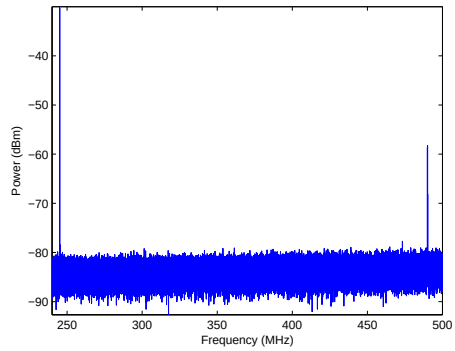

(a) First Order Distortions and Second Order Harmonics are Illustrated.

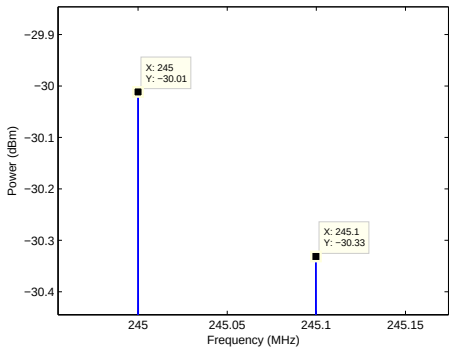

(b) First Order Distortions are Illustrated.

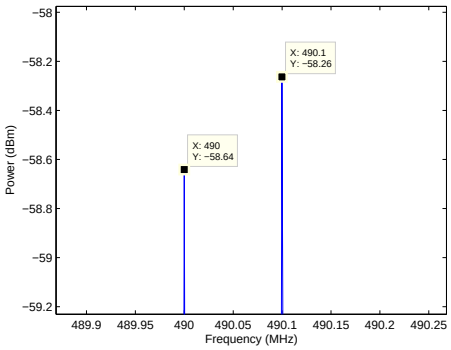

(c) Second Order Harmonics are Illustrated.

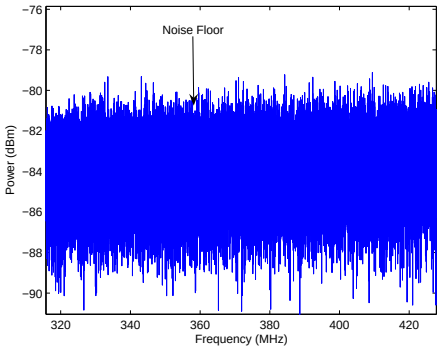

(d) Noise Floor is Illustrated.

Fig. 1.3. Power Spectrum of the Walkie-Talkie.

The amplitudes of the second order harmonics, located at $2\alpha_{19} = 500$MHz and $2\beta_{19} = 500.2$MHz, are -58.64dBm and -58.26dBm. The third order IMD's, located at $(2\alpha_{19} - \beta_{19}) = 249.1$MHz and $(2\beta_{19} - \alpha_{19}) = 250.2$MHz, are not visible in the Figure, since they are close to the noise floor, where the noise floor is the minimum signal level that can be detected [12]. The noise floor is used to describe the power level of the noise in the experiment and is shown in Figure 1.3(d). The third order IMD is determined as $P_{r_{19}}(2\alpha_{19} - \beta_{19}) = -81.6$dBm and $P_{r_{19}}(2\beta_{19} - \alpha_{19}) = -84.8$dBm.

To determine if the third order IMD is detectable, we shall examine Figure 1.4(a) for the following amplitudes $\{P_{r_1}(2\alpha_1 - \beta_1), ...P_{r_{517}}(2\alpha_{517} - \beta_{517})\}$. As shown in

the Figure, a pattern is indicated, which suggests that the third order IMD is detectable for this example. In addition, we will examine the fifth order IMD using $\{P_{r_1}(3\alpha_1 - 2\beta_1), ...P_{r_{517}}(3\alpha_{517} - 2\beta_{517})\}$, which is shown in Figure 1.4(b). As is shown in the Figure, no pattern is indicated, which suggests that the fifth order IMD is not detectable for this example.

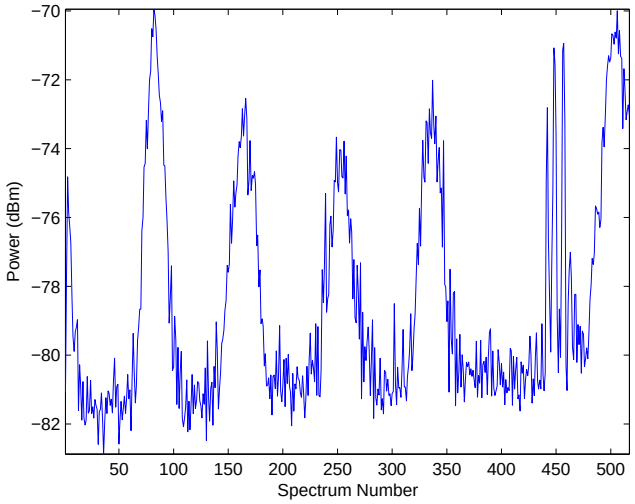

(a) Third Order. A Unique Pattern is Indicated.

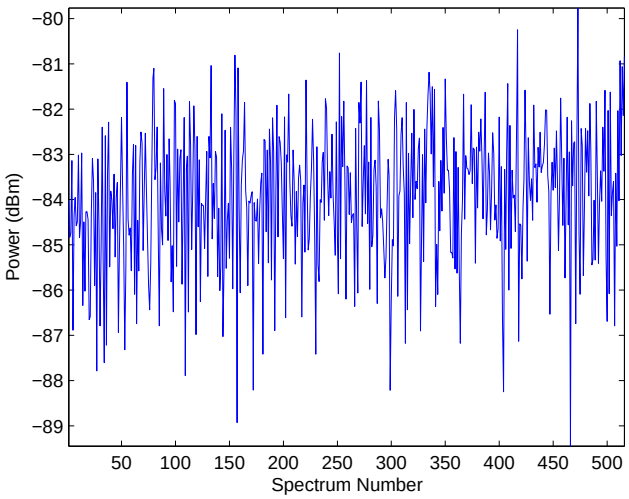

(b) Fifth Order. No Pattern is Indicated.

Fig. 1.4. Intermodulation Distortion Amplitude for the Power Spectrums in P_r.

This experiment shows that the FOD, the second order harmonic, and the third order IMD is present in the power spectrum presented in Figure 1.3(a). It was shown that the fifth order IMD, and consequently the higher order IMD's, were not detectable. This information will be used for the design of several circuit models that will be used for the simulations in Section 5.2 of Chapter 5. Although the second order harmonic is present in this experiment, typically it is discarded by the bandpass of the circuit [2].

A variety of methods can be used to measure the nonlinear performance of an RF device. Some performance measures include adjacent channel power ratio, co-channel power ratio, noise-to-power ratio [29], the third-order intercept point [6], and the intermodulation distortion ratio (IMR) [30]. The performance of the nonlinearities, and consequentially the performance rating of the RF device, are dependent on these testing schemes [2] [7]. In addition to the performance measures, models of the nonlinear source can be designed. By modeling the sources of the nonlinearity, accurate prediction and control of the IMD is achieved [31]. Modeling is also a way to lower the computational complexity of direct analysis [32].

We will measure nonlinear performance using the IMR. The IMR is used since it measures the contribution of all detectable IMD. Since the third order IMD was the only detectable IMD in the experiment of this Section, it will be used to measure the IMR. The IMR is defined as [2] [7]

$$IMR_L = \frac{P_r(2f_1 - f_2)}{P_r(f_1)} \tag{1.11}$$

or

$$IMR_U = \frac{P_r(2f_2 - f_1)}{P_r(f_2)} \tag{1.12}$$

where $P_r(f)$ is the power spectrum of the return signal $r(t)$, f_1 and f_2 are the probe frequencies of the two-tone signal.

1.4 Linear Chirp Signals

The linear chirp probe signal was described by Equation 1.7. The linear chirp signal is used in a variety of applications including pulse compression [33], radar [34], sonar [35], and spread spectrum communications [36]. The linear chirp signal is

$$p(t) = A\cos(2\pi(f_0 + \frac{(f_1 - f_0)}{2t_1}t)t) \tag{1.13}$$

where A is the amplitude, f_0 is the initial frequency at time $t = 0$, f_1 is the final frequency at time t_1, and t_1 is the offset time between f_0 and f_1. The instantaneous frequency of the signal is defined by [37]:

$$f_i = f_0 + kt \tag{1.14}$$

where

$$k = \frac{(f_1 - f_0)}{t_1} \tag{1.15}$$

One unique property of the linear chirp signal is that its instantaneous frequency increases over time. The increase in frequency is noticeable in the time domain for the linear chirp signal as illustrated in Figure 1.5, where $f_0 = 1$MHz, $f_1 = 100$MHz, $t_1 = 2$ microseconds (μs). An example of the instantaneous frequency is shown in Figure 1.6.

The increase in instantaneous frequency allows the linear chirp signal to have a relatively large bandwidth. For example, it can be used to transmit a low peak power signal over a long time duration while maintaining a large bandwidth. The bandwidth of the chirp signal $p(t)$ is defined as [38] [3]

$$B^2 = \frac{1}{E}\int_{-\infty}^{\infty}(2\pi f)^2|P(f)|^2 df \tag{1.16}$$

[3]It should be noted that there are many definitions of "bandwidth" of a signal. We are using this definition for chirp signals to illustrate the bandwidth properties of the signal.

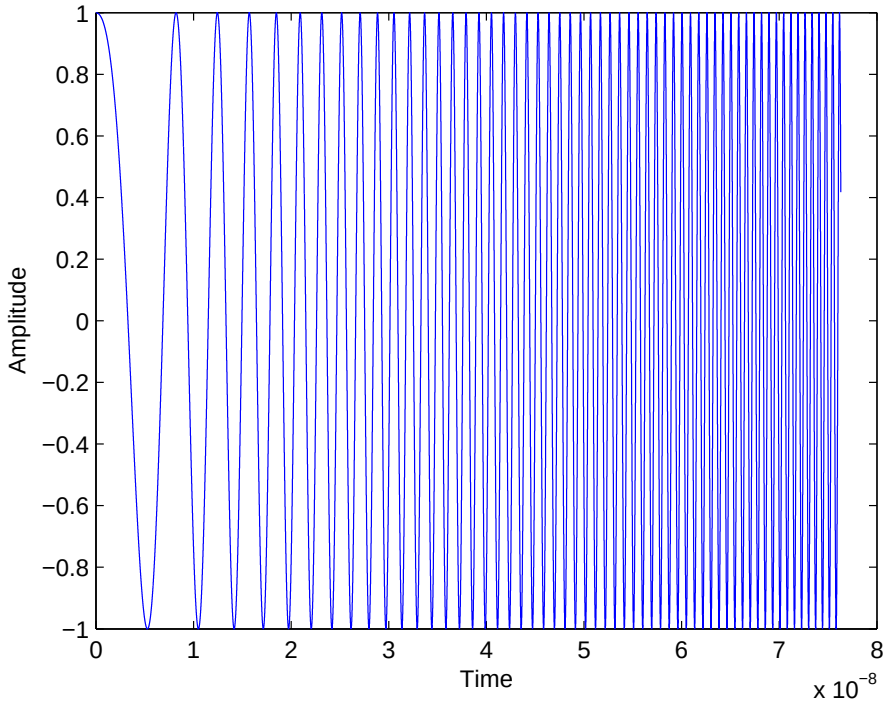

Fig. 1.5. Example of a Linear Chirp Probe Signal. As is Shown, the Frequency of Oscillations Increases With Respect to Time.

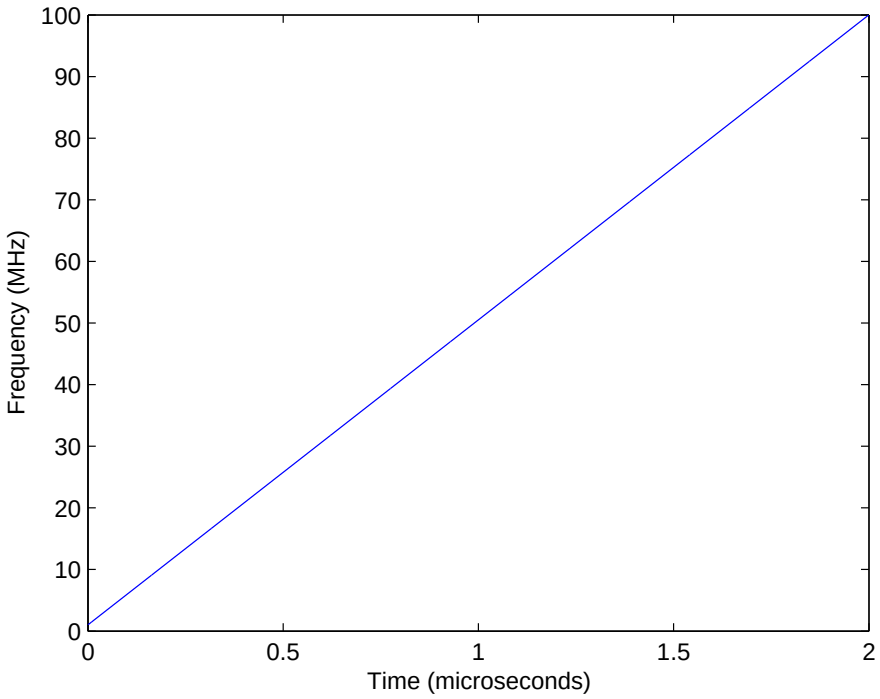

Fig. 1.6. Example of Instantaneous Frequency of the Linear Chirp Signal.

where $|P(f)|$ is the magnitude of the Fourier transform of $p(t)$, and E is the energy of $p(t)$ defined by [9]

$$E = \int_{-\infty}^{\infty} |p(t)|^2 dt \tag{1.17}$$

Pulse compression was first introduced in 1951 by Bernard Oliver at Bell Labs [39] [40]. Pulse compression is useful for applications that have peak signal limitations. To increase the power in a signal, one can either increase its amplitude or increase its time duration. However, increasing its time duration will decrease its bandwidth. The linear chirp signal can therefore replace short duration pulses that require high peak power and need to have the same bandwidth. Pulse compression is used by radar systems where high range resolution [34] [41] and maximum SNR is needed [39] [38] [42]. Pulse compression has also been considered for use in medical imaging, specifically ultrasound systems [43]. In the ultrasound system, a high power probe signal can be used for high resolution images. However, for safety reasons, a high power probe signal cannot be transmitted. Instead, a linear chirp signal can replace the high power signal using pulse compression.

In other applications, linear chirp signals have been used in spread spectrum communication as a way of transmitting information utilizing a wide band of frequencies [44]. "Spread spectrum is a means of transmission in which the signal occupies a bandwidth in excess of the minimum necessary to send the information; the band spread is accomplished by means of a code which is independent of the data, and a synchronized reception with the code at the receiver is used for despreading and subsequent data recovery [45]." Applications of spread spectrum communication include transmission of ultra wideband (UWB) signals [46], wireless local area networks [34], personal area networks [47], and noise jamming [41]. One way to "spread" the spectrum of a signal is by using the linear chirp signal [44].

In [48], a linear chirp signal is designed to have spectral content within a specified frequency band of 3.1GHz - 10.6GHz. The need for such a system is due to

Federal Communication Commission (FCC) regulations for the transmission of UWB signals. The shape of the linear chirp signal is designed using an electromagnetic pulse shaper [49]. The linear chirp signal was used to increase waveform energy and the RF power spectral density given peak voltage limitations in the electromagnetic pulse shaper. As mentioned above for pulse compression, the linear chirp signal is used since it can transmit a great deal of power by sending a low peak-power long-duration signal. The two waveforms studied in [48] are a linear chirp signal using a rectangular window and a linear chirp signal using a Gaussian window. It was shown that the Gaussian window function had a wider main lobe and more rapidly decaying side lobes as compared with the rectangular window.

For the characterization of RF devices, the linear chirp probe signal is attractive because it allows for the use of a probe signal that has a large spectrum that can be transmitted with a reasonable amount of power. A large probe bandwidth can be used to analyze multiple device components that operate at different frequencies simultaneously. For example, consider an RF device that contains two filters β_1 and β_2. Let the passband of β_1 be 200MHz-250MHz and the passband of β_2 be 500MHz-550MHz. A linear chirp signal can be designed to probe frequencies between $f_0 = 200$MHz and $f_1 = 550$MHz, which would identify the passband of both filters.

1.5 Proposed Forensic Characterization System

Our proposed RF device characterization system is illustrated in Figure 1.7 [50], where $p(t)$ is the probe signal and $r(t)$ is the return signal. $p(t)$ is transmitted into the environment and received by the RF device. As described in Section 1.1, the probe signal is designed to generate a specific RF signature at an a priori frequency location. Once received by the antenna of the RF device, the probe signal will encounter a nonlinearity and be reflected and reradiated from the device. An example is shown in Figure 1.8 for when the probe is filtered before the nonlinearity.

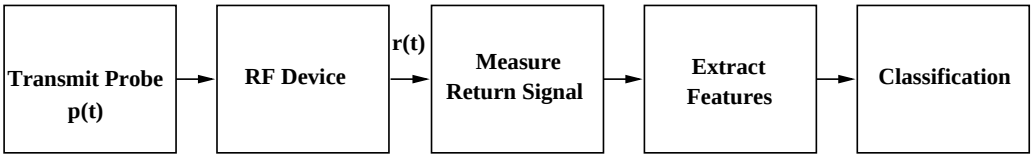

Fig. 1.7. Proposed RF Device Characterization System.

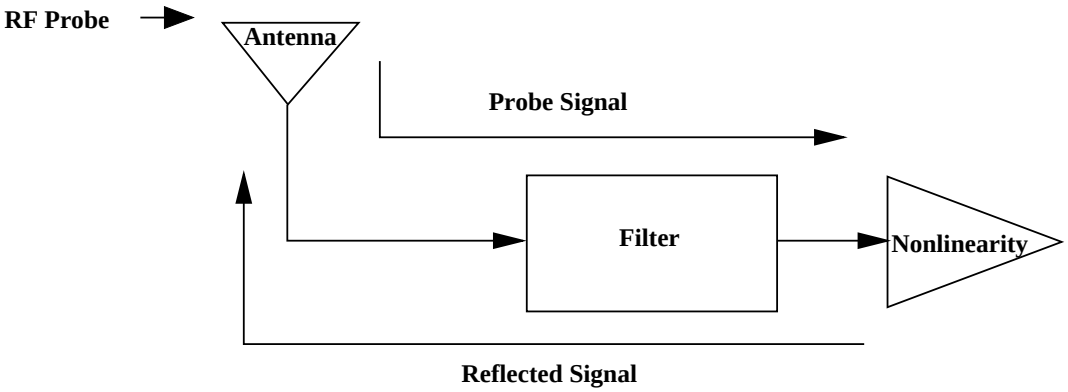

Fig. 1.8. Example of Probe Signal Input Into RF Device.

Once reradiated from the RF device, the proposed RF device characterization system obtains the return signal $r(t)$ and the power spectrum $P_r(f)$ of the return signal is estimated. Once the power spectrum of the signal is determined, the amplitude of frequency locations are sampled. These amplitudes are known as the features, where the features constitute the device signature and will be used to characterize the device. Each feature is modeled as a random variable $\mathbf{e}_i$. The set of features are formed into a random vector, known as a feature vector, and is defined as

$$\boldsymbol{\eta} = [\mathbf{e}_1 \ ... \ \mathbf{e}_G] \tag{1.18}$$

The feature vector is processed using statistical pattern recognition techniques [51]. Statistical pattern recognition is the process of mapping the feature vector into a category, or label, where the category corresponds to the RF device that generated the features. Six pattern recognition systems, or classifiers, are studied in this dissertation. These classifiers include a support vector machine (SVM), a binary tree (BT) classifier, two Bayesian classifiers, a Parzen window (PW) classifier, and a K-nearest neighbor (K-NN) classifier.

1.6 Other Applications of Forensic Fingerprinting

Forensic fingerprinting is the process of characterizing an object or electronic device based on unique characteristics. The fingerprint is the unique information used to characterize the object or device. This section provides an overview of forensic fingerprinting methods. Several fingerprinting applications are discussed which include fingerprinting humans, objects, multimedia content, printers, scanners, cameras, and RF devices.

In the most basic example, fingerprints are used in criminal investigations to identify people. A human fingerprint leaves a residue from the surface ridges of the finger [52]. The pattern of a fingerprint for any individual is unique, meaning that no two fingerprints are the same. The features of the human fingerprint are unique and

correspond to the spacial location of the surface ridges, which can be analyzed in the frequency domain. Human fingerprinting is an early form of forensic analysis and is the basis for many forensic applications.

Fingerprints are also used to characterize metallic objects buried in the ground. One application of this fingerprinting technique is landmine detection [53]. Similar to RF devices, the metallic object returns information (a signature) in response to a probe signal. The information is used to characterize the object. The metallic object has a distinct permeability, which can be identified using Electromagnetic Induction Spectroscopy (EMIS) [54]. The object is first probed by a time-varying low frequency electromagnetic field. Currents are induced in the object, which generates a magnetic field that can be used to characterize the object. This characterization approach is very similar to the proposed RF device characterization system.

In more recent applications, video forensic fingerprinting systems, which identify copyrighted video material, are being developed for internet websites. Video sharing websites, such as *YouTube*, allows users to upload videos and other content, which can then be downloaded by others. A growing problem with such websites is that copyrighted material, such as movies, are uploaded without the consent of the content owners. A particular video fingerprinting technique is content-based copy detection (CBCD) [55]. In CBCD, a fingerprint is extracted from the video and matched with known candidates in a database [56]. The fingerprint contains features that are inherent to the video. Typically, few features are needed for the fingerprint, which allows for a low computational complexity when matching the fingerprint with a candidate in the database [57].

In general, a device can be authenticated by developing a fingerprint based on information generated by the device [50]. For example, it may be of interest to identify a printer that was used in illegal activity or identify a source camera to authenticate digital photographs. Several approaches have been developed to characterize printers [58–61] [62–64] [65–67]. Two types of printers that can be characterized are electrophotographic (EP) and inkjet printers. The fingerprinting techniques are based

on the electromechanical properties of the printer. "In EP printing, artifacts are created in the printed output due to electromechanical imperfections in the printer such as fluctuations in the angular velocity of the OPC drum, gear eccentricity, gear backlash, and polygon mirror wobble [50]." The inkjet printer generates similar effects. These "imperfections" can be used to characterize the printer.

A digital camera can be authenticated by the noise characteristics in the digital image [68]. The two types of noise that can be used are fixed pattern noise and "photoresponse nonuniformity (PRNU) which is caused by variations in pixel responsivity [50] [69]." The fixed pattern noise is created by dark currents, which are defined as stray currents that leak into the sensor substrate [68]. The noise in image X can identified by subtracting it from a noiseless version, Y, of itself. Y is estimated using a wavelet denoiseing filter, and the noise can be found $X - Y$. The method used to characterize a digital camera can be extended to scanners, where the scanned image contains noise unique to the sensors that generated the image [70] [71].

1.6.1 RF Circuit Forensics

There are currently two existing techniques that are used to detect RF devices in the environment. These methods require that the RF device comply to a standard, for example the IEEE 802.11 standard. The RF device is therefore designed to transmit information independently, or when prompted by a probe signal. The RF devices that comply to the IEEE 802.11 standard use methods, described by the standard, for processing incoming and outgoing signals for the RF device. The manufacture is allowed, under the guidelines of the standard, to specify certain settings of the device. Therefore certain bytes of information are set by the manufacturer that are used to develop a fingerprint.

One approach used for RF device characterization is known as passive fingerprinting. In the passive fingerprinting, the RF device is independently transmitting information into the environment. Mobile telephone companies used a technique similar

to passive fingerprinting, known as Radio Frequency Fingerprinting [72], to prevent mobile phone cloning. In more recent applications, passive fingerprinting techniques are used to detect RF devices that comply to the IEEE 802.11 standard. In addition to fingerprinting hardware, a fingerprint can also be developed for the device driver. The device driver specifies the amount of information that is transmitted into the environment. The information is transmitted in packets or frames. The number of transmitted frames is different for each device driver. A fingerprint for the device driver can be developed based on the rate at which these frames are transmitted [73].

Another approach used for RF device characterization is known as active fingerprinting. The fingerprinting system transmits and receives information to and from the RF device that complies to a transmission protocol. The probe signal must have the ability to initiate connections with the RF device [74], meaning that the RF device can recognize and process the probe signal. Once a connection is established, the RF device transmits and receives information to and from the fingerprinting system. A fingerprint is then developed based on this information [72].

It is important to note that the approach used for the passive and active fingerprinting techniques described in this Section is very different from the approach used by our proposed RF device characterization system outlined in Figure 1.7. The fingerprinting techniques described in this Section require that the RF device comply to some transmission standard (IEEE 802.11) and can therefore only be used to characterize a subset of RF devices. Our proposed RF device characterization system can theoretically be used to characterize any device and, in particular, FCC Part 15 devices. Part 15 is a FCC mandate used for unlicensed radiators [75]. The general conditions of operation for Part 15 devices state that "an intentional, unintentional, or incidental radiator is subject to the conditions that no harmful interference is caused and that interference must be accepted that may be caused by the operation of an authorized radio station, by another intentional or unintentional radiator, by industrial, scientific and medical (ISM) equipment, or by an incidental radiator [76]." The term harmful interference is any transmission that seriously degrades, obstructs,

or repeatedly interrupts a radio communications service [77]. Some examples of Part 15 devices include wireless local area networks, cordless phones, walkie-talkies, garage door openers, wireless fences, and surveillance systems.

1.7 Outline of Dissertation

One of the first steps for RF device characterization is probe signal design. Chapter 2 presents the design of three probe signals. Time and frequency domain analysis is presented for each design. These three probe signals are a two-tone probe signal, a windowed linear chirp probe signal, and a linear chirp probe signal. Chapter 3 describes three feature types, where each feature is designed with respect to one of the three probe signals. All features considered in this Chapter are amplitudes that are sampled at deterministic frequency locations of the power spectrum of the return signal. Chapter 4 presents a review of 6 classification systems. This review is used to provide an overview of each classifier. Three simulations are presented in Chapter 5. The first simulation is designed to classify FOD and IMD features using 6 circuit models in response to a two-tone signal. The second simulation is used to classify harmonic distortion features using 5 circuit models in response to a windowed linear chirp signal. The third simulation is used to classify features that are sampled from the passband of two filter models. In addition, an experiment is presented which classifies the output of two RF device filters. The experiments are designed to follow the procedure of the third simulation.

1.8 Contributions

The contributions of this dissertation are as follows:

- Mathematical analysis of the output of a nonlinear system when a windowed linear chirp signal is its input. The power spectral density is derived in closed form. This analysis is used in the simulations.

- Developed methods for forensically characterizing circuit models using intermodulation distortion generated by nonlinearities in response to a two-tone probe signal. Classification errors are examined when the return signal is close to the noise floor. These simulations are presented in Section 5.2 of Chapter 5.

- Developed methods for forensically characterizing circuit models using harmonic distortion generated by nonlinearities in response to a windowed linear chirp signal. Classification errors are examined when the return signal is close to the noise floor. These simulations are presented in Section 5.3 of Chapter 5.

- Developed methods for forensically characterizing circuit models using the filter response of two Chebyshev filters. The filter response is estimated by the linear chirp probe signal. Both experimental and simulation results are compared. These results indicate that the distinct oscillating patterns in the passband of the "real" RF circuits may be caused by other sources.

- Comparison of classification accuracy of the pattern recognition methods.

2. PROBE SIGNAL DESIGN

In this Chapter, three probe signals are considered. These are a two-tone probe signal, a windowed linear chirp probe signal, and a linear chirp probe signal. From these three probe signals we will study various methods to characterize the return signal after they are used as inputs to an RF circuit model. The two-tone probe signal is presented in Section 2.1. The two-tone signal is input into a third order nonlinearity modeled by a power series. The power spectrum is derived for the output of this nonlinearity and contains intermodulation distortion (IMD). The windowed linear chirp probe signal is presented in Section 2.2. This signal is also input into a third order nonlinearity and the power spectrum is derived for the output of the nonlinearity. It will be shown that this power spectrum contains harmonic distortions. The linear chirp probe is presented in Section 2.3 and is used to estimate the filter response of the RF circuit. In this Chapter, we will denote the probe signal as $x(t)$ and the return signal as $y(t)$ since we are not analyzing the entire RF system.

2.1 Two-Tone Probe Signals

The two-tone signal is

$$x(t) = A_1 \cos(2\pi f_1 t) + A_2 \cos(2\pi f_2 t) \tag{2.1}$$

The parameters of the signal are defined in Table 2.1. An example of $x(t)$ is shown in Figure 2.1(a), where $f_1 = 40$MHz, $f_2 = 40.1$MHz, and t ranges from 0 to 2x10^{-6} seconds. The Fourier transform of $x(t)$ is [9]

Table 2.1
Two-Tone Probe Signal Parameters.

Parameter	Description	Definition
A_1	Amplitude of first sinusoid	$A_1 \in \Re$
A_2	Amplitude of second sinusoid	$A_2 \in \Re$
t	Time (seconds)	$t \in \Re$
f_1	Probe frequency of first sinusoid (Hz)	$f_1 \in \Re$
f_2	Probe frequency of second sinusoid (Hz)	$f_2 = f_1 + \Delta$
Δ	Offset between probe frequencies (Hz)	$\Delta \in \Re$

$$X(f) = \int_{-\infty}^{\infty} x(t)e^{-i2\pi ft}dt = \frac{A_1\delta(f-f_1) + A_1\delta(f+f_1)}{2} + \frac{A_2\delta(f-f_2) + A_2\delta(f+f_2)}{2} \tag{2.2}$$

This derivation is shown in Appendix B. The power spectrum of $x(t)$ is defined as $P_x(f) = X(f)X^*(f)$, where $X^*(f)$ is the complex conjugate of $X(f)$. The energy of a two-tone signal is concentrated at the locations of the discrete probe frequencies f_1 and f_2 as shown in Figure 2.1(b).

When input into a nonlinearity, the two-tone signal generates IMD. The nonlinearity is modeled as a power series of order M as shown in [78] [79]

$$y(t) = \sum_{j=1}^{M} a_j[x(t)]^j \tag{2.3}$$

The IMD is located at discrete positions in the power spectrum of $y(t)$. The IMD locations are defined as

$$f_{imd}(n_1, n_2) = n_1 f_1 + n_2 f_2 \tag{2.4}$$

where $n_1 \neq 0$ and $n_2 \neq 0$. The order of the IMD is defined by [3]

$$O = |n_1| + |n_2| \tag{2.5}$$

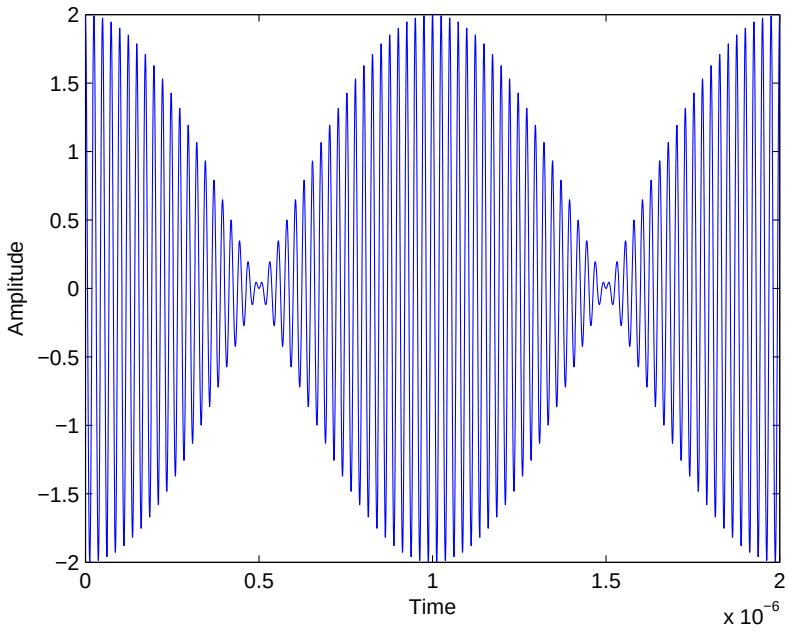

(a) $x(t)$

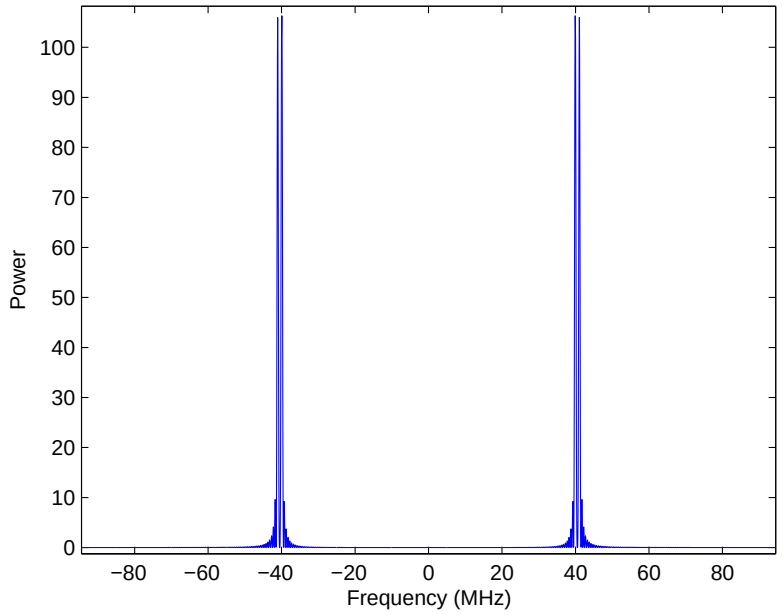

(b) $P_x(f)$

Fig. 2.1. Example of a Two-Tone Signal in the Time Domain and Frequency Domain. $f_1 = 40$MHz, $f_2 = 40.1$MHz, and t ranges from 0 to 2x10^{-6} seconds.

2.1.1 Third Order Analysis

In this Section, the two-tone signal defined in Equation 2.1 is input into a power series of order $M = 3$ [78] [79]

$$y(t) = \sum_{j=1}^{3} a_j [A_1 \cos(2\pi f_1 t) + A_2 \cos(2\pi f_2 t)]^j \tag{2.6}$$

Expanding Equation 2.6

$$\begin{aligned} y(t) &= b_0^1 + b_1^1 \cos(2\pi f_1 t) + b_1^2 \cos(2\pi f_2 t) + b_2^1 \cos(2\pi [2f_1] t) + b_2^2 \cos(2\pi [2f_2] t) \\ &+ b_3^1 \cos(2\pi [3f_1] t) + b_3^2 \cos(2\pi [3f_2] t) + b_4^1 \cos(2\pi [f_1 + f_2] t) + b_4^2 \cos(2\pi [f_2 - f_1] t) \\ &+ b_5^1 \cos(2\pi [2f_1 + f_2] t) + b_5^2 \cos(2\pi [2f_1 - f_2] t) + b_5^3 \cos(2\pi [2f_2 + f_1] t) \\ &+ b_5^4 \cos(2\pi [2f_2 - f_1] t) \end{aligned} \tag{2.7}$$

The constant coefficients of Equation 2.7 are defined in Table 2.2. The complete derivation of $y(t)$ is shown in Appendix A. An example of $y(t)$ is shown in Figure 2.2.

The Fourier transform of Equation 2.7 is

$$\begin{aligned} Y(f) &= b_0^1 \delta(f) + \tfrac{b_1^1}{2}\delta(f - f_1) + \tfrac{b_1^1}{2}\delta(f + f_1) + \tfrac{b_1^2}{2}\delta(f - f_2) + \tfrac{b_1^2}{2}\delta(f + f_2) \\ &+ \tfrac{b_2^1}{2}\delta(f - [2f_1]) + \tfrac{b_2^1}{2}\delta(f + [2f_1]) + \tfrac{b_2^2}{2}\delta(f - [2f_2]) + \tfrac{b_2^2}{2}\delta(f + [2f_2]) \\ &+ \tfrac{b_3^1}{2}\delta(f - [3f_1]) + \tfrac{b_3^1}{2}\delta(f + [3f_1]) + \tfrac{b_3^2}{2}\delta(f - [3f_2]) + \tfrac{b_3^2}{2}\delta(f + [3f_2]) \\ &+ \tfrac{b_4^1}{2}\delta(f - [f_1 + f_2]) + \tfrac{b_4^1}{2}\delta(f + [f_1 + f_2]) + \tfrac{b_4^2}{2}\delta(f - [f_2 - f_1]) \\ &+ \tfrac{b_4^2}{2}\delta(f + [f_2 - f_1]) + \tfrac{b_5^1}{2}\delta(f - [2f_1 + f_2]) + \tfrac{b_5^1}{2}\delta(f + [2f_1 + f_2]) \\ &+ \tfrac{b_5^2}{2}\delta(f - [2f_1 - f_2]) + \tfrac{b_5^2}{2}\delta(f + [2f_1 - f_2])] + \tfrac{b_5^3}{2}\delta(f - [2f_2 + f_1]) \\ &+ \tfrac{b_5^3}{2}\delta(f + [2f_2 + f_1]) + \tfrac{b_5^4}{2}\delta(f - [2f_2 - f_1]) + \tfrac{b_5^4}{2}\delta(f + [2f_2 - f_1]) \end{aligned} \tag{2.8}$$

where $\delta(f)$ is a Dirac Delta Function. The derivation of this Equation is shown in Appendix B. The power spectrum of $Y(f)$ is $P_y(f) = Y(f)Y^*(f)$. The power spectrum $P_y(f)$ of $Y(f)$ is

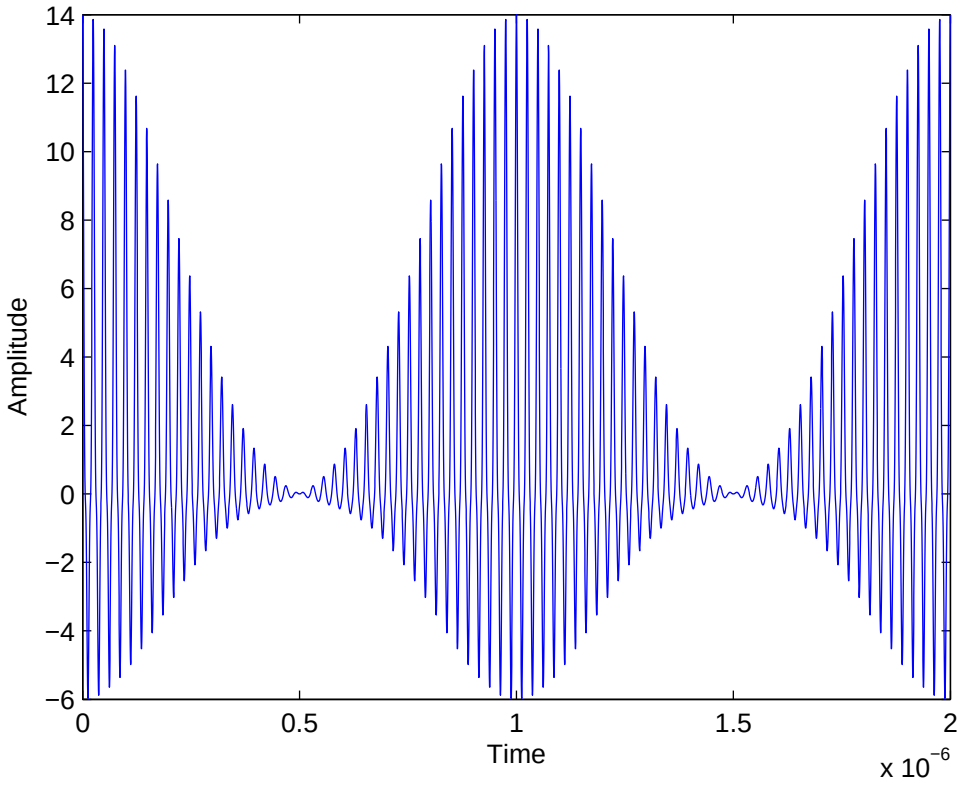

Fig. 2.2. Example Output from a Nonlinearity of Order M=3 When the Input is a Two-Tone Signal. $a_1 = a_2 = a_3 = 1$, $f_1 = 40$MHz, $f_2 = 40.1$MHz, and t ranges from 0 to 2x10^{-6} seconds.

Table 2.2
Parameter Definitions for Constants in $y(t)$.

Parameter	Description	Coefficients
b_0^1	Constant	$\frac{a_2(A_1)^2}{2} + \frac{a_2(A_2)^2}{2}$
b_1^1	1^{st} order harmonic	$a_1A_1 + \frac{a_3(A_1)^3}{2} + \frac{a_3(A_1)^3}{4} + \frac{3a_3A_1(A_2)^2}{2}$
b_1^2	1^{st} order harmonic	$a_1A_2 + \frac{3a_3(A_1)^2A_2}{2} + \frac{a_3(A_2)^3}{2} + \frac{a_3(A_2)^3}{4}$
b_2^1	2^{nd} order harmonic	$\frac{a_2(A_1)^2}{2}$
b_2^2	2^{nd} order harmonic	$\frac{a_2(A_2)^2}{2}$
b_3^1	3^{rd} order harmonic	$\frac{a_3(A_1)^3}{4}$
b_3^2	3^{rd} order harmonic	$\frac{a_3(A_2)^3}{4}$
b_4^1	2^{nd} order intermodulation	$a_2A_1A_2$
b_4^2	2^{nd} order intermodulation	$a_2A_1A_2$
b_5^1	3^{rd} order intermodulation	$\frac{3a_3(A_1)^2A_2}{4}$
b_5^2	3^{rd} order intermodulation	$\frac{3a_3(A_1)^2A_2}{4}$
b_5^3	3^{rd} order intermodulation	$\frac{3a_3A_1(A_2)^2}{4}$
b_5^4	3^{rd} order intermodulation	$\frac{3a_3A_1(A_2)^2}{4}$

$$
\begin{aligned}
&P_y(f) = [b_0^1]^2\delta(f)^2 + [\tfrac{b_1^1}{2}]^2\delta(f-f_1)^2 \\
&+[\tfrac{b_1^1}{2}]^2\delta(f+f_1)^2 + [\tfrac{b_1^2}{2}]^2\delta(f-f_2)^2 + [\tfrac{b_1^2}{2}]^2\delta(f+f_2)^2 \\
&+[\tfrac{b_2^1}{2}]^2\delta(f-[2f_1])^2 + [\tfrac{b_2^1}{2}]^2\delta(f+[2f_1])^2 + [\tfrac{b_2^2}{2}]^2\delta(f-[2f_2])^2 + [\tfrac{b_2^2}{2}]^2\delta(f+[2f_2])^2 \\
&+[\tfrac{b_3^1}{2}]^2\delta(f-[3f_1])^2 + [\tfrac{b_3^1}{2}]^2\delta(f+[3f_1])^2 + [\tfrac{b_3^2}{2}]^2\delta(f-[3f_2])^2 + [\tfrac{b_3^2}{2}]^2\delta(f+[3f_2])^2 \\
&+[\tfrac{b_4^1}{2}]^2\delta(f-[f_1+f_2])^2 + [\tfrac{b_4^1}{2}]^2\delta(f+[f_1+f_2])^2 + [\tfrac{b_4^2}{2}]^2\delta(f-[f_2-f_1])^2 \\
&+[\tfrac{b_4^2}{2}]^2\delta(f+[f_2-f_1])^2 + [\tfrac{b_5^1}{2}]^2\delta(f-[2f_1+f_2])^2 + [\tfrac{b_5^1}{2}]^2\delta(f+[2f_1+f_2])^2 \\
&+[\tfrac{b_5^2}{2}]^2\delta(f-[2f_1-f_2])^2 + [\tfrac{b_5^2}{2}]^2\delta(f+[2f_1-f_2])^2 + [\tfrac{b_5^3}{2}]^2\delta(f-[2f_2+f_1])^2 \\
&+[\tfrac{b_5^3}{2}]^2\delta(f+[2f_2+f_1])^2 + [\tfrac{b_5^4}{2}]^2\delta(f-[2f_2-f_1])^2 + [\tfrac{b_5^4}{2}]^2\delta(f+[2f_2-f_1])^2
\end{aligned}
\tag{2.9}
$$

The derivation of this Equation is shown in Appendix B. Note that all the energy occurs at discrete frequency locations.

2.2 Windowed Linear Chirp Signal

We are interested in studying other types of probe signals to see whether they can perform better when used to forensically characterize a RF circuit. In this Section, we describe linear chirp signals. As discussed in Section 1.4 of Chapter 1, chirp signals are attractive because they allow the probe to have a large bandwidth and higher transmission power. The frequency content of the probe may then generate more harmonic components that can be used to characterize the circuit. Following the approach of the two-tone signal, a windowed linear chirp signal is input into a nonlinearity and the response is analyzed in the frequency domain. A linear chirp signal is defined as

$$l(t) = C_1 e^{i\phi(t)} \tag{2.10}$$

$$\phi(t) = 2\pi f_0 t + \pi k t^2 \tag{2.11}$$

Where $\phi(t)$ is known as the instantaneous phase of the chirp signal. The parameters in Equations 2.10 and 2.11 are defined in Table 2.3. The frequency at any given time t is known as the instantaneous frequency and is defined as [80]

$$f_i = \frac{\dot{\phi}(t)}{2\pi} = f_0 + kt \tag{2.12}$$

A Gaussian window function is multiplied by the linear chirp signal in the time domain [81] [82]. As mentioned in Section 1.4 of Chapter 1, the Gaussian window function is used since it generates a wide main lobe and produces rapidly decaying side lobes in the frequency domain [48]. The Gaussian window function will be described in the form of a Gaussian envelop [37]

Table 2.3
Linear Chirp Probe Signal Parameters.

Parameter	Description	Definition
C_1	Amplitude of signal	$C_1 \in \Re$
i	Imaginary number	$\sqrt{-1}$
t	Time	$t \in \Re$
t_1	Time at frequency f_1	$t_1 \in \Re, t_1 > 0$
f_0	Frequency at $t = 0$	$f_0 \in \Re$
f_1	Frequency at time t_1	$f_1 \in \Re, f_1 > f_0$
k	Chirp rate	$\frac{(f_1 - f_0)}{t_1}$

$$w(t) = e^{\frac{-(t-\mu)^2}{2\sigma^2}} \tag{2.13}$$

where

$$\mu = \int_{-\infty}^{\infty} t w(t) dt \tag{2.14}$$

and

$$\sigma^2 = \int_{-\infty}^{\infty} (t-\mu)^2 w(t) dt > 0 \tag{2.15}$$

The windowed linear chirp signal, which is known as a Gaussian chirp signal, is then formed, $x(t) = w(t)l(t)$. $x(t)$ is

$$x(t) = C_1 e^{i\phi(t)} e^{\frac{-(t-\mu)^2}{2\sigma^2}} \tag{2.16}$$

An example of a Gaussian chirp signal is shown in Figure 2.3. The parameters of this signal are shown in Table 2.4. These parameters where chosen for illustration purposes.

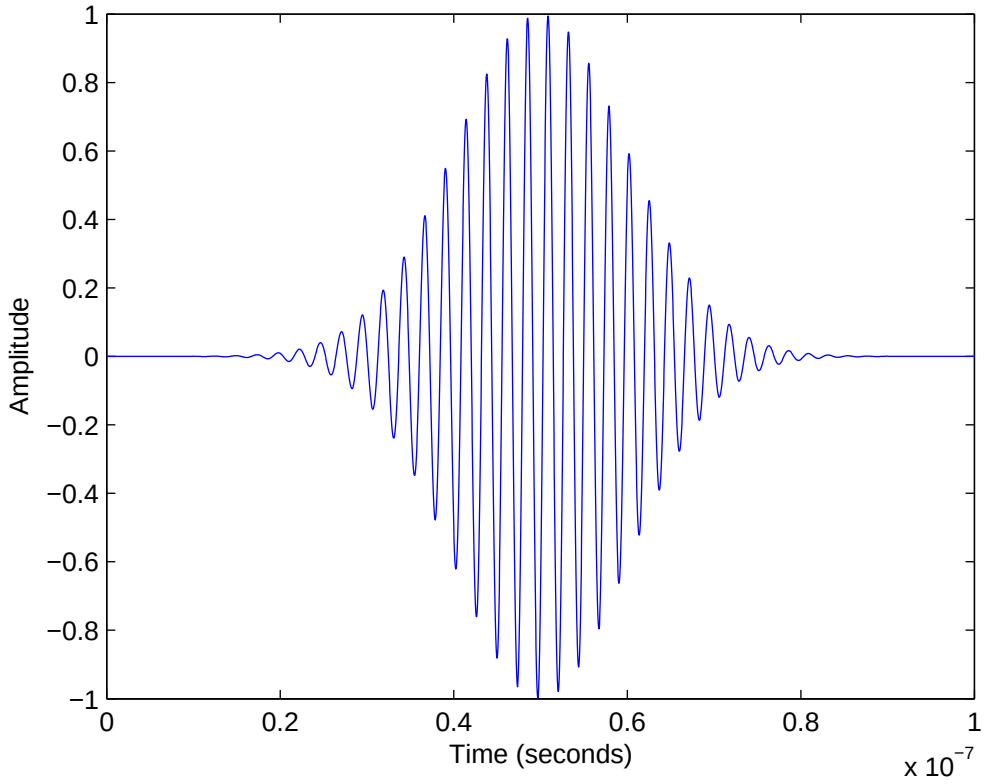

Fig. 2.3. Example of a Gaussian Chirp Signal in the Time Domain, Where Parameters are Defined in Table 2.4.

Table 2.4
Windowed Chirp Signal Parameters.

Parameter	Description	Value
C_1	Amplitude of signal	1
i	Imaginary number	$\sqrt{-1}$
f_0	Initial frequency at $t = 0$	400MHz
f_1	Final frequency at time t_1	450MHz
t_1	Final time	$0.1\text{x}10^{-6}$
k	Chirp rate	$5\text{x}10^{14}$
μ	Mean	$5\text{x}10^{-8}$
σ	Standard deviation	$1\text{x}10^{-8}$

Similar to the approach used for the two-tone probe, $x(t)$ is input into a non-linearity modeled as the power series described in Equation 2.6. The output then becomes

$$y(t) = \sum_{j=1}^{M} a_j (C_1)^j e^{ij\phi(t)} e^{\frac{-j(t-\mu)^2}{2\sigma^2}} \tag{2.17}$$

$y(t)$ is shown in Figure 2.4. The parameters of this Figure are defined in Table 2.4, and $a_1 = a_2 = a_3 = 1$.

The signal $y(t)$ contains distortion at specific frequencies. Substituting $y(t)$ into the Fourier transform produces

$$Y(f) = \int_{-\infty}^{\infty} [\sum_{j=1}^{M} a_j (C_1)^j e^{ij\phi(t)} e^{\frac{-j(t-\mu)^2}{2\sigma^2}}] e^{-i2\pi ft} dt \tag{2.18}$$

where the closed form solution is

$$Y(f) = \sum_{j=1}^{M} [\sqrt{\pi} a_j (C_1)^j e^{\frac{-j\mu^2}{2\sigma^2}}] \frac{e^{\frac{-(2\pi f - j2\pi f_0 + \frac{ij\mu}{\sigma^2})^2}{2j(\frac{1}{\sigma^2} - i2\pi k)}}}{\sqrt{\frac{j}{2\sigma^2} - ij\pi k}} \tag{2.19}$$

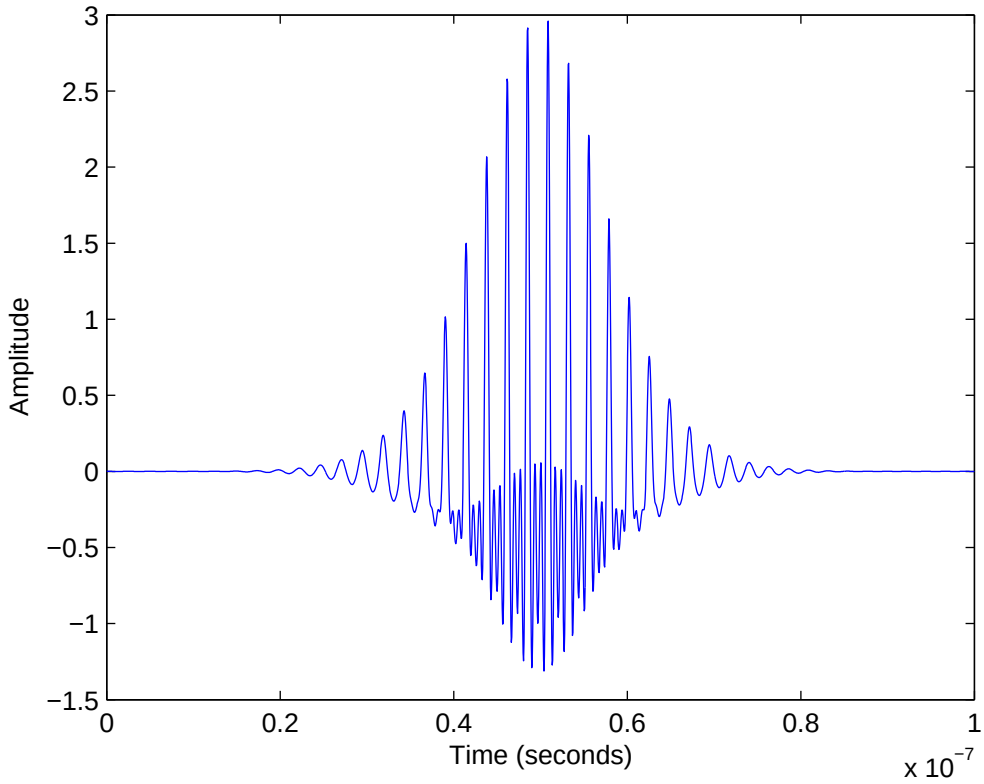

Fig. 2.4. Output from the Nonlinearity of Order $M = 3$, Where the Input is the Gaussian Chirp Signal.

The derivation of Equation 2.19 is shown in Appendix C. $Y(f)$ is formed into its magnitude and phase components as follows

$$Y(f) = C_2 \sum_{j=1}^{M} [C_3(j) e^{iC_4(j)}] \xi(j,f) e^{i\psi(j,f)} \tag{2.20}$$

where

$$\xi(j,f) = e^{\frac{-2\pi^2\sigma^2}{j\gamma^2}(f - j(f_0 + \mu k))^2} \tag{2.21}$$

$$\psi(j,f) = \frac{-4\pi^3\sigma^4 k}{j\gamma^2}(f + \frac{j\mu}{4\pi^2\sigma^4 k} - jf_0)^2 \tag{2.22}$$

$$C_3(j) = \frac{a_j (C_1)^j}{\sqrt{j}} e^{\frac{-j\mu^2}{2\sigma^2} + \frac{j\mu^2}{2\sigma^2\gamma^2} - \frac{4\pi^2\sigma^2 k\mu f_0 j}{\gamma^2} + \frac{2\pi^2\sigma^2 j(f_0 + k\mu)^2}{\gamma^2} - \frac{2\pi^2\sigma^2 j f_0^2}{\gamma^2}} \tag{2.23}$$

$$C_4(j) = \frac{jk\pi\mu^2}{\gamma^2} - \frac{jk4\pi^3\sigma^4 f_0^2}{\gamma^2} + \frac{2\pi j f_0 \mu}{\gamma^2} + \frac{4\pi^3\sigma^4 k}{j\gamma^2}(\frac{\mu j}{4\pi^2\sigma^4 k} - jf_0)^2 \tag{2.24}$$

$$C_2 = \frac{\sqrt{2\pi\sigma^2} e^{i\frac{\arctan(2\pi\sigma^2 k)}{2}}}{\sqrt{\gamma}} \tag{2.25}$$

$$\gamma = \sqrt{1 + 4\pi^2\sigma^4 k^2} \tag{2.26}$$

The derivation of Equation 2.20 is shown in Appendix C. Note that when j=1 in Equation 2.20

$$X(f) = C_2 [C_3(1) e^{iC_4(1)}] \xi(1,f) e^{i\psi(1,f)} \tag{2.27}$$

which is the Fourier transform of $x(t)$. The power spectrum of $Y(f)$ is

$$\begin{aligned} P_y(f) = Y(f)Y(f)^* = C_2 C_2^* \{ &\sum_{j=1}^{M} [C_3(j)\xi(j,f)]^2 + \\ &\sum_{j=1}^{M-1} \sum_{l=j+1}^{M} 2C_3(j)C_3(l)\xi(j,f)\xi(l,f)\cos(C_4(j) - C_4(l) + \psi(j,f) - \psi(l,f)) \} \end{aligned} \tag{2.28}$$

The derivation of $P_y(f)$ is shown in Appendix D. Note that, when $j = 1$ and $l = 0$ in Equation 2.28

$$P_x(f) = [C_3(1)\xi(1, f)]^2 \tag{2.29}$$

which is the power spectrum of $x(t)$. A graph of $P_x(f)$ and $P_y(f)$ are illustrated in Figure 2.5, where the Gaussian chirp signal parameters are shown in Table 2.4, where $a_1 = a_2 = a_3 = 1$. As is shown, harmonic distortion is located at

$$f_{har}(n_1) = n_1[f_0 + \mu k] \tag{2.30}$$

where $n_1 \in \{1, ...M\}$, $[f_0 + \mu k]$ is defined as the mean of $\xi(1, f)$, and, for these Figures, $[f_0 + \mu k] = 425MHz$. The harmonic distortion defined by Equation 2.30 is known as Gaussian harmonic distortion (GHD). GHD is present in the power spectrum at each harmonic.

Equation 2.28 is a combination of square-terms and cross-terms. The square-terms are defined as

$$\text{square-terms} = \{\sum_{j=1}^{M}[C_3(j)\xi(j, f)]^2\} \tag{2.31}$$

The cross-terms are defined as

$$\text{cross-terms} = \{\sum_{j=1}^{M-1}\sum_{l=j+1}^{M} 2C_3(j)C_3(l)\xi(j, f)\xi(l, f)\cos(C_4(j)-C_4(l)+\psi(j, f)-\psi(l, f))\} \tag{2.32}$$

Closer examination of the square-terms $\sum_{j=1}^{M}[C_3(j)\xi(j, f)]^2 = \sum_{j=1}^{M}[C_3(j)\, e^{\frac{-4\pi^2\sigma^2}{j\gamma^2}(f-j[f_0+\mu k])}$ illustrates that the square-terms are a sum of GHD. The mean of $\xi(j, f)^2$ is

$$\mu_\xi(j) = j[f_0 + \mu k] \tag{2.33}$$

and the variance of $\xi(j, f)^2$ is

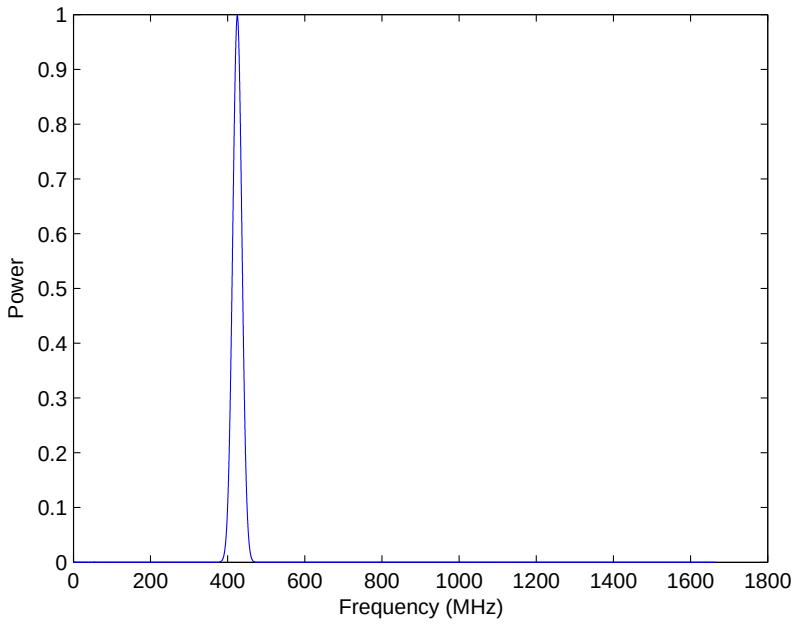

(a) $P_x(f)$

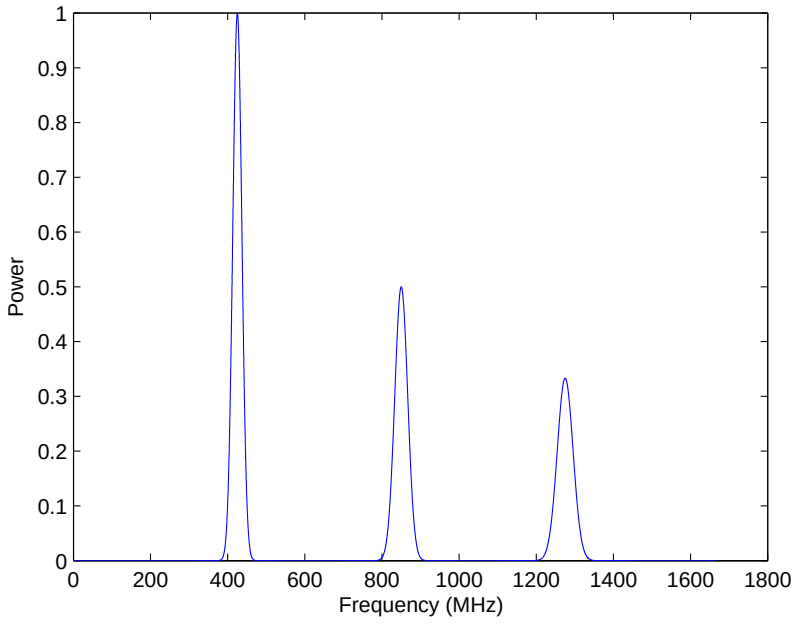

(b) $P_y(f)$

Fig. 2.5. Comparison of the Power Spectrum of the Gaussian Chirp Probe Signal $P_x(t)$ with the Output of the Nonlinearity $P_y(f)$. Parameters are Defined in Table 2.4.

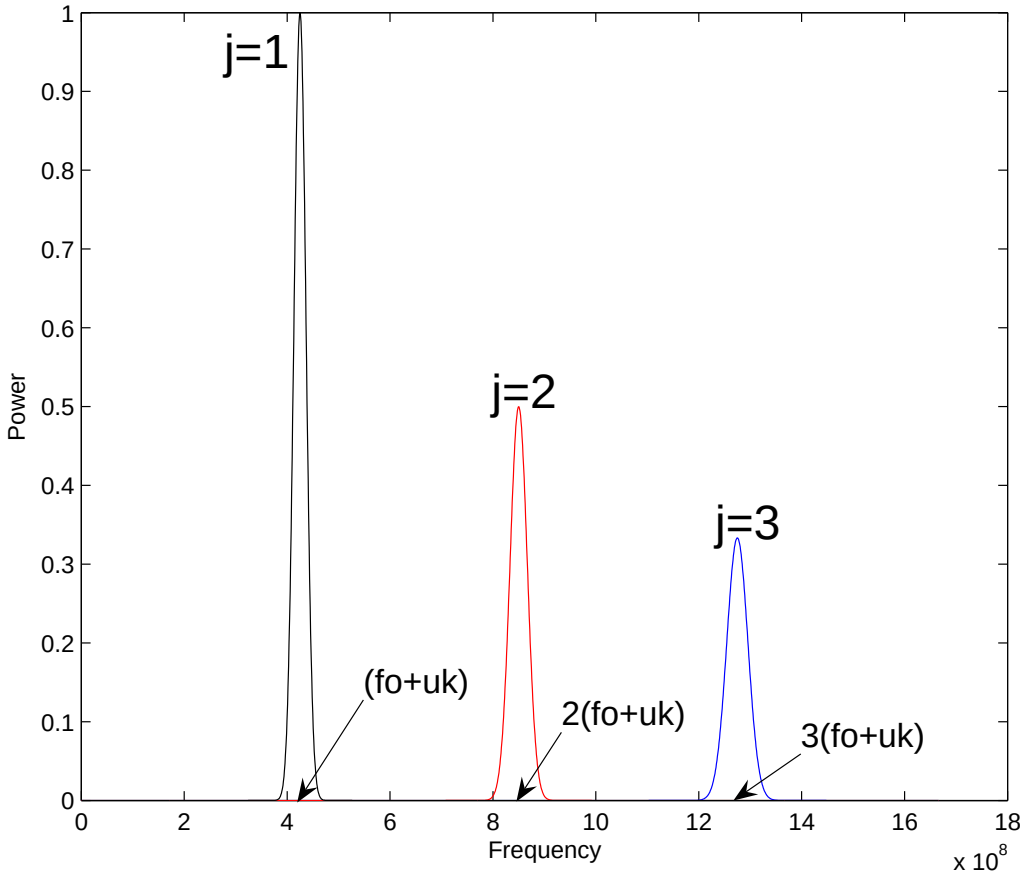

Fig. 2.6. Example Output of a Third Ordered Nonlinear System. Each GHD is Generated by a Square-Term.

$$\sigma_{\xi}^{2}(j) = \frac{j\gamma^{2}}{8\pi^{2}\sigma^{2}} \tag{2.34}$$

The peak of each GHD is located using Equation 2.33. An example response of a third order system using a Gaussian chirp signal is illustrated in Figure 2.6. Each GHD illustrated in this Figure is an example of a square-term. These square-terms will be used as features and will be discussed in Chapter 3.

The cross-terms $\sum_{j=1}^{M-1}\sum_{l=j+1}^{M} 2C_3(j)C_3(l)\xi(j,f)\xi(l,f)\cos(C_4(j)-C_4(l)+\psi(j,f)-\psi(l,f))$ are a multiple of two GHD's of different order. The magnitude of the cross-terms is of the form $\xi(j,f)\xi(l,f) = e^{\frac{-2\pi^2\sigma^2}{j\gamma^2}(f-j[f_0+\mu k])}e^{\frac{-2\pi^2\sigma^2}{l\gamma^2}(f-l[f_0+\mu k])}$. If minimal overlap exists between the GHD, then the product is approximately zero. For example, closer examination of Figure 2.6 illustrates that each GHD is well separated and has no overlap. A minimal overlap condition is defined as

$$\xi(j,f)\xi(l,f) = \epsilon \tag{2.35}$$

where $\epsilon \simeq 0$, and $l > j$. Note that since $\xi(j,f)$ and $\xi(l,f)$ are both Gaussian functions, $\epsilon \neq 0$. An example of an overlap between two GHD's is shown in Figure 2.7, where $Y1 = e^{\frac{-(f-1)^2}{2}}$ and $Y2 = e^{\frac{-(f-5)^2}{2}}$. As is shown, the amount of overlap is small relative to the amplitude of $Y1$ and $Y2$ and has a maximum at the intercept point f_{int}. Equation 2.35 is considered at the intercept point $f = f_{int}$. The intercept occurs when $\xi(j,f_{int}) = \xi(l,f_{int})$. Solving for f_{int} yields

$$f_{int} = \frac{\mu_\xi(l)\sigma_\xi(j) + \mu_\xi(j)\sigma_\xi(l)}{\sigma_\xi(j) + \sigma_\xi(l)} \tag{2.36}$$

where $\mu_\xi()$ is defined by Equation 2.33 and $\sigma_\xi()$ is defined by Equation 2.34. The derivation of f_{int} is shown in Appendix D. If $f = f_{int}$, then Equation 2.35 reduces to

$$\epsilon = \frac{(\sigma_\xi(j) + \sigma_\xi(l))^2}{(\mu_\xi(l) - \mu_\xi(j))^2} \tag{2.37}$$

where $\mu_\xi(l) > \mu_\xi(j)$, $\sigma_\xi(j) > 0$, and $\sigma_\xi(l) > 0$. The derivation of Equation 2.37 is shown in Appendix D. This condition states that as ϵ decreases, $(\mu_\xi(l) - \mu_\xi(j))$ increases (i.e., the GHD's become more separated causing less overlap). Therefore as ϵ decreases, $(\sigma_\xi(j) + \sigma_\xi(l))$ decreases (i.e., the variance of the GHD's decreases causing less overlap).

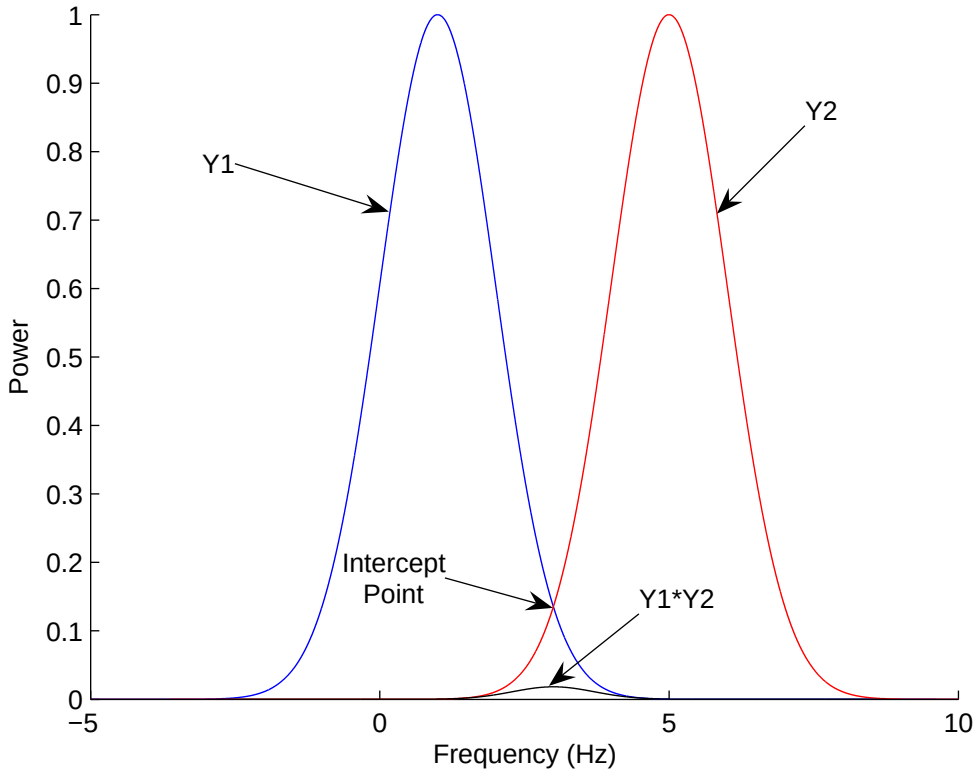

Fig. 2.7. Multiplication of Two Gaussian Functions. The Overlap is Dependent on the Intercept Point. As is Illustrated, $Y1 * Y2$ is the Multiplication of $Y1$ and $Y2$.

2.2.1 Estimation of the Filter Response Using the Gaussian Chirp Probe Signal.

In addition to the GHD generated by the nonlinearity, the Gaussian chirp signal can also be used to estimate the filter response of a circuit. Estimation of the filter response is useful if the probe signal is filtered before input into a nonlinearity.

As discussed in Section 1.5 of Chapter 1, the filter is assumed to be known a priori. The Gaussian chirp signal can be designed to estimate the filter response. The design requires that the passband of the filter is within the frequency band (i.e., f_0 to f_1) of the Gaussian chirp signal. For example, considered the Gaussian chirp signal used in the simulations of Chapter 5 and shown in Figure 2.8, where $f_0 = 1$Hz, $f_1 = 2GHz$, $\mu = 1.5x10^{-5}$, $\sigma = 3.5x10^{-6}$, and $t_1 = 50$ microseconds. As demonstrated in the simulations, this probe signal can be used to estimate a filter with a passband of 400MHz - 450MHz. An example of an estimated filter response is shown in Figure 2.9.

2.3 Linear Chirp Probe Signal

As mentioned above in Section 2.2.1, the windowed linear chirp probe signal can be used to estimate the filter response. In the same way, a linear chirp probe signal (not windowed) can also be used to estimate the filter response. The linear chirp signal will be used in Section 5.4 of Chapter 5 to estimate the filter response of two Chebyshev filters. The nonlinearity of the RF device is not considered. The linear chirp signal is

$$x(t) = Acos(2\pi(f_0 + \frac{(f_1 - f_0)}{2t_1}t)t) \tag{2.38}$$

where A is the amplitude, f_0 is the initial frequency at time $t = 0$, f_1 is the final frequency at time t_1. The output signal $y(t)$ is generated when $x(t)$ is input into a filter as shown in Figure 2.10. An example filter response of a actual filter is shown in Figure 2.11. This filter is a K&L Microwave 5MC10-500/T25-O/O 5th-

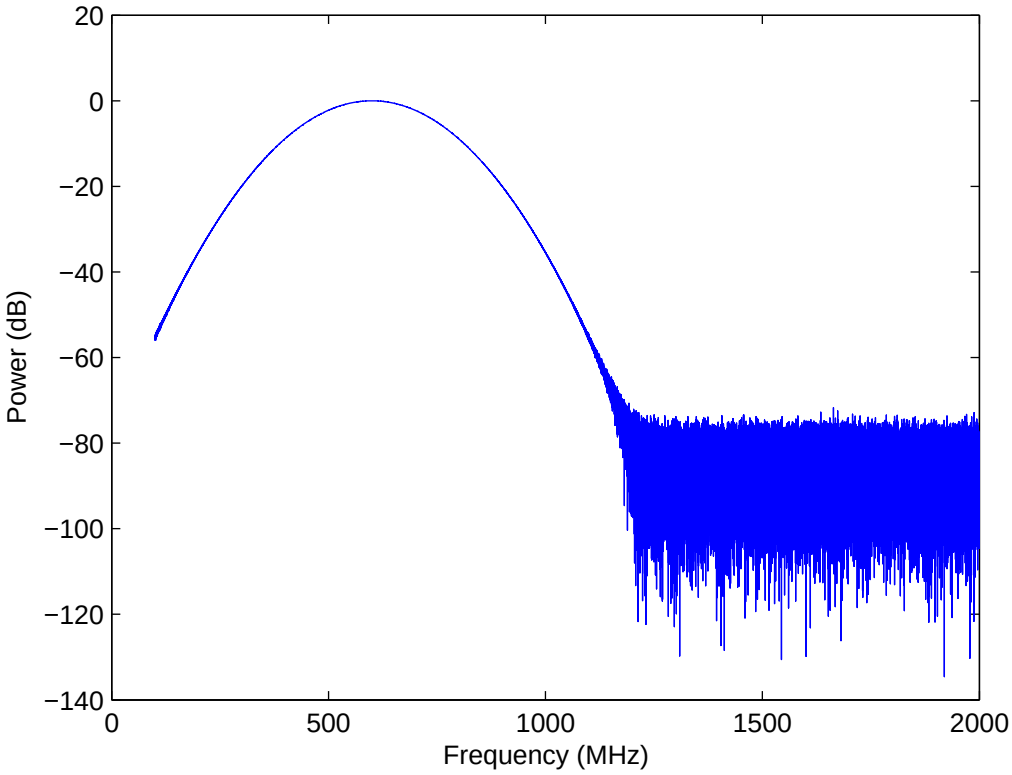

Fig. 2.8. Example Fourier Transform of the Gaussian Chirp Probe Signal.

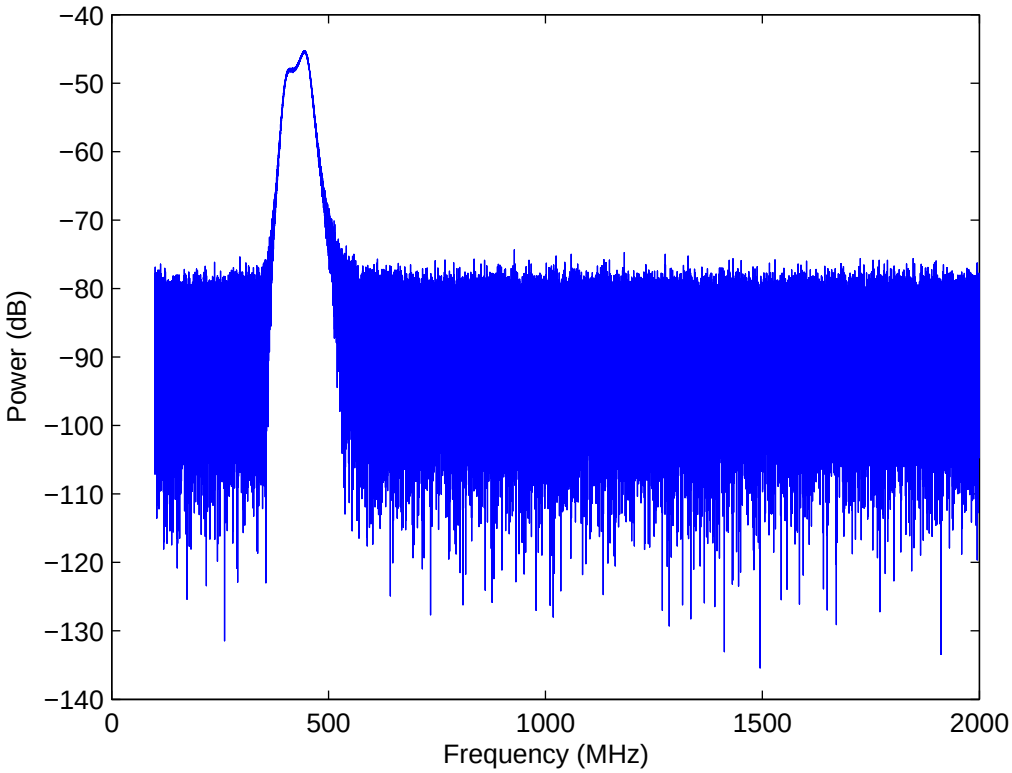

Fig. 2.9. Example Response of a Filter Using a Passband Between 400MHz and 450MHz. This Filter is Probed Using the Gaussian Chirp Probe Signal.

order Chebyshev filter with a center frequency of 500MHz, a passband of 25MHz, and a passband ripple of 0.05dB. The probe signal used to generate this filter response is a linear chirp probe signal with $f_0 = 495$MHz, $f_1 = 505$MHz, and $t_1 = 1000$ nanoseconds. As is illustrated, the passband ripple of this filter has a distinct pattern in the frequency range 495MHz - 505MHz. The passband presented in this Figure indicates that it may be possible to characterize the output signal of the filter based on these ripple patterns.

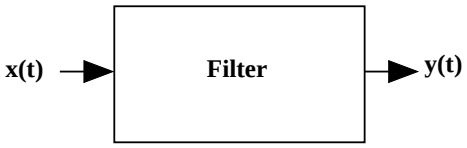

Fig. 2.10. Linear Chirp Signal is Input into a Filter. The Output Signal Contains an Estimate of the Filter Response.

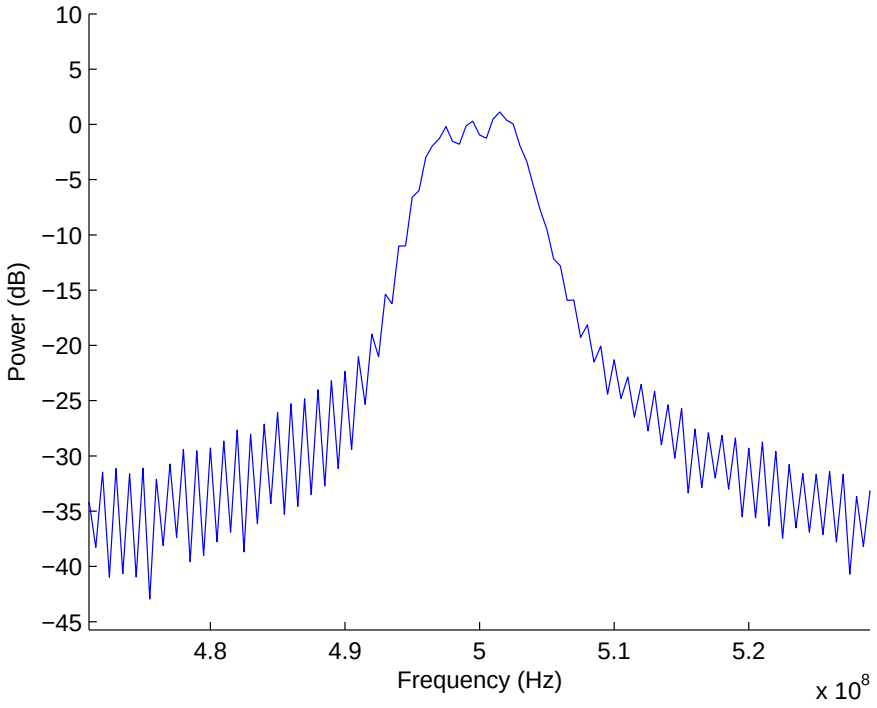

Fig. 2.11. Example Power Spectrum of the Filter Response for a K&L Microwave Filter.

3. FEATURES FOR DEVICE CHARACTERIZATION

After the RF device is probed, a response is reradiated by the device back to a receiver. Information, or features, are extracted from the returned signal and used to determine which type of RF device has been probed. The features should be distinct information inherent to the device. These features will then be used by classification techniques developed in the areas of pattern recognition and machine learning to determine which RF circuit was probed from a class of potential devices. Classification systems as discussed in more detail in Chapter 4.

In general the features used will be of two types, features corresponding to power at discrete frequencies caused by distortion or features that are related in the filter response in the RF circuit. For each of the three probe signals introduced in Chapter 2, different features will be used. For example, the features for the two-tone probe signal are power/energy of the intermodulation distortion (IMD) at discrete frequencies in the power spectrum of the return signal. The Gaussian chirp signal is used to estimate the filter response of the RF device and is also used to generate harmonic distortion. The amplitudes in the passband of the filter response and the amplitudes of the harmonic distortion will be used as features in this case. Finally, the features for the linear chirp signal are also amplitudes of the passband of the filter response.

3.1 Features For The Two-Tone Probe Signal

It was shown in Section 2.1 that, when a two-tone probe signal is input into a nonlinearity, first order distortion (FOD) and IMD occurs in the return signal $r(t)$ and is located at discrete (and deterministic) frequencies. The power in the FOD and IMD are inherent to the nonlinearities and will be used as features to characterize the RF device. The power in the FOD and IMD are obtained by sampling the power

spectrum of $r(t)$, $P_r(f)$, at the FOD and IMD frequency locations and using this power as features. For a given $P_r(f)$, 2 FOD's and 2 third order IMD's are considered. The discrete frequency locations are $\rho_1 = f_1$, $\rho_2 = f_2$, $\rho_3 = (2f_1 - f_2)$, and $\rho_4 = (2f_2 - f_1)$. Where f_1 and f_2 are the two probe frequencies as described in Chapter 2. Hence the 4 features are

$$e_g = P_r(\rho_g) \tag{3.1}$$

where $1 \leq g \leq 4$. Each feature of Equation 3.1 is modeled as a random variable, and will be denoted as $\mathbf{e}_g$ where $\mathbf{e}_g \in \Re$. Feature details are shown in Table 3.1. These features are used to form the random feature vector

$$\boldsymbol{\eta} = [\mathbf{e}_1 \ ... \ \mathbf{e}_4] \tag{3.2}$$

3.2 Features for the Windowed Linear Chirp Probe Signal

Similar to the two-tone probe discussed above, the harmonic distortion generated by the windowed linear chirp probe signal, or the Gaussian chirp signal, is also located at deterministic frequencies. The distortion is dependent on the parameters of the window function. If an input filter is present in the RF circuit before the nonlinearity,

Table 3.1
Four Features Used for the Two-Tone Probe Signal.

Feature	Feature Location	Feature Value
$\mathbf{e}_1$	$\rho_1 = f_1$	$e_1 = P_r(\rho_1)$
$\mathbf{e}_2$	$\rho_2 = f_2$	$e_2 = P_r(\rho_2)$
$\mathbf{e}_3$	$\rho_3 = 2f_1$-f_2	$e_3 = P_r(\rho_3)$
$\mathbf{e}_4$	$\rho_4 = 2f_2$-f_1	$e_4 = P_r(\rho_4)$

the shape of the filter response can also used for features (assuming the filter response is known a priori).

Two techniques are considered for sampling the power spectrum of the return signal to create features. Both techniques are used in the simulations described in Section 5.3. In the first technique, the power spectrum is sampled using a fixed pattern in the frequency domain. An example is shown in Figure 3.1 for the case when no filters are present in the circuit. If the filters are present, the same approach is used. An example is shown in Figure 3.2. In the second technique, the power spectrum is sampled at precise fixed locations. An example is shown in Figure 3.3 for the case when no filters are present in the circuit. The peak location of the distortion is sampled and used as features. The peak locations of the distortion are

$$\mu_\xi(j) = j[f_0 + \mu k] \tag{3.3}$$

$$\sigma_\xi^2(j) = \frac{j\gamma^2}{8\pi^2\sigma^2} \tag{3.4}$$

These are known a priori using the analysis of the return signal described in Section 2.2.1 of Chapter 2. If the filters are present, the same sampling technique is used. An example is shown in Figure 3.4. The filter response can be sampled at precise locations since the filter response is assumed to be known a priori.

Based on the above, consider a total of G features, sampled from the power spectrum $P_r(f)$ of the return signal. Define ρ to be the set of G frequencies $\rho = \{\rho_1, ...\rho_G\}$ corresponding to the frequency location of each feature. If the samples are determined at regular intervals, then $\rho_g = \rho_{g-1} + \Delta$ for $2 \leq g \leq G$, where Δ is a constant offset value. If samples are at precise locations, the set ρ must be determined based on Equations 3.3 and 3.4. Once ρ is determined, samples from the power spectrum (and the features) are

$$e_g = P_r(\rho_g) \tag{3.5}$$

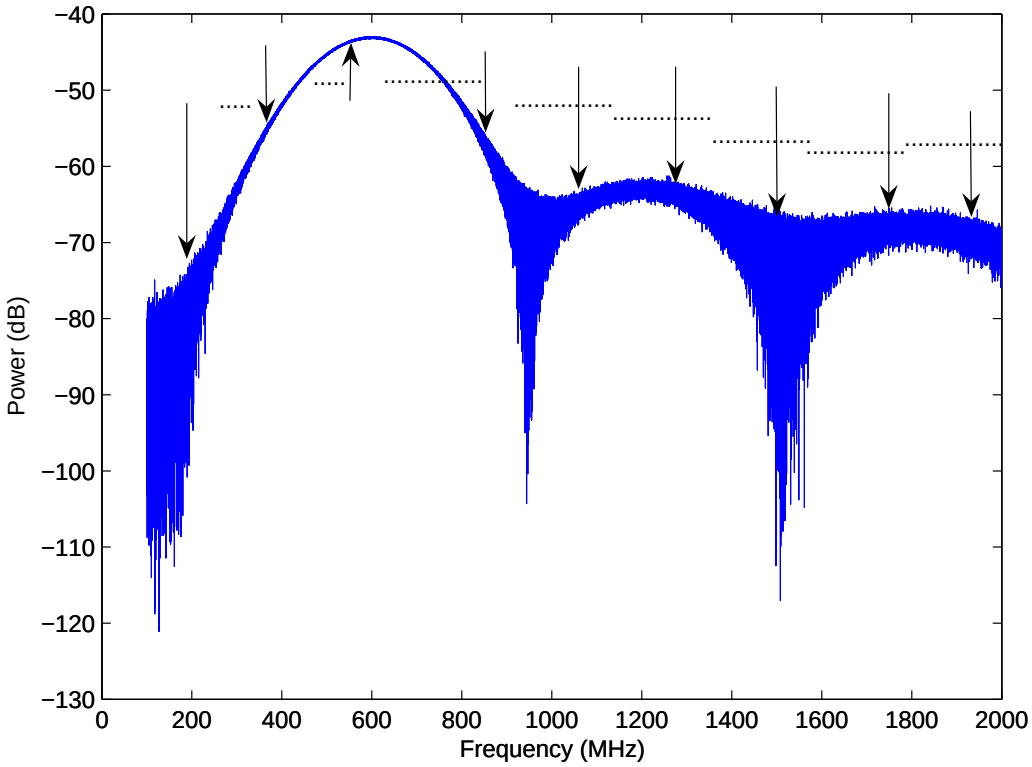

Fig. 3.1. Sampling Locations of the Power Spectrum at Regular Intervals (No Filter).

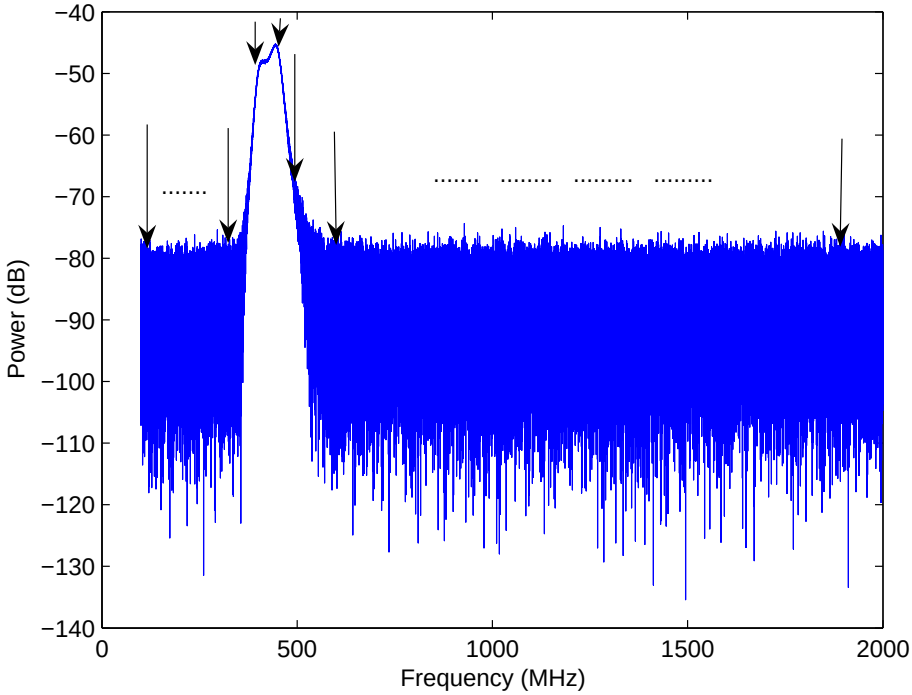

Fig. 3.2. Sampling Locations of the Power Spectrum at Regular Intervals (Filter Present).

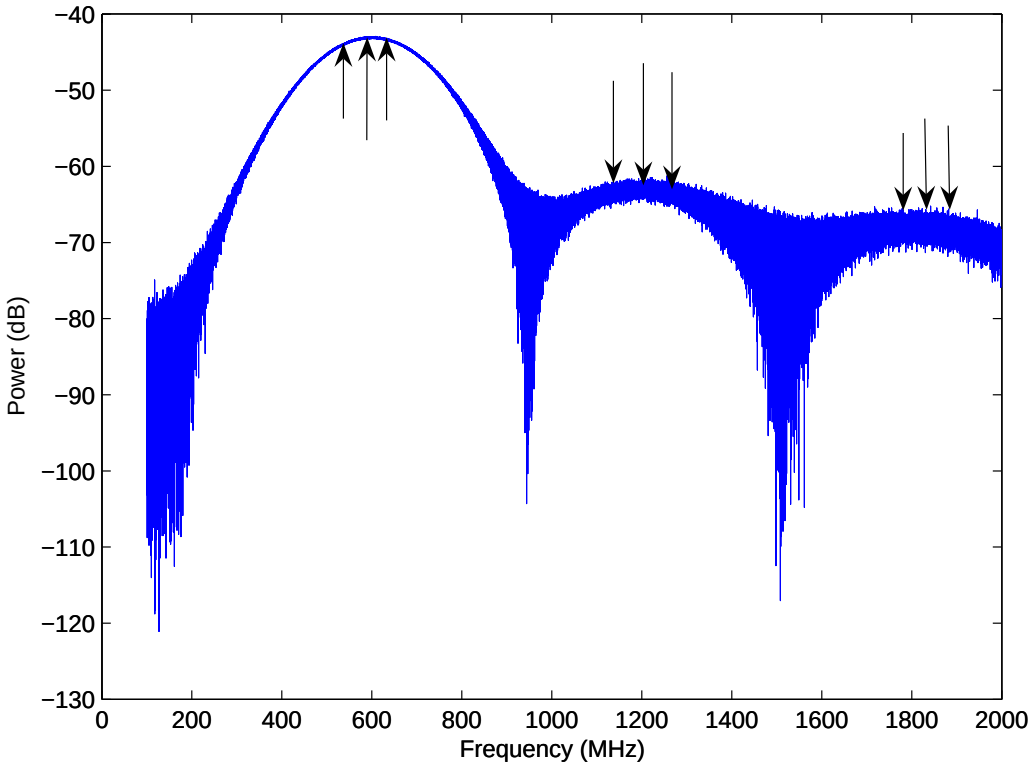

Fig. 3.3. Sampling Locations of the Power Spectrum at Precise Locations (No Filter).

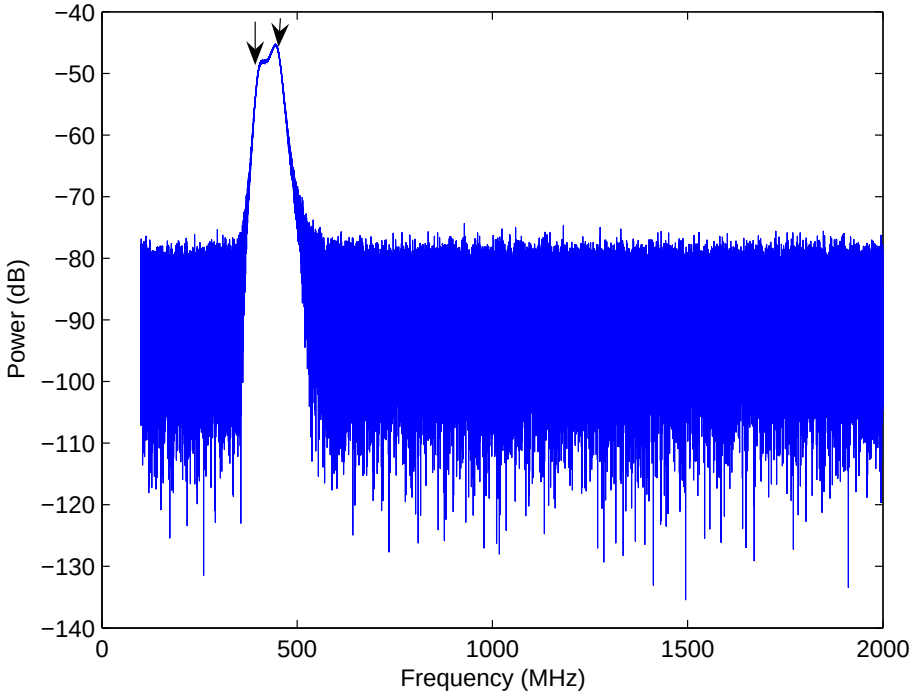

Fig. 3.4. Sampling Locations of the Power Spectrum at Precise Locations (Filter Present).

where $1 \leq g \leq G$. As mentioned in the above Section, the features are modeled as random variables that form the set $\{\mathbf{e}_1, ...\mathbf{e}_G\}$, where $\mathbf{e}_g \in \Re$. These features are used to form the random feature vector

$$\boldsymbol{\eta} = [\mathbf{e}_1 \ ... \ \mathbf{e}_G] \tag{3.6}$$

3.3 Features for the Linear Chirp Probe Signal

It was demonstrated in Section 2.3 how the linear chirp probe signal can be used to estimate the filter response of the circuit. The features introduced in this Section are obtained by sampling the filter response and scaling the samples at regular intervals as shown in Figure 3.5. Consider a total of G features, sampled from the power spectrum $P_r(f)$ of the return signal. Define the set of G frequency locations, $\rho = \{\rho_1, ...\rho_G\}$, where $\rho_g = \rho_{g-1} + \Delta$ for $2 \leq g \leq G$. Δ is a constant offset value. The features are

$$\varrho_g = P_r(\rho_g) \tag{3.7}$$

where $1 \leq g \leq G$. The samples form the set $\varrho = \{\varrho_1, ...\varrho_G\}$. The samples are then normalized from 0 to 1. Scaling the features maintains the "pattern" of passband ripple in the filter response. Each feature ϱ_g is scaled as follows

$$e_g = \frac{\varrho_g - min(\varrho)}{max(\varrho) - min(\varrho)} \tag{3.8}$$

where the function $min(\varrho)$ is the minimum value of ϱ and the function $max(\varrho)$ is the maximum value of ϱ. As mentioned above, the features are modeled as random variables that form the set $\{\mathbf{e}_1, ...\mathbf{e}_G\}$, where $\mathbf{e}_g \in \Re$. These features are used to form the following random feature vector

$$\boldsymbol{\eta} = [\mathbf{e}_1 \ ... \ \mathbf{e}_G] \tag{3.9}$$

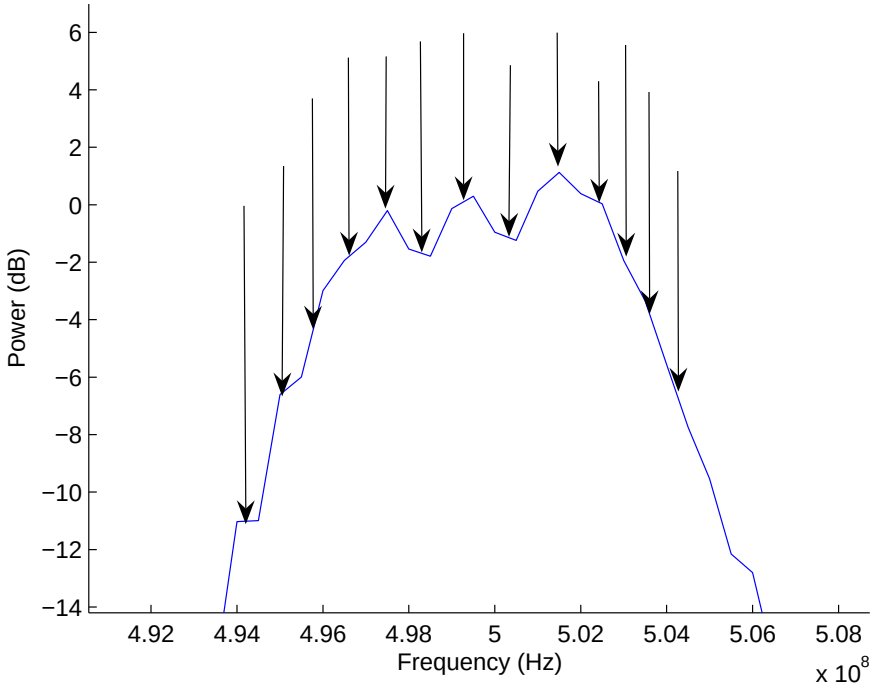

Fig. 3.5. Filter Response Sampled at Regular Intervals.

4. REVIEW OF CLASSIFIERS

This Chapter provides a review of classifiers that are used in a variety of pattern recognition and machine learning applications ranging from automatic speech recognition to the characterization of printers. This chapter provides a theoretical overview and an operational description of each classifier. Six classifiers are considered and are used in the simulations described in Chapter 5. The features discussed in Chapter 3 represent information that can be used to identify the RF device that was probed. The features presented in Chapter 3 were of two types, features corresponding to power at discrete frequencies in the return signal caused by distortion or features that are related in the filter response in the RF circuit. These features are considered as continuous random variables that form the set

$$\mathbf{e} = \{\mathbf{e}_1, \ ... \ \mathbf{e}_G\} \tag{4.1}$$

where G is the total number of features, $\mathbf{e}_g \in \Re$, where $g \in \{1, ...G\}$. The bold notation is used in this dissertation to denote random variables and random vectors. The features form the feature vector

$$\boldsymbol{\eta} = [\mathbf{e}_1 \ ... \ \mathbf{e}_G] \tag{4.2}$$

The features are used by classifier, which maps observed features into a label or category, representing an RF device from a set of D potential devices. For example $D = 2$ would correspond to a situation where one was interested in identifying an RF circuit from one of two potential circuits. The set of RF devices are defined as

$$\boldsymbol{\Upsilon} = \{\boldsymbol{\Upsilon}_1, ...\boldsymbol{\Upsilon}_D\} \tag{4.3}$$

where $\boldsymbol{\Upsilon}_d$ would correspond to a particular RF device or circuit, and $d \in \{1, ...D\}$. We assume the devices have equal probability of occurring, $P(\boldsymbol{\Upsilon}_d) = \frac{1}{D}$.

All the classifiers considered in this dissertation must first be trained. By training, the classifier "learns" how to map the features into the category or label. The training is not perfect and the classifier will make mistakes in actual operation by assigning the wrong label to an observed feature vector. Training the classifier has two goals. One goal is to determine how it will assign labels to observed feature vectors and the other is to estimate its error performance or its classification accuracy. This is accomplished by using a set of feature vectors where the label or category is known a priori. This is sometimes referred to as "ground truth" information. This ground truth information is divided into two sets, a training set and a testing set. The training set or data is used to train the classifier and the testing set or data is used to test the error performance of the classifier.

For training, a set of J observations is considered. Each observation consists of a feature vector, known as the training vector, and a label or category from the ground truth data. The training vector is defined as

$$\boldsymbol{\theta}_j = [\mathbf{e}_{(tr,j,1)} \ ... \ \mathbf{e}_{(tr,j,G)}] \tag{4.4}$$

where $\boldsymbol{\theta}_j \in \Re^G$. The feature $\mathbf{e}_{(tr,j,g)}$ in Equation 4.4 uses the notation from Equation 4.2 to denote the j^{th} vector in the set of training vectors. The label or category, $\tau_j \in \{1, ...D\}$ (ground truth), of the training vector, $\boldsymbol{\theta}_j$, denotes a particular RF device defined in Equation 4.3, where $\tau_j = d$ is the label for the RF device Υ_d. The training set is defined as

$$\boldsymbol{\Theta} = \{[\boldsymbol{\theta}_1, \tau_1], ...[\boldsymbol{\theta}_J, \tau_J]\} \tag{4.5}$$

where $[\boldsymbol{\theta}_j, \tau_j]$ is the j^{th} observation in the training set. When dividing the ground truth information into the training set, the number of vectors per category will vary. Define the set $Q = \{Q_1, ...Q_D\}$ to be the number of vectors per category in the training set. Define $Q_d \in Q$ as the number of vectors with labels equal to Υ_d. The

classifier estimates the mapping of the features vectors to the labels, $\varphi : \boldsymbol{\theta}_j \Rightarrow \tau_j$ for each observation [83].

To test the accuracy of the classifier, the test data is used from the ground truth data. A test vector is defined as

$$\boldsymbol{\omega}_i = [\mathbf{e}_{(te,i,1)} \ ... \ \mathbf{e}_{(te,i,G)}] \tag{4.6}$$

The feature $\mathbf{e}_{(te,i,g)}$ in Equation 4.6 uses the notation from Equation 4.2. Each test vector has a ground truth label λ_i, where $\lambda_i \in \{1, ...D\}$ and $\lambda_i = d$ denotes the RF device $\boldsymbol{\Upsilon}_d$. We will consider a test set of I test vectors

$$\boldsymbol{\Omega} = \{[\boldsymbol{\omega}_1, \lambda_1], ...[\boldsymbol{\omega}_I, \lambda_I]\} \tag{4.7}$$

where $[\boldsymbol{\omega}_i, \lambda_i]$ is the i^{th} observation in the test set. Similar to the training set, the number of vectors per category varies in the test set. Define the set $R = \{R_1, ...R_D\}$ to be the number of vectors per category in the test set. Define $R_d \in R$ as the number of vectors with labels equal to Υ_d.

The trained classifier is then used to map the test vector into a label or category $\varphi : \boldsymbol{\omega}_i \Rightarrow \chi_i$, where $\chi_i \in \{1, ...D\}$ and $\chi_i = d$ denotes the RF device $\boldsymbol{\Upsilon}_d$. The mapping function φ was determined using the training set. This label may be incorrect. Let χ_i be known as the predicted label for $\boldsymbol{\omega}_i$ determined by φ.

Once a classification decision is made, the classification accuracy of the classifier can be measured for performance evaluation. The performance evaluation process is illustrated in Figure 4.1. To measure the accuracy of the classifier, χ_i is compared with the ground truth label λ_i using

$$I_f(i) = \begin{cases} 1 & , \quad \lambda_i = \chi_i \\ 0 & , \quad \text{else} \end{cases} \tag{4.8}$$

Hence the test set is used to measure classification accuracy. Accuracy is estimated for each RF device $\boldsymbol{\Upsilon}_d$. The accuracy of $\boldsymbol{\Upsilon}_d$ is measured by using observations from

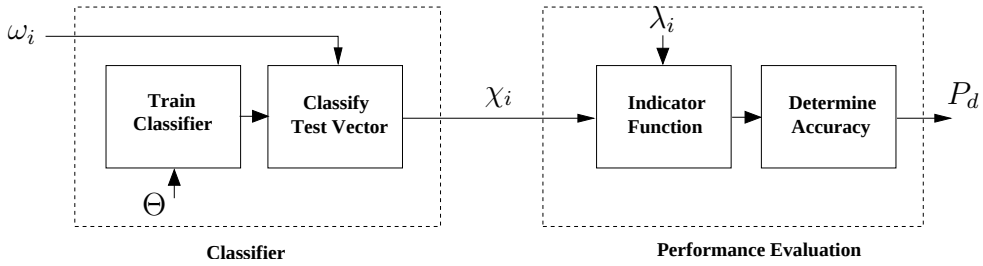

Fig. 4.1. Block Diagram of Performance Evaluation.

the test set that have the label $\lambda_i = d$. The average classification accuracy for $\boldsymbol{\Upsilon}_d$ is defined as

$$P_d = \frac{\sum_{\substack{i=1 \\ \lambda_i = d}}^{I} I_f(i)}{R_d} \tag{4.9}$$

P_d is used in Chapter 5 to evaluate the performance of the classifier.

4.1 Bayesian Classifiers

A Bayesian classifier is based on Bayes decision theory [51] where a posterior distribution $P(\boldsymbol{\Upsilon}_d|\boldsymbol{\omega}_i)$ is estimated. The Bayesian classifier determines the most probable category by comparing the posterior distribution of each category in $\boldsymbol{\Upsilon}$. For example, consider two RF devices, a garage door opener, $\boldsymbol{\Upsilon}_1$, and a walkie-talkie, $\boldsymbol{\Upsilon}_2$. For a given test vector $\boldsymbol{\omega}_i$, the Bayesian classifier would decide $\boldsymbol{\Upsilon}_1$ (garage door opener) if $P(\boldsymbol{\Upsilon}_1|\boldsymbol{\omega}_i) > P(\boldsymbol{\Upsilon}_2|\boldsymbol{\omega}_i)$. Otherwise, it would decide $\boldsymbol{\Upsilon}_2$.

In this Section, two Bayesian classifiers are introduced, which are known as the Bayesian$_\mu$ and Bayesian$_\Sigma$ classifiers. Both classifiers use the same decision procedure as described above. Bayes decision theory uses Bayes rule [84]

$$P(\boldsymbol{\Upsilon}_d|\boldsymbol{\omega}_i) = \frac{p(\boldsymbol{\omega}_i|\boldsymbol{\Upsilon}_d)P(\boldsymbol{\Upsilon}_d)}{p(\boldsymbol{\omega}_i)} \tag{4.10}$$

where

$$P(\boldsymbol{\Upsilon}_d) = \frac{1}{D} \tag{4.11}$$

has an equal probability distribution for each label, and

$$p(\boldsymbol{\omega}_i) = \sum_{d=1}^{D} p(\boldsymbol{\omega}_i|\boldsymbol{\Upsilon}_d)P(\boldsymbol{\Upsilon}_d) \tag{4.12}$$

is the probability of $\boldsymbol{\omega}_i$, and

$$p(\boldsymbol{\omega}_i|\boldsymbol{\Upsilon}_d) = \frac{e^{\frac{-(\boldsymbol{\omega}_i-\tilde{\boldsymbol{\mu}}_d)^T(\tilde{\boldsymbol{\Sigma}}_d)^{-1}(\boldsymbol{\omega}_i-\tilde{\boldsymbol{\mu}}_d)}{2}}}{(2\pi)^{\frac{G}{2}}|\tilde{\boldsymbol{\Sigma}}_d|^{\frac{1}{2}}} \tag{4.13}$$

is the conditional density function modeled as a the Gaussian distribution, where

$$\tilde{\boldsymbol{\mu}}_d = \frac{\sum_{\substack{j=1 \\ \tau_j=d}}^{J} \boldsymbol{\theta}_j}{Q_d} \tag{4.14}$$

and

$$\tilde{\boldsymbol{\Sigma}}_d = \frac{\sum_{\substack{j=1 \\ \tau_j=d}}^{J} (\boldsymbol{\theta}_j - \tilde{\boldsymbol{\mu}}_d)(\boldsymbol{\theta}_j - \tilde{\boldsymbol{\mu}}_d)^T}{Q_d - 1} \tag{4.15}$$

are parameters defined using the maximum likelihood (ML) estimate [85]. The parameter $\tilde{\boldsymbol{\mu}}_d$ is the mean vector of the Gaussian density function of size G. The parameter $\tilde{\boldsymbol{\Sigma}}_d$ is the covariance matrix of the Gaussian density function of size GxG. Note the conditions $\tau_j = d$ in Equations 4.14 and 4.15, which requires that only the training vectors from category $\boldsymbol{\Upsilon}_d$ are used to estimate $\tilde{\boldsymbol{\mu}}_d$ and $\tilde{\boldsymbol{\Sigma}}_d$.

4.1.1 Discriminate Functions

The decision rule used to classify the test vector $\boldsymbol{\omega}_i$ maximizes the posterior probability $P(\boldsymbol{\Upsilon}_d|\boldsymbol{\omega}_i)$. If two RF devices are considered, $D = 2$, then the decision rule uses a binary hypothesis test [51]. For the multi-category case, the decision rule uses a discriminate function [86]. The discriminate function is [84]

$$g_d(\boldsymbol{\omega}_i) = ln(p(\boldsymbol{\omega}_i|\boldsymbol{\Upsilon}_d)) + ln(P(\boldsymbol{\Upsilon}_d)) \tag{4.16}$$

where $g_d(\boldsymbol{\omega}_i)$ is a monotonically increasing function. χ_i is then determined as

$$\chi_i = \arg\max_d g_d(\boldsymbol{\omega}_i) \tag{4.17}$$

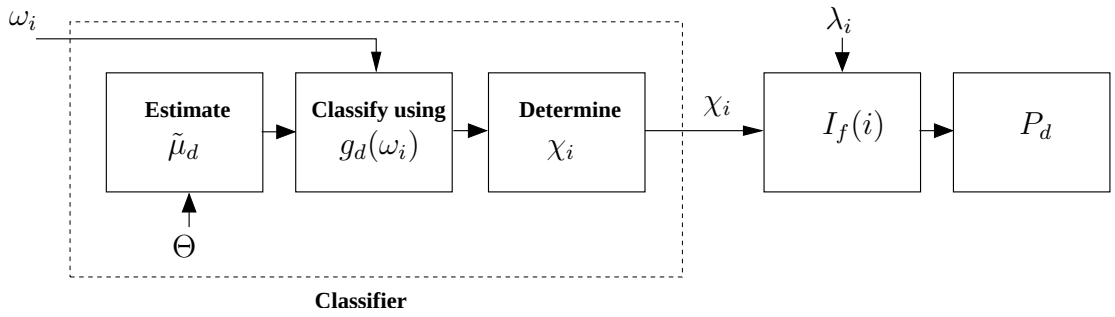

Fig. 4.2. Block Diagram of the Bayesian$_\mu$ Classifier and the Performance Evaluation Process.

4.1.2 Bayesian$_\mu$ Classifier

The first Bayesian classifier presented will be referred to as the Bayesian$_\mu$ classifier and is sometimes known as a distance classifier [51]. Bayesian$_\mu$ estimates the parameter $\tilde{\boldsymbol{\mu}}_d$ and defines $\tilde{\boldsymbol{\Sigma}}_d = \Sigma_I$ in Equation 4.13, where Σ_I is the identity matrix. The discriminate function of the Bayesian$_\mu$ classifier for a given test vector $\boldsymbol{\omega}_i$ is [84]

$$g_d(\boldsymbol{\omega}_i) = \frac{-(\boldsymbol{\omega}_i - \tilde{\boldsymbol{\mu}}_d)^T(\boldsymbol{\omega}_i - \tilde{\boldsymbol{\mu}}_d)}{2} - \frac{Gln(2\pi)}{2} + ln(\frac{1}{D}) \tag{4.18}$$

A block diagram of the Bayesian$_\mu$ classifier is shown in Figure 4.2. This block diagram also shows how the average classification accuracy P_d is measured. The parameter $\tilde{\boldsymbol{\mu}}_d$ is estimated using Equation 4.14. A test vector is input into the classifier and the discriminate function $g_d(\boldsymbol{\omega}_i)$ is determined using Equation 4.18. The predicted label χ_i is then determined using Equation 4.17. To determine the average classification accuracy measurement, the indicator function of Equation 4.8 compares χ_i to λ_i, and the average probability P_d of Equation 4.9 is measured for $\boldsymbol{\Upsilon}_d$.

4.1.3 Bayesian$_\Sigma$ Classifier

The second Bayesian classifier is known to as the Bayesian$_\Sigma$ classifier. The Bayesian$_\Sigma$ classifier estimates the parameters $\tilde{\boldsymbol{\mu}}_d$ and $\tilde{\boldsymbol{\Sigma}}_d$. The discriminate function of the Bayesian$_\Sigma$ classifier for a given test vector $\boldsymbol{\omega}_i$ is [84]

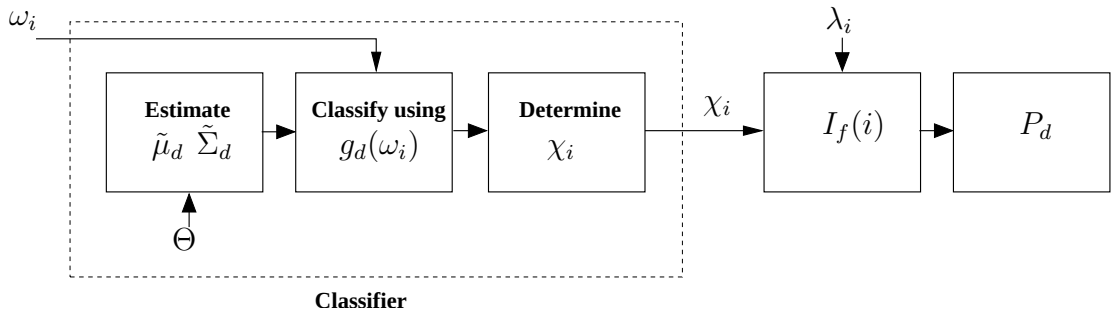

Fig. 4.3. Block Diagram of the Bayesian$_\Sigma$ Classifier and the Performance Evaluation Process.

$$g_d(\boldsymbol{\omega}_i) = \frac{-(\boldsymbol{\omega}_i - \tilde{\boldsymbol{\mu}}_d)^T(\tilde{\boldsymbol{\Sigma}}_d)^{-1}(\boldsymbol{\omega}_i - \tilde{\boldsymbol{\mu}}_d)}{2} - \frac{Gln(2\pi)}{2} - \frac{ln|\tilde{\boldsymbol{\Sigma}}_d|}{2} + ln(\frac{1}{D}) \qquad (4.19)$$

A block diagram of the Bayesian$_\Sigma$ classifier is shown in Figure 4.3. This block diagram also shows how the average classification accuracy P_d is measured. The parameter $\tilde{\boldsymbol{\mu}}_d$ is estimated using Equation 4.14 and the parameter $\tilde{\boldsymbol{\Sigma}}_d$ is estimated using Equation 4.15. The discriminate function $g_d(\boldsymbol{\omega}_i)$ is determined using Equation 4.19. The predicted label χ_i is then determined using Equation 4.17. To determine the average classification accuracy measurement, the indicator function of Equation 4.8 compares χ_i to λ_i, and the average probability P_d of Equation 4.9 is measured for $\boldsymbol{\Upsilon}_d$.

4.2 Parzen Window Classifier

The Parzen window (PW) classifier [51] estimates a density function in a local region around the test vector $\boldsymbol{\omega}_i$. The PW classifier discussed in this dissertation estimates a density function, $p_d(\boldsymbol{\omega}_i|\boldsymbol{\Upsilon}_d)$, for each category Υ_d [87]. The subscript d denotes Q_d, which is the number of training vectors that have the label $\tau_i = d$ [88]. The volume, V_d, of the local region is determined by a window function, $\varphi()$, with a window width, h_d. $p_d(\boldsymbol{\omega}_i|\boldsymbol{\Upsilon}_d)$ is estimated using the training vectors with a label $\tau_j = d$ that are within the window defined by the window function. For example,

consider the case when two training vectors, $\boldsymbol{\theta}_1$ and $\boldsymbol{\theta}_2$, fall within the window. Let $\boldsymbol{\theta}_1$ have the ground truth label $\tau_1 = 1$ and let $\boldsymbol{\theta}_2$ have the ground truth label $\tau_2 = 2$. For a given test vector $\boldsymbol{\omega}_i$, a density estimate $p_d(\boldsymbol{\omega}_i|\boldsymbol{\Upsilon}_1)$ is found using $\boldsymbol{\theta}_1$ and a density estimate $p_d(\boldsymbol{\omega}_i|\boldsymbol{\Upsilon}_2)$ is found using $\boldsymbol{\theta}_2$. The PW classifier decides Υ_1 if $p_d(\boldsymbol{\omega}_i|\boldsymbol{\Upsilon}_1)$ $> p_d(\boldsymbol{\omega}_i|\boldsymbol{\Upsilon}_2)$. Otherwise, Υ_2 is chosen. The PW density estimate of Υ_d is defined as [88] [84]

$$p_d(\boldsymbol{\omega}_i|\boldsymbol{\Upsilon}_d) = \sum_{\substack{j=1 \\ \tau_j=d}}^{J} \frac{1}{Q_d V_d} \varphi(\frac{\boldsymbol{\omega}_i - \boldsymbol{\theta}_j}{h_d}) \tag{4.20}$$

The density estimate $p_d(\boldsymbol{\omega}_i|\boldsymbol{\Upsilon}_d)$ converges to $p(\boldsymbol{\omega}_i|\boldsymbol{\Upsilon}_d)$ in quadratic mean if the window function $\varphi(\boldsymbol{U})$ and h_d are chosen under certain conditions [88] [89], where $\boldsymbol{U}$ is defined as $\boldsymbol{U} = [\boldsymbol{u}_1 ... \boldsymbol{u}_G]$ and $\boldsymbol{U} \in \Re^G$. For convergence, the window function must be nonnegative

$$\varphi(\boldsymbol{U}) \geq 0 \tag{4.21}$$

and [90]

$$\int_{-\infty}^{\infty} \varphi(\boldsymbol{U}) d\boldsymbol{U} = 1 \tag{4.22}$$

Other convergence conditions are [91] [86]

$$\sup_{\boldsymbol{U}} \varphi(\boldsymbol{U}) < \infty \tag{4.23}$$

$$\lim_{||\boldsymbol{U}|| \to \infty} \varphi(\boldsymbol{U}) \prod_{i=1}^{G} \boldsymbol{u}_i = 0 \tag{4.24}$$

$$\lim_{Q_d \to \infty} V_d = 0 \tag{4.25}$$

$$\lim_{Q_d \to \infty} Q_d V_d = \infty \tag{4.26}$$

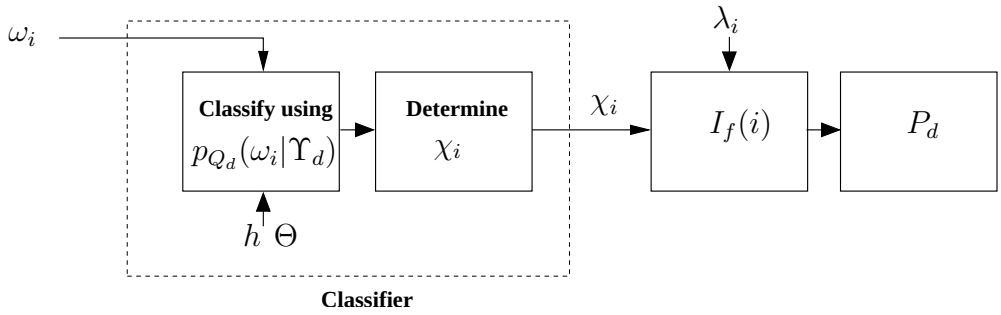

Fig. 4.4. Block Diagram of the Parzen Window Classifier and the Performance Evaluation Process.

We will use a zero-mean unit-variance Gaussian window function, which satisfies the convergence conditions [84] [88]. The PW density function using a Gaussian window is [87]

$$p_d(\boldsymbol{\omega}_i|\boldsymbol{\Upsilon}_d) = \sum_{\substack{j=1 \\ \tau_j=d}}^{J} \frac{e^{-\frac{(\boldsymbol{\omega}_i-\boldsymbol{\theta}_j)^T(\boldsymbol{\omega}_i-\boldsymbol{\theta}_j)}{2(h)^2}}}{(2\pi)^{\frac{G}{2}} Q_d(h)^G} \tag{4.27}$$

where h is a constant window width used for all categories. The predicted label χ_i is determined by

$$\chi_i = \arg\max_d p_d(\boldsymbol{\omega}_i|\boldsymbol{\Upsilon}_d) \tag{4.28}$$

A block diagram of the PW classifier is shown in Figure 4.4. This block diagram also shows how the classification accuracy P_d is measured. The window size h must be determined a priori and input into this algorithm. For the simulations in Chapter 5, several window sizes will be tested. $p_d(\boldsymbol{\omega}_i|\boldsymbol{\Upsilon}_d)$ is estimated by Equation 4.27. The predicted label χ_i is then determined using Equation 4.28. To determine the average classification accuracy, the indicator function of Equation 4.8 compares χ_i to λ_i, and the average probability P_d of Equation 4.9 is measured for $\boldsymbol{\Upsilon}_d$.

4.3 K Nearest Neighbor Classifier

Similar to the PW classifier, the K nearest neighbor (K-NN) classifier also estimates a density function in a local region around the test vector $\boldsymbol{\omega}_i$. However, instead of examining the number of training vectors that fall within a fixed window, the K-NN classifier examines the number of training vectors "nearest[1]" to the test vector. For example, consider classifying using two nearest neighbors. Define $\boldsymbol{\theta}_1$ and $\boldsymbol{\theta}_2$ as two training vectors nearest to the test vector $\boldsymbol{\omega}_i$. The first training vector has the ground truth label $\tau_1 = 1$ denoting Υ_1 and the other has ground truth label $\tau_2 = 2$ denoting Υ_2. A distance is found between each training vector and the test vector. Let the distance between $\boldsymbol{\theta}_1$ and $\boldsymbol{\omega}_i$ to be d_1. Let the distance between $\boldsymbol{\theta}_2$ and $\boldsymbol{\omega}_i$ to be d_2. The K-NN classifier decides Υ_1 if $d_1 < d_2$. Otherwise, Υ_2 is chosen. The density function estimate for the K-NN classifier is [92]

$$p_J(\boldsymbol{\omega}_i) = \frac{K_J}{JV_J} \tag{4.29}$$

where V_J is the volume of the local region, K_J is the number of nearest training vectors in the volume V_J, and J is the total number of training vectors. The subscript J is used, instead of d from the PW classifier, to indicate that all training vectors are used to estimate a posterior distribution [84]. Define K_d as the number of nearest training vectors with a label $\tau_i = d$. A posterior distribution is estimated as follows. First define the joint probability of $\boldsymbol{\Upsilon}_d$ and $\boldsymbol{\omega}_i$ as [93]

$$p_J(\boldsymbol{\Upsilon}_d, \boldsymbol{\omega}_i) = \frac{K_d}{JV_J} \tag{4.30}$$

Using Bayes rule [94]

$$p_J(\boldsymbol{\Upsilon}_d|\boldsymbol{\omega}_i) = \frac{p_J(\boldsymbol{\Upsilon}_d, \boldsymbol{\omega}_i)}{p_J(\boldsymbol{\omega}_i)} \tag{4.31}$$

The posterior distribution becomes [84]

[1]The nearest training vectors are determined using a distance function.

$$p_J(\boldsymbol{\Upsilon}_d|\boldsymbol{\omega}_i) = \frac{K_d}{K_J} \tag{4.32}$$

and is determined by substituting Equations 4.29 and 4.30 into Equation 4.31. The K_J training vectors nearest to the test vector are determined using the distance function: [95]

$$d(\boldsymbol{\theta}_j, \boldsymbol{\omega}_i) = \sqrt{(\mathbf{e}_{(tr,j,1)} - \mathbf{e}_{(te,i,1)})^2 + ... + (\mathbf{e}_{(tr,j,G)} - \mathbf{e}_{(te,i,G)})^2} \tag{4.33}$$

The training vectors that belong to the first K_J smallest distances are defined as the nearest neighbors.

A block diagram of the K-NN classifier is shown in Figure 4.5. This block diagram also shows how the classification accuracy P_d is measured. The number of nearest neighbors K_J must be known a priori and input into the algorithm. For the simulations in Chapter 5, several values of K_J are examined. A distance $d(\boldsymbol{\theta}_j, \boldsymbol{\omega}_i)$ is estimated by Equation 4.33 between all training vectors and the test vector. The K_J training vectors with the smallest distances are used as the nearest neighbors. The posterior density $p_J(\boldsymbol{\Upsilon}_d|\boldsymbol{\omega}_i)$ is estimated using Equation 4.32. The predicted label χ_i is estimated using

$$\chi_i = \arg\max_d p_J(\boldsymbol{\Upsilon}_d|\boldsymbol{\omega}_i) \tag{4.34}$$

To determine the average classification accuracy, the indicator function of Equation 4.8 compares χ_i to λ_i, and the average probability P_d of Equation 4.9 is measured for $\boldsymbol{\Upsilon}_d$.

4.4 Binary Tree Classifier

The binary tree (BT) classifier splits a single classification decision into a set of simpler binary decisions. Let the binary tree be T, where T is made up of several elements known as nodes, where a node is denoted as t. The starting node in the tree is the root node. The ending nodes in the tree are the terminal nodes. A classification

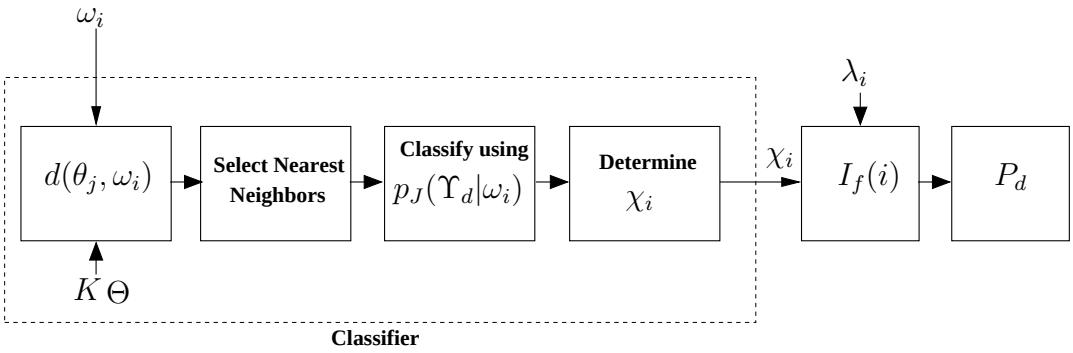

Fig. 4.5. Block Diagram of the K Nearest Neighbor Classifier and the Performance Evaluation Process.

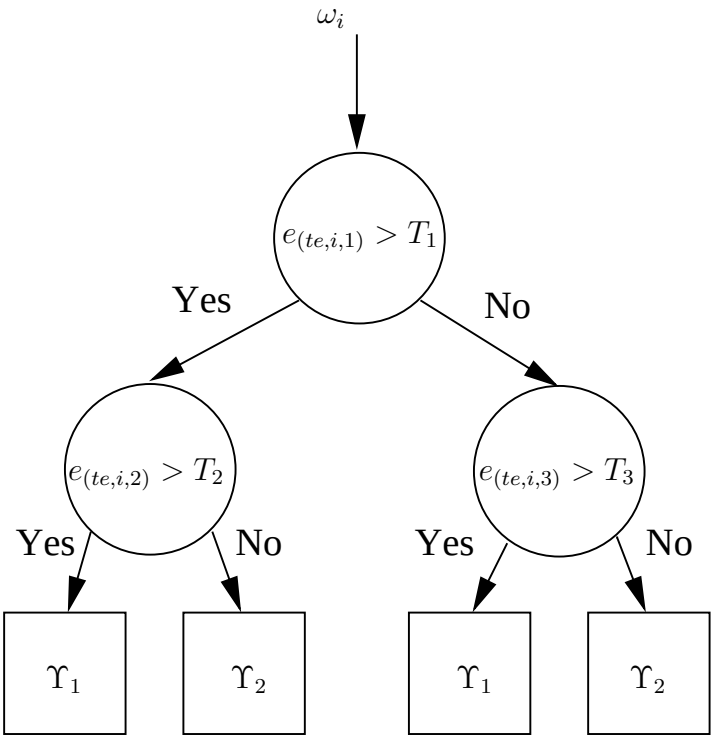

Fig. 4.6. Example of a Binary Tree. The Test Vector is Input into the Root Node and the Features are Compared to Thresholds. A Category is Decided at the Terminal Nodes.

decision is made at the terminal nodes. Each node, except for the terminal nodes, have at most two descendants or children. Only two children exist, a left and a right, for a given node in the binary tree. An example of a binary tree is shown in Figure 4.6 for a two category case, $\{\Upsilon_1, \Upsilon_2\}$. This example is used only for illustration purposes. This tree is grown from the training data, and the threshold values T_1, T_2, and T_3 are estimated during training. As shown, the test vector $\boldsymbol{\omega}_i$ is input into the root node. If the feature $\mathbf{e}_{(te,i,1)} > T_1$, then $\boldsymbol{\omega}_i$ is sent to the left child, otherwise it is sent to the right child. This process continues until a terminal node is reach, which is represented by the square block in the Figure. A category is chosen at the terminal node.

A common tree growing method is known as the classification and regression tree (CART) procedure [96]. CART outlines a technique to grow a tree from the

training data. The CART framework consists of splitting nodes, labelling nodes, and determining terminal nodes. A binary decision rule is used to split a node. The decision rule is determined based on an impurity measure [96]. Determining the terminal nodes is a critical procedure, which greatly affects the classification accuracy. Typically, instead of using a stopping criteria, a tree is grown to a very large size and then pruned [96]. The terminal nodes are labelled based on a majority vote.

4.4.1 Splitting Rule and Terminal Nodes

A binary decision is made at each node based on an impurity measure. One impurity measure is known as the Gini impurity measure [97]. The Gini impurity measure is defined as [84]

$$i(t) = \sum_{d \neq f}^{D} P(\boldsymbol{\Upsilon}_d|t) P(\boldsymbol{\Upsilon}_f|t) \tag{4.35}$$

where

$$P(\boldsymbol{\Upsilon}_d|t) = \frac{N_{(t,d)}}{N_t} \tag{4.36}$$

and $d \in \{1, ...D\}$, $f \in \{1, ...D\}$. N_t is the total number of training vectors in node t and $N_{(t,d)}$ is the total number of training vectors in node t that have the label $\tau_j = d$. $i(t)$ is the impurity at node t. The tree is grown so that the children are purer then the parent node. A splitting rule is defined as in [84] [98]

$$\Delta i(s_t, t) = i(t) - P_L i(t_L) - P_R i(t_R) \tag{4.37}$$

where s_t is defined as a split at node t, t_L and t_R are the left and right descendent nodes, $i(t_L)$ is the impurity measure of t_L, $i(t_R)$ is the impurity measure of t_R, P_L is the probability that the training vectors in node t are sent to t_L, and P_R is the probability that the training vectors in t are sent to t_R. The splitting rule requires that the impurity of a node is as large as possible. Define $s_t \in S$, where S is the set

of all possible splits. Then, define $s_{max} = \arg\max_{s_t}[\Delta i(s_t, t)]$ [98]. s_{max} is the split that generates the largest $\Delta i(s_t, t)$ and is used as the splitting rule for node t.

4.4.2 Pruning

The binary tree described in Section 4.4.1 is grown to full size, meaning a zero impurity measure is reached at all terminal nodes. The full size binary tree may be larger then necessary. Pruning [98] [96] is a technique used to reduce, or "trim," the binary tree. Pruning is started at the terminal nodes. The impurity is measured at the parent of a given terminal node. The impurity is again measured after removing the terminal node from the parent. If a small increase in impurity exists (close to 0 increase in impurity), then the terminal node is removed from the parent and the parent node becomes a terminal node [84]. This process is continued until all terminal nodes, including all newly transformed parent nodes, are examined.

4.4.3 Binary Tree Classifier

A block diagram of the BT classifier is shown in Figure 4.7. This block diagram also shows how the classification accuracy P_d is measured. The BT classifier generates the tree T using the algorithm described in [98–100]. "This algorithm randomly divides the training data into two sets, one to build the pure" terminal node tree "and the other to prune; then the roles of two sets are changed and the procedure iterates until converging to a smallest pruned subtree [99]." Once the tree is built using this procedure, a test vector $\boldsymbol{\omega}_i$ is input into the tree and the predicted label χ_i is determined. To determine the average classification accuracy, the indicator function of Equation 4.8 compares χ_i to λ_i, and the average probability P_d of Equation 4.9 is measured for $\boldsymbol{\Upsilon}_d$.

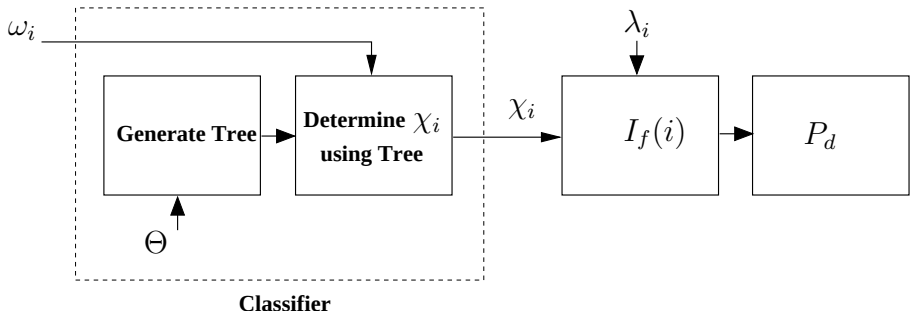

Fig. 4.7. Block Diagram of the Binary Tree Classifier and the Performance Evaluation Process.

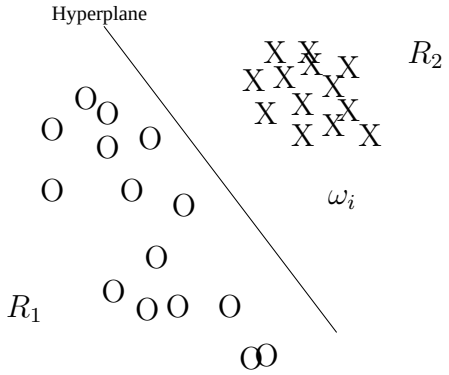

Fig. 4.8. Example of the Feature Space $\Re^2$ Used by the Support Vector Machine. The X's Denote the position of the Training Vectors in Region R_1 and the O's Denote the Position of the Training Vectors in Region R_2.

4.5 Support Vector Machines

A support vector machine (SVM) generates a hyperplane or separation boundary that separates the training data into two regions in the feature space $\Re^g$. For example, consider the two category case using training vectors of size $G = 2$ that are positioned in a feature space of size $\Re^2$ as illustrated in Figure 4.8. The hyperplane is positioned to separate training vectors with different labels into the regions R_1 and R_2. R_1 contains training vectors with the label $\tau_j = 1$ and the positions of these training vectors are denoted using X's. R_2 contains training vectors with the label $\tau_j = 2$ and the positions of these training vectors are denoted using O's. The test vector $\boldsymbol{\omega}_j$ is located in R_1, and is therefore assigned the label $\lambda_i = 1$.

For the theoretical development of the SVM, $D = 2$ classes are considered. The labels for the training vectors are defined as $\tau_j \in \{-1, 1\}$. The linear SVM defines a hyperplane [101]

$$(\mathbf{v} \cdot \boldsymbol{\theta}_j) + b = 0 \tag{4.38}$$

where $(\mathbf{v} \cdot \boldsymbol{\theta}_j)$ is the dot product between $\mathbf{v}$ and $\boldsymbol{\theta}_j$, $\mathbf{v} \in \Re^G$ is a random vector that is perpendicular to the hyperplane, $b \in \Re$ is defined as an offset value [83].

The training vectors are assumed to be linearly separable meaning that the training vectors satisfy the boundary conditions of the following Equations [102]

$$(\mathbf{v} \cdot \boldsymbol{\theta}_j) + b \geq +1 \qquad \tau_j = 1 \tag{4.39}$$

$$(\mathbf{v} \cdot \boldsymbol{\theta}_j) + b \leq -1 \qquad \tau_j = -1 \tag{4.40}$$

The training vectors on the boundaries, specified by $(\mathbf{v} \cdot \boldsymbol{\theta}_j) + b = +1$ for $\tau_j = 1$ and $(\mathbf{v} \cdot \boldsymbol{\theta}_j) + b = -1$ for $\tau_j = -1$, are defined as support vectors [84]. The margin between the two boundaries in Equations 4.39 and 4.40 must be maximized. A unique solution exists for maximizing the boundaries using Lagrange's theorem [103]:

$$L_D = \sum_{j=1}^{J} \alpha_j - \frac{1}{2} \sum_{k=1}^{J} \sum_{j=1}^{J} \alpha_k \alpha_j \tau_k \tau_j (\boldsymbol{\theta}_k \cdot \boldsymbol{\theta}_j) \tag{4.41}$$

where the constraints are defined by [102] [83]

$$0 \leq \alpha_j \leq C \tag{4.42}$$

$$\sum_{j=1}^{J} \alpha_j \tau_j = 0 \tag{4.43}$$

where $\{\alpha_1, ...\alpha_J\}$ are the Lagrange multipliers. The resulting decision function of the Lagrangian maximization procedure is [102]

$$f(\boldsymbol{\omega}_i) = \text{sign}[\sum_{j=1}^{J} \alpha_j \tau_j (\boldsymbol{\theta}_j \cdot \boldsymbol{\omega}_i)] \tag{4.44}$$

where, for $x \in \Re$,

$$\text{sign}[x] = \begin{cases} 1 & , \quad x \geq 0 \\ 0 & , \quad x < 0 \end{cases} \tag{4.45}$$

4.5.1 Nonlinear Support Vector Machine

A nonlinear SVM is used in place of the linear SVM if the training vectors are not linearly separable. The training vectors are separated by a nonlinear boundary. The nonlinear decision boundaries are determined by mapping the training vectors to some other Euclidian space H, $\Phi : \Re^G \Rightarrow H$, where the mapping function is denoted as Φ [83]. A hyperplane is then used in H to separate the mapped training vectors. The training vectors $\boldsymbol{\theta}_k$ and $\boldsymbol{\theta}_j$ of Equation 4.41 are mapped as $\Phi(\boldsymbol{\theta}_k)$ and $\Phi(\boldsymbol{\theta}_j)$, thereby replacing $(\boldsymbol{\theta}_k \cdot \boldsymbol{\theta}_j)$ as $\Phi(\boldsymbol{\theta}_k) \cdot \Phi(\boldsymbol{\theta}_j)$.

Mapping the training vectors to a higher dimension increases the complexity of the problem [104]. To avoid complexity, replace $\Phi(\boldsymbol{\theta}_k) \cdot \Phi(\boldsymbol{\theta}_j)$ by the kernel function $K(\boldsymbol{\theta}_k, \boldsymbol{\theta}_j) = \Phi(\boldsymbol{\theta}_k) \cdot \Phi(\boldsymbol{\theta}_j)$ [105], where the kernel function must satisfy Mercers condition [106].

The Lagrangian of Equation 4.41 is redefined for the nonlinear case by substituting $K(\boldsymbol{\theta}_k, \boldsymbol{\theta}_j)$ in the place of $(\boldsymbol{\theta}_k \cdot \boldsymbol{\theta}_j)$, which produces the same maximization problem. The Lagrangian for this problem is formulated as

$$L_D = \sum_{j=1}^{J} \alpha_j - \frac{1}{2} \sum_{k=1}^{J} \sum_{j=1}^{J} \alpha_k \alpha_j \tau_k \tau_j K(\boldsymbol{\theta}_k, \boldsymbol{\theta}_j) \tag{4.46}$$

under the same constraints of Equations 4.42 and 4.43. The Lagrangian is maximized under its constraints, which results in the decision function

$$f(\boldsymbol{\omega}_i) = \text{sign}[\sum_{j=1}^{J} \alpha_j \tau_j K(\boldsymbol{\theta}_j, \boldsymbol{\omega}_i)] \tag{4.47}$$

where sign[] is defined by Equation 4.45.

4.5.2 Support Vector Machine Classifier

The SVM classifier generates its training model using the LIBSVM library, which supports multi-class classification [107]. A multi-class SVM is easily extended from

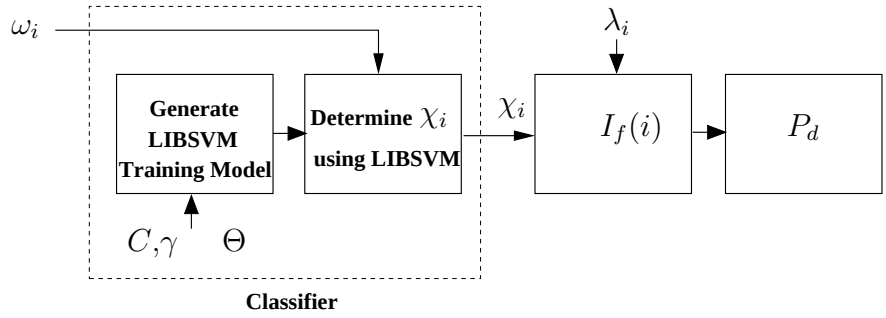

Fig. 4.9. Block Diagram of the Support Vector Machine Classifier and the Performance Evaluation Process.

the binary SVM discussed above [102]. The kernel function used in the SVM algorithm is the radial basis function (RBF)

$$K(\boldsymbol{\theta}_j, \boldsymbol{\omega}_i) = e^{-\gamma||\boldsymbol{\theta}_j - \boldsymbol{\omega}_i||^2} \tag{4.48}$$

which satisfies Mercers condition.

A block diagram of the SVM classifier is shown in Figure 4.5. This block diagram also shows how the classification accuracy P_d is measured. The LIBSVM library generates a training model using the parameters C and γ. C is the upper bound of the Lagrange multipliers and γ is a parameter in the RBF of Equation 4.48. C and γ must be input into the classifier. For the simulations in Chapter 5, several combinations of C and γ are tested. Once the LIBSVM training model is generated, a test vector $\boldsymbol{\omega}_i$ is classified by LIBSVM based on the generated training model. To determine the average classification accuracy, the indicator function of Equation 4.8 compares χ_i to λ_i, and the average probability P_d of Equation 4.9 is measured for $\boldsymbol{\Upsilon}_d$.

5. SIMULATIONS AND EXPERIMENTS

Three simulations and one experiment are presented in this Chapter. In the first simulation presented in Section 5.2, we develop a method to forensically characterize RF circuit models using first order distortion (FOD) and intermodulation distortion (IMD) generated by a nonlinearity in response to a two-tone probe signal. In the second simulation presented in Section 5.3, we develop methods to forensically characterize RF circuit models using harmonic distortion generated by nonlinearities in response to a Gaussian chirp signal. In this Section, we also develop methods to forensically characterize RF circuit models using the estimated filter response. In Section 5.4, we develop a method to forensically characterize actual physical RF circuits and circuit models using the filter response of two Chebyshev filters. The experimental results are compared with the simulations. Some of our results indicate that our simulation approach needs further investigation to validate it against actual measurement data.

5.1 RF Circuit Models

Three RF circuit models are introduced in this Section. Each circuit model is designed to simulate an RF device. A popular architecture that is widely used in RF devices is the superheterodyne architecture [108]. The superheterodyne architecture provides a high level of selectivity which is the ability to cancel out unwanted signals, and a high level of sensitivity which is the ability to detect small signals [12]. In some superheterodyne designs, the antenna is followed by a filter and then an amplifier [12]. When a probe signal is input into this superheterodyne architecture, it will be reflected by the amplifier since the amplifier is a source of a nonlinearity. A block diagram of this scenario is shown in Figure 5.1. This is simulated using the circuit model shown in

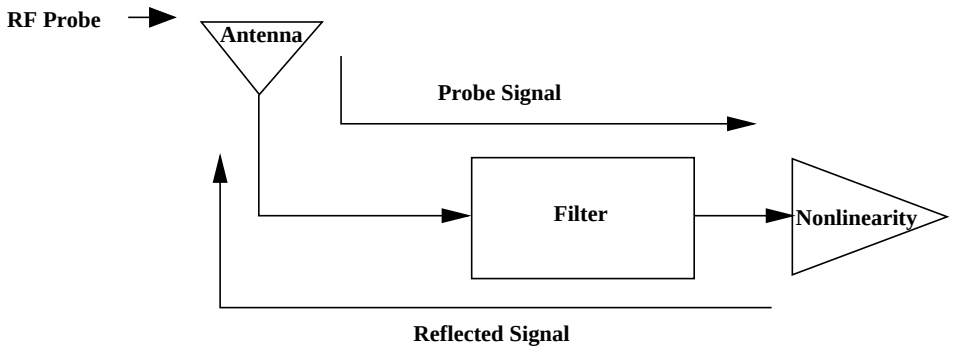

Fig. 5.1. RF Circuit with Filter Present.

Figure 5.2 [1], where $p(t)$ is the probe signal and $x(t)$ is the input into the nonlinearity. The nonlinearity is modeled empirically [2] and is represented by a power series of order M [109]

$$y(t) = \sum_{j=1}^{M} a_j [x(t)]^j \tag{5.1}$$

where $y(t)$ is the output of the nonlinearity. $d(t)$ is the output from the second filter that is added to the noise $n_c(t)$, and $r(t)$ is the return signal. The noise $n_c(t)$ is modeled as a white noise random process with a power spectrum, σ_c^2 [85]. The circuit models in the simulations of this Chapter will use random noise having multiple noise power spectrums. Multiple noise power spectrum are considered since it is possible that the noise in an RF device varies, this is typically dependent on the thermal level of the device [12] [108].

The two filters in Figure 5.2 are identical and assumed to be Chebyshev bandpass filters [8], which are common in RF circuits. The Chebyshev filter allows for flexible design of the filter response at the expense of complexity [110]. The Chebyshev filter has two main design features. The first is the passband ripple, which controls the quality of the passband, and the second is the rejection, which controls the quality of the stopband [110]. It is therefore possible to tradeoff passband quality with stopband quality.

[1]This circuit model was suggested by Professor Larry Carin of Duke University.

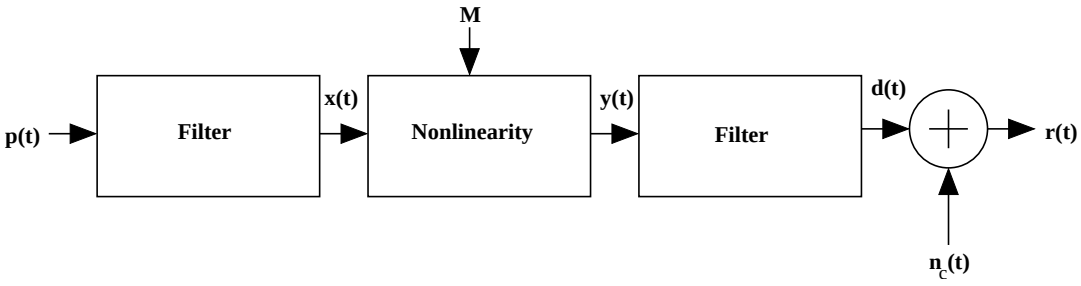

Fig. 5.2. RF Circuit Model - Filter Present.

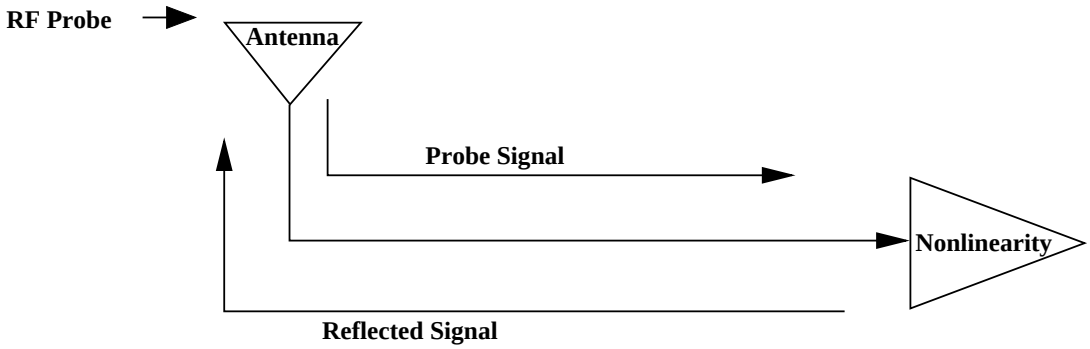

Fig. 5.3. RF Scenario - No Filter Present.

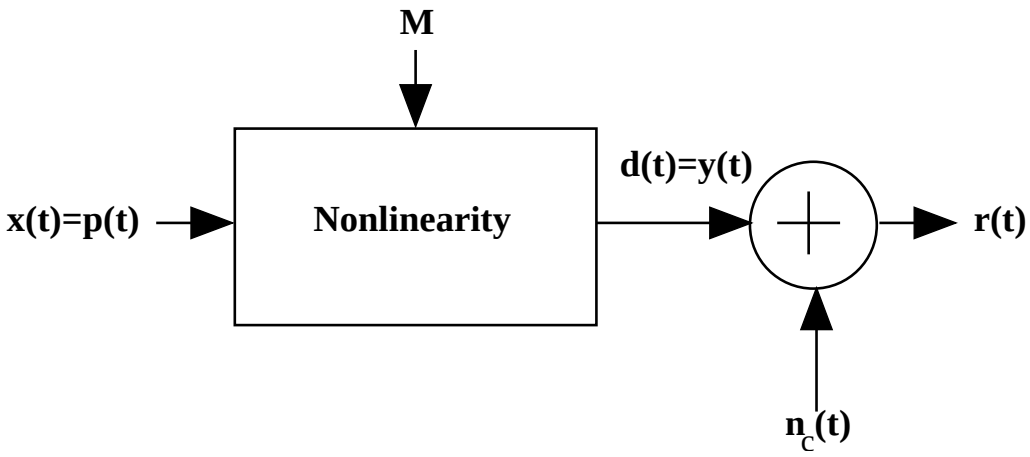

Fig. 5.4. RF Circuit Model - No Filter Present.

In other superheterodyne architectures, the antenna is followed directly by a amplifier [108], which is a source of a nonlinearity. When the probe signal is transmitted to this receiver, it is input into a nonlinearity and reflected. A block diagram of this scenario is shown in Figure 5.3. This scenario is simulated using the circuit model shown in Figure 5.4. Where $p(t)$ ($x(t) = p(t)$) is the probe signal that is input into the nonlinearity. The nonlinearity is modeled empirically [2] and is represented by the power series in Equation 5.1. $d(t)$ (where $d(t) = y(t)$) is the output of the nonlinearity that is added to the noise. The noise $n_c(t)$ is again modeled as a white noise random process with a power spectrum σ_c^2 and $r(t)$ is the return signal.

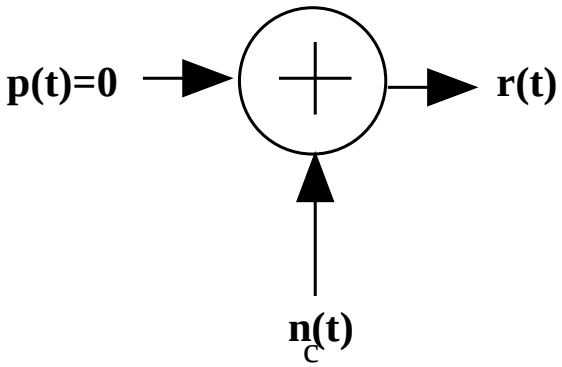

Fig. 5.5. Noise Model.

The final circuit model is the noise only model. This simulates the scenario when a probe signal is input into the RF circuit and only noise returns. This simulates the case when the probe does not incur any RF circuits. This model is shown in Figure 5.5. $p(t)$ is the probe signal that is added to the noise $n_c(t)$, where the noise is again modeled as a white noise random process with a power spectrum σ_c^2. $r(t)$ is the return signal. Note that $p(t) = 0$, and therefore $r(t) = n_c(t)$.

5.1.1 Signal to Noise Ratio

The definition of signal to noise ratio (SNR) for the circuit models is shown in this Section. The output signal (return signal) of the circuit models in Figure 5.2 and 5.4 is $r(t) = d(t) + n_c(t)$, where $d(t)$ is a deterministic signal and $n_c(t)$ is a white noise random process with a power spectrum σ_c^2. We will define SNR in terms of average signal power to average noise power [108]. Let the average power of $d(t)$ (signal) be [41] [9]

$$P_d = \lim_{T\to\infty} \frac{1}{T} \int_{-\frac{T}{2}}^{\frac{T}{2}} [d(t)]^2 dt \tag{5.2}$$

where $T = (t_2 - t_1)$ is the time interval from t_1 to t_2. The "noise power" will be assumed to be σ_c^2 [2]. The SNR of $r(t)$ is defined as [108]

$$\text{SNR} = \frac{P_d}{\sigma_c^2} \tag{5.3}$$

The SNR can also be expressed in dB or dBm:

$$\text{SNR}_{dB} = 10log_{10}(\frac{P_d}{\sigma_c^2}) \tag{5.4}$$

$$\text{SNR}_{dBm} = 10log_{10}(\frac{1000P_d}{\sigma_c^2}) \tag{5.5}$$

5.2 Two-Tone Signal Simulations

In this Section, we present a method to forensically characterize circuit models using first order distortion (FOD) and intermodulation distortion (IMD) generated by a nonlinearity in response to a two-tone probe signal. We are specifically interested in knowing how classification accuracy is effected by the power level of the FOD and IMD. For example, how is classification accuracy effected when the amplitude of the FOD and IMD is close to the noise floor?

The circuit models used in this simulation are based on the walkie-talkie experiment in Section 1.3 of Chapter 1. We will consider 6 circuit models, where one circuit model is the noise model. The noise model is shown in Figure 5.5. The other circuit models have a distinct nonlinearity and do not use filters as shown in Figure 5.4. No filters are considered in this simulation since we are only interested in the distortion caused by the nonlinearities. We will use 2 different noise power spectrums, $\{\sigma_{c_1}^2, \sigma_{c_2}^2\}$, in each circuit model. A set of two-tone probe signals are input into the circuit models. A set of return signals are generated by each circuit model in response to the

[2] σ_c^2 is not the true noise power since the power in a white noise process is undefined. We will use the spectral height of the white noise process as a measure of the power in the noise.

probe signals. The power spectrums of the return signals are obtained and features are sampled from the power spectrum and then classified.

5.2.1 Probe Signal Design

A set of two-tone probe signals were used in the walkie-talkie experiments in Section 1.3 of Chapter 1. Each two-tone signal of this experiment used different probe frequencies. The probe frequencies were chosen to be within the 240MHz - 500MHz frequency band. Following this approach, we will design a set of two-tone probe signals, $P = \{p_1(t), ...p_L(t)\}$, where

$$p_l(t) = \cos(2\pi\alpha_l t) + \cos(2\pi\beta_l t) \tag{5.6}$$

and $\alpha_l = 100x10^6 + (l-1)x10^6$, $\beta_l = \alpha_l + 0.1x10^6$, and $L = 901$. Note that the probe signals in P are in the 100MHz-1000MHz frequency band, which is a different band then that used in the two-tone experiment presented in Section 1.3 of Chapter 1. A wider band of frequencies are considered since we are using multiple circuit models instead of only one (i.e., the walkie-talkie). In a practical application, multiple RF devices will be present in the environment. Each RF device will operate within various frequency bands.

5.2.2 RF Circuit Model Design

As discussed at the start of this Section, six RF circuit models $\Upsilon = \{\Upsilon_1, ...\Upsilon_6\}$ are used to generate synthetic data. The circuit models $\{\Upsilon_1, ...\Upsilon_5\}$ have a distinct nonlinearity and do not use filters. Υ_6 is the noise only model. An example power spectrum of the return signal generated by each circuit model in response to the two-tone probe signal is shown in Figure 5.6, where the noise power spectrum $\sigma_c^2 = 5x10^{-13}$, $\alpha_{l=100} = 199x10^6$, and $\beta_{l=100} = 199.1x10^6$.

The circuit models $\{\Upsilon_1, ...\Upsilon_5\}$ are designed with nonlinearities that create distortion (FOD, harmonic distortion, IMD) at specified amplitudes based on the walkie-

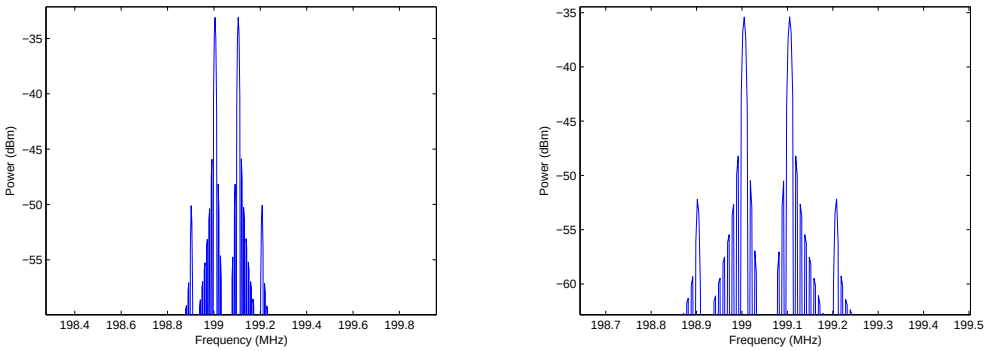

(a) Υ_1 (b) Υ_2

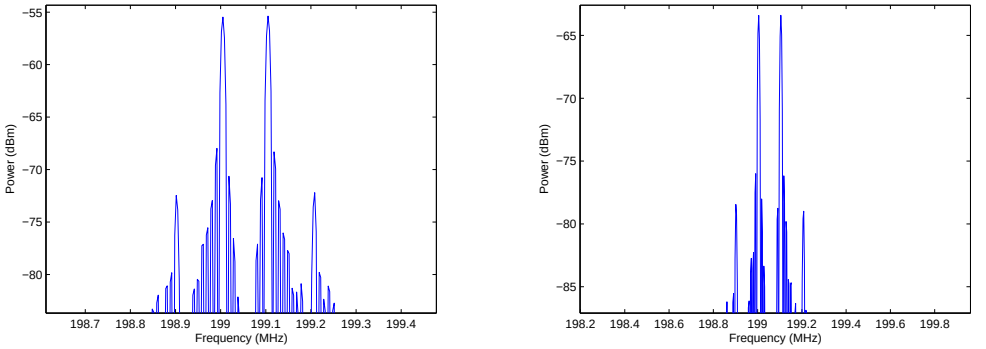

(c) Υ_3 (d) Υ_4

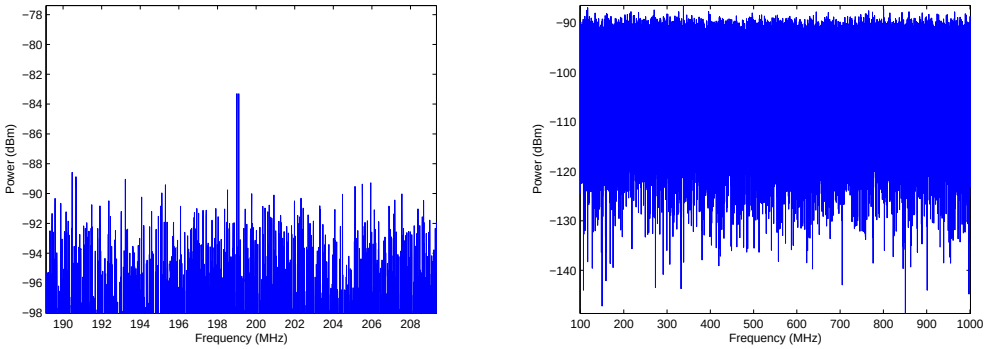

(e) Υ_5 (f) Υ_6

Fig. 5.6. Power Spectrums Generated by the 6 Circuit Models in Response to a Two-Tone Probe Signal.

Table 5.1
Power Series Coefficients Used by the Circuit Models in the Two-Tone Simulations.

	Υ_1	Υ_2	Υ_3	Υ_4	Υ_5
a_1	$2x10^{-6}$	$1.5x10^{-6}$	$0.15x10^{-6}$	$0.05x10^{-6}$	$0.0028x10^{-6}$
a_2	$0.1x10^{-6}$	$0.1x10^{-6}$	$0.1x10^{-6}$	$0.1x10^{-6}$	$0.1x10^{-6}$
a_3	$0.5x10^{-6}$	$0.4x10^{-6}$	$0.04x10^{-6}$	$0.02x10^{-6}$	$0.0028x10^{-6}$

talkie experiments. The coefficients used in the power series of Equation 5.1 are shown in Table 5.1 for each circuit model ($M = 3$). Υ_1 is designed to simulate the FOD and second order harmonic distortion of the walkie-talkie experiments. It was shown in Section 1.3 of Chapter 1 that the FOD was -31.5dBm and -30.33dBm and the second order harmonic distortion was -58.64dBm and -58.26dBm. It was also shown that the third order IMD was close to the noise floor. For these simulations, the third order IMD is used as features and will therefore be designed to have detectable amplitudes at -50 dBm for Υ_1. Υ_2 is designed to generate distortion amplitudes, in response to the two-tone signal, near Υ_1. This is done to determine if the classifiers can distinguish between circuit models that have similar features. Υ_3 is designed to produce unique distortion amplitudes, in response to the two-tone signal, that are well separated from the distortion amplitudes of the other circuit models. Υ_4 is also designed to produce unique distortion amplitudes, in response to the two-tone signal, that are well separated from the distortion amplitudes of the other circuit models. Υ_5 is designed to generate distortion, in response to the two-tone signal, close to the noise floor.

Multiple noise power spectrums are used in each circuit model. We will consider the following noise power spectrums: $\sigma_C^2 = \{\sigma_{c_1}^2 = 5x10^{-13}, \sigma_{c_2}^2 = 3x10^{-12}\}$. The notation $\sigma_{c_n}^2 \in \sigma_C^2$ is used to denote the n^{th} noise power spectrum, where $n \in \{1, ...N\}$ and $N = 2$.

5.2.3 Return Signals

The circuit models are used to generate simulated ground truth data in response to the set of two-tone probes signals in P. The set of probe signals is input into each of the six models using a noise power in σ_C^2. Each circuit model outputs L, $L = 901$, return signals. Each return signal will have a label, which is used to denote the model that produced the return signal. The return signal and label are the observations or ground truth data. Circuit model Υ_d, using the noise power spectrum $\sigma_{c_n}^2$, generates the follow set of ground truth data in response to the set P:

$$O_{(n,d)} = \{[r_{(n,d,1)}(t), \gamma_{(n,d,1)} = d], ...[r_{(n,d,L)}(t), \gamma_{(n,d,L)} = d]\} \tag{5.7}$$

where the notation d signifies the circuit model Υ_d and n signifies the noise power spectrum $\sigma_{c_n}^2$, $\gamma_{(n,d,l)}$ is the ground truth label, and $r_{(n,d,l)}(t)$ is the return signal generated in response to the probe $p_l(t)$. The set of observations produced by all circuit models utilizing both noise power spectrums is

$$O = \{O_{(1,1)}, ...O_{(1,6)}, O_{(2,1)}, ...O_{(2,6)}\} \tag{5.8}$$

Note that the total number of return signals is 10,812. For all the return signals in O from Equation 5.8, power spectrums are obtained. The power spectrums in $O_{(n,d)}$ are

$$P_{O_{(n,d)}} = \{[P_{r_{(n,d,1)}}(f), \gamma_{(n,d,1)} = d], ...[P_{r_{(n,d,L)}}(f), \gamma_{(n,d,L)} = d]\} \tag{5.9}$$

where

$$P_{r_{(n,d,l)}}(f) = R_{(n,d,l)}(f)[R_{(n,d,l)}(f)]^* \tag{5.10}$$

and

$$R_{(n,d,l)}(f) = \int_{-\infty}^{\infty} r_{(n,d,l)}(t) e^{-i2\pi ft} dt \tag{5.11}$$

The power spectrums form the set

$$P_O = \{P_{O_{(1,1)}}, ...P_{O_{(2,6)}}\} \tag{5.12}$$

We will next determine the average SNR for each set $P_{O_{(n,d)}}$ of power spectrums. First, by using Equation 5.5, we can define the SNR for the given power spectrum $P_{r_{(n,d,l)}}(f)$ as $SNR_{(n,d,l)}$, where $P_{r_{(n,d,l)}}(f) \in P_{O_{(n,d)}}$. Then, we will let the average SNR for the power spectrums in $P_{O_{(n,d)}}$ be

$$\text{ASNR}_{(n,d)} = \frac{\sum_{l=1}^{L} \text{SNR}_{(n,d,l)}}{L} \tag{5.13}$$

Note $d \neq 6$ in Equation 5.13 since the SNR is not determined for the noise model. In addition to the average SNR, we will also determine the average intermodulation distortion ratio (IMR) for each set $P_{O_{(n,d)}}$ of power spectrums. The IMR for the power spectrum $P_{r_{(n,d,l)}}(f) \in P_{O_{(n,d)}}$ is

$$IMR_{(n,d,l)} = \frac{P_{r_{(n,d,l)}}(2f_1 - f_2)}{P_{r_{(n,d,l)}}(f_1)} \tag{5.14}$$

Then, we will let the average IMR for the power spectrums in $P_{O_{(n,d)}}$ as

$$\text{AIMR}_{(n,d)} = \frac{\sum_{l=1}^{L} \text{IMR}_{(n,d,l)}}{L} \tag{5.15}$$

where $d \neq 6$ in Equation 5.15 since the SNR is not determined for the noise models. The average SNR and IMR for the circuit models is shown in Table 5.2. Note that $\text{ASNR}_{(1,5)}$ and $\text{ASNR}_{(2,5)}$ are low relative to the other average SNR values. Also note that $\text{AIMR}_{(1,5)}$ and $\text{AIMR}_{(2,5)}$ have large IMR's. This is caused by the high noise power used in circuit model Υ_5. As shown in Figure 5.6(e), the amplitude of the FOD is near the noise floor and the IMD is noise. Therefore, the ratio of the IMD to FOD increases.

Table 5.2
Average SNR and IMR for the RF Circuit Models Used in the Two-Tone Simulations.

	d=1	d=2	d=3	d=4	d=5
$\text{ASNR}_{(1,d)}$ (dBm)	44.5	42.2	22.5	15.3	2.4
$\text{ASNR}_{(2,d)}$ (dBm)	36.7	34.4	14.7	7.5	-5.4
$\text{AIMR}_{(1,d)}$	0.020	0.021	0.021	0.032	0.142
$\text{AIMR}_{(2,d)}$	0.020	0.021	0.022	0.035	0.510

5.2.4 Training and Testing

Features are extracted from each power spectrum in P_O of Equation 5.12. The method used for feature extraction was discussed in Section 3.1 of Chapter 3. Four amplitudes were sampled from a power spectrum and formed into a feature vector. For the set of power spectrums in P_O, the four features are extracted as follows:

$$e_{(k,1)} = P_{r_{(n,d,l)}}(\alpha_l) \tag{5.16}$$

$$e_{(k,2)} = P_{r_{(n,d,l)}}(\beta_l) \tag{5.17}$$

$$e_{(k,3)} = P_{r_{(n,d,l)}}(2\alpha_l - \beta_l) \tag{5.18}$$

$$e_{(k,4)} = P_{r_{(n,d,l)}}(2\beta_l - \alpha_l) \tag{5.19}$$

where, given any values of n, d, and l, $k = (n-1)DL + (d-1)L + l$, $k \in \{1, ...K\}$, and $K = 10,812$. The features form the feature vector

$$\boldsymbol{\eta}_k = [\mathbf{e}_{(k,1)}\ \mathbf{e}_{(k,2)}\ \mathbf{e}_{(k,3)}\ \mathbf{e}_{(k,4)}] \tag{5.20}$$

where $\boldsymbol{\eta}_k \in \Re^4$. Also, let $\Gamma_k = \gamma_{(n,d,l)}$. We can then order the feature vectors and labels as

$$\{[\boldsymbol{\eta}_1, \Gamma_1], ...[\boldsymbol{\eta}_K, \Gamma_K]\} \tag{5.21}$$

where $[\boldsymbol{\eta}_k, \Gamma_k]$ is the k^{th} observation. Each observation or ground truth set in Equation 5.21 is randomly divided into the training and testing ground truth sets. The training and testing sets were introduced in Chapter 4. Before dividing the observations in Equation 5.21, first let $\nu(k)$ be a random variable with a uniform distribution on the interval [0 1] indexed by the integer k [3]. For the k^{th} observation in Equation 5.21, we let

$$\begin{aligned} \{\boldsymbol{\theta}_j = \boldsymbol{\eta}_k,\, \tau_j = \Gamma_k\} \quad &, \quad \nu(k) \geq 0.5 \\ \{\boldsymbol{\omega}_i = \boldsymbol{\eta}_k,\, \lambda_i = \Gamma_k\} \quad &, \quad \nu(k) < 0.5 \end{aligned} \tag{5.22}$$

where $\boldsymbol{\theta}_j$ is the j^{th} training vector with label τ_j, and $\boldsymbol{\omega}_i$ is the i^{th} test vector with a label λ_i. The training vectors form the set

$$\boldsymbol{\Theta} = \{[\boldsymbol{\theta}_1, \tau_1], ...[\boldsymbol{\theta}_{\mathbf{J}}, \tau_{\mathbf{J}}]\} \tag{5.23}$$

Note that since we are randomly dividing the observations in Equation 5.21, $\mathbf{J}$ is a discrete random variable where $\mathbf{J} \in \{0, 1, ...K\}$. The test vectors form the set

$$\boldsymbol{\Omega} = \{[\boldsymbol{\omega}_1, \lambda_1], ...[\boldsymbol{\omega}_{\mathbf{I}}, \lambda_{\mathbf{I}}]\} \tag{5.24}$$

Also note $\mathbf{I}$ is a discrete random variable where $\mathbf{I} \in \{0, 1, ...K\}$ and $K = \mathbf{J} + \mathbf{I}$.

For the training set described by Equation 5.23, the number of total observations and the number observations per category are shown in Table 5.3, where $\mathbf{Q}_d \in \mathbf{J}$ was described in Chapter 4 as the number of observations that have the label $\tau_j = d$. For the test set defined in Equation 5.24, the total number of observations and the

[3]These simulations used the *MATLAB* function *rand()* to generate a pseudorandom number drawn from the uniform distribution.

Table 5.3
Number of Feature Vectors Per Category for the Training Set for the Two-Tone Simulations.

$\mathbf{J}$	$\mathbf{Q}_1$	$\mathbf{Q}_2$	$\mathbf{Q}_3$	$\mathbf{Q}_4$	$\mathbf{Q}_5$	$\mathbf{Q}_6$
5437	901	906	889	908	927	906

Table 5.4
Number of Feature Vectors Per Category for the Testing Set for the Two-Tone Simulations.

$\mathbf{I}$	$\mathbf{R}_1$	$\mathbf{R}_2$	$\mathbf{R}_3$	$\mathbf{R}_4$	$\mathbf{R}_5$	$\mathbf{R}_6$
5375	901	896	913	894	875	896

number observations per category are shown in Table 5.4, where $\mathbf{R}_d \in \mathbf{I}$ was defined in Chapter 4 as the number of observations that have the label $\lambda_i = d$.

5.2.5 Classification Results

We will measure the average classification accuracy for each circuit model in Υ. As discussed in Chapter 4, this accuracy is

$$P_d = \frac{\sum_{\substack{i=1 \\ \lambda_i = d}}^{I} I_f(i)}{R_d} \tag{5.25}$$

where

$$I_f(i) = \begin{cases} 1 & , \quad \lambda_i = \chi_i \\ 0 & , \quad \text{else} \end{cases} \tag{5.26}$$

is the indicator function and χ_i is the predicted label decided by the classifier. The K nearest neighbor (K-NN) classifier, Parzen window (PW) classifier, and support vector machine (SVM) require the selection of parameters prior to classification. For example, the K-NN classifier requires the number of nearest neighbors K_J. An

interesting question is: what value of K_J has the highest classification accuracy? To answer this question, we define π as a classifier parameter. For the K-NN classifier, $\pi = K_J$. To determine the value of the parameter that produces the highest classification accuracy, we will need to test several values of π. Define a set of parameter values as $\Pi = \{\pi_1, ...\pi_V\}$. The total number of parameter values in the set is denoted as V. For the K-NN classifier, assume we would like to test the following number of nearest neighbors: $K_J = 1$, $K_J = 2$, $K_J = 3$. The parameter set Π would therefore be defined as $\Pi = \{\pi_1 = 1, \pi_2 = 2, \pi_3 = 3\}$.

An average classification accuracy is determined for each parameter $\pi_v \in \Pi$. Define

$$P_{(ave,v)} = \frac{\sum_{i=1}^{\mathbf{I}} I_f(i)}{\mathbf{I}} \tag{5.27}$$

as the average classification accuracy of all categories using the parameter π_v. Next, let

$$v_{max} = \arg\max_{v} P_{(ave,v)} \tag{5.28}$$

The parameter $\pi_{v_{max}}$ is the parameter that yields the highest average classification accuracy of the circuit models, and is used by the classifier for the results that will be presented in this Section.

The K-NN classifier requires the number of nearest neighbors, K_J, prior to classification. Define the parameter set for the K-NN classifier as $\Pi = \{\pi_1 = 1, ...\pi_{50} = 50\}$, where the parameters correspond to the number of nearest neighbors used by the classifier. It was determined that $v_{max} = 24$, therefore $K_J = \pi_{24} = 24$. The PW classifier requires the window width, h, prior to classification. Define the parameter set for the PW classifier as $\Pi = \{\pi_1 = 0.1, \pi_2 = 0.3, ...\pi_{25} = 4.9\}$, where these parameters correspond to the window width used by the classifier. It was determined that $v_{max} = 10$, therefore $h = \pi_{10} = 1.9$. The SVM classifier requires two inputs C and γ prior to classification. Note that $C \in \{c_1 = 1, c_2 = 3, ...c_7 = 13\}$ and

Table 5.5
Average Classification Accuracies for the Two-Tone Simulations.

	P_1	P_2	P_3	P_4	P_5	P_6
SVM	100%	100%	100%	100%	92.1%	94.3%
BTC	100%	100%	100%	100%	91.4%	92.7%
Bayesian$_\mu$	100%	100%	100%	100%	99.3%	68.9%
Bayesian$_\Sigma$	100%	100%	100%	100%	93.6%	90.8%
PW	100%	100%	100%	100%	93.1%	93.6%
K-NN	100%	100%	100%	100%	93%	94%

$\gamma \in \{\gamma_1 = 0.01, \gamma_2 = 0.03, ...\gamma_{250} = 4.99\}$. Let the parameter set for the SVM classifier be $\Pi = \{\pi_1 = \{c_1, \gamma_1\}, ...\pi_{1750} = \{c_7, \gamma_{250}\}\}$. It was determined that $v_{max} = 251$, therefore $C = 3$ and $\gamma = 0.01$.

The average classification accuracies for the two-tone simulations are shown in Table 5.5. By examining P_5 and P_6, this Table indicates that all classifiers misclassified test vectors that have labels $\lambda_i = \Upsilon_5$ and $\lambda_i = \Upsilon_6$ (noise category). This is caused by the fact that the feature vectors with the label $\lambda_i = \Upsilon_5$ are extracted from power spectrums that have FOD and IMD near the noise floor, which is evident by the average SNR values $\text{ASNR}_{(1,5)}$ and $\text{ASNR}_{(2,5)}$ in Table 5.2. This is also evident by examining Figure 5.6(e), which is a power spectrum generated by Υ_5, in response to a two-tone signal, using $\sigma^2_{c_1}$. As illustrated in this Figure, the FOD is near the noise floor and the IMD is not detectable. Therefore, the feature vectors with label $\lambda_i = \Upsilon_5$ are being classified as category Υ_6 (noise) and the feature vectors with label $\lambda_i = \Upsilon_6$ are being classified as category Υ_5. In addition, the Bayesian$_\mu$ classifier has a large number of classification errors, which is indicated by examining P_6 in Table 5.5.

5.2.6 Conclusions

For the Two-Tone simulations, we presented a method to forensically characterize circuit models using features of the FOD and IMD that were generated in response to a two-tone signal. It was shown that classification errors occur for features sampled from power spectrums with low SNR. All classifiers, except the Bayesian$_\mu$, had high average classification accuracies, which is evident by examining Table 5.5.

5.3 Gaussian Chirp Signal Simulations

In this Section, we present a method to forensically characterize circuit models using harmonic distortion generated by nonlinearities in response to a Gaussian chirp signal. This method was discussed in Section 2.2 of Chapter 2. We will also present a method to forensically characterize circuit models using the filter response to a Gaussian chirp signal. This method was discussed in Section 2.2.1 of Chapter 2. We will implement two feature selection methods and compare the classification results. Both feature selection techniques were discussed in Section 3.2 of Chapter 3. The first feature selection technique samples the power spectrum of the return signal at regular intervals within a set band of frequencies. The second feature selection method samples the power spectrum of the return signal at precise locations. For each feature selection method, five circuit models are used, where one of the circuit models is a noise only model. We will use five noise power spectrums, $\{\sigma_{c_1}^2, \sigma_{c_2}^2, \sigma_{c_3}^2, \sigma_{c_4}^2, \sigma_{c_5}^2\}$, for each circuit model. A set of Gaussian chirp probe signals are input into the circuit models. A set of return signals are generated by each circuit model in response to the set of probe signals. Power spectrums of the return signals are obtained and features are extracted based on one of the two feature selection techniques. The features are classified and the results are compared.

5.3.1 Probe Signal Design

A set of Gaussian chirp signals will be used as input to the five circuit models. The set of signals are $P = \{p_1(t), ...p_L(t)\}$, where

$$p_l(t) = p(t) = C_1 e^{i(2\pi f_0 t + \pi k t^2)} e^{\frac{-(t-\mu)^2}{2\sigma^2}} \tag{5.29}$$

where each parameter is described in Table 5.6 and $L = 500$. An example of $p(t)$ is shown in Figure 5.7. The bandwidth of $p(t)$ was defined in Section 1.4 of Chapter 1 as [38]

$$B^2 = \frac{1}{E} \int_{-\infty}^{\infty} (2\pi f)^2 |P(f)|^2 df \tag{5.30}$$

where $|P(f)|$ is the magnitude of the Fourier transform of $p(t)$, and E is the energy of $p(t)$ defined by [9]

$$E = \int_{-\infty}^{\infty} |p(t)|^2 dt \tag{5.31}$$

The bandwidth of $p(t)$ is $B = 3.82$GHz.

As discussed in Section 2.2 of Chapter 2, harmonic distortion occurs in the return signal. It is possible that an overlap of the harmonic distortion components will occur in the frequency domain. The concept of the overlapping components in the frequency domain of the return signal was discussed in Section 2.2 of Chapter 2. The overlap is measured by

$$\epsilon = \frac{(\sigma_\xi(j) + \sigma_\xi(l))^2}{(\mu_\xi(l) - \mu_\xi(j))^2} \tag{5.32}$$

where

$$\mu_\xi(j) = j[f_0 + \mu k] \tag{5.33}$$

where j denotes the j^{th} order harmonic, and

Table 5.6
Gaussian Chirp Signal Parameters.

Parameters	Description	Definition
C_1	Amplitude of signal	1
i	Imaginary number	$\sqrt{-1}$
f_0	Frequency at $t = 0$	1Hz
f_1	Frequency at t_1	2GHz
t_1	Final time	50μs
t	Time	$0 \leq t \leq 50\mu$s
k	Chirp rate	$4x10^{13}$
μ	Mean	$1.5x10^{-5}$
σ	Standard deviation	$3.5x10^{-6}$

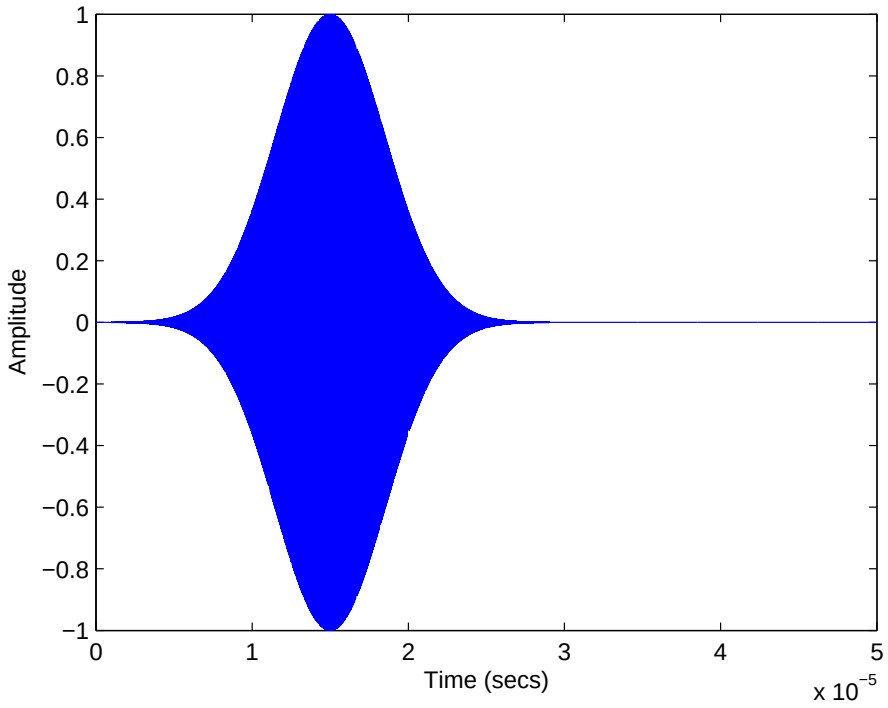

Fig. 5.7. Example of the Gaussian Chirp Probe Signal. Parameters of the Probe Signal are Defined in Table 5.6.

$$\sigma_{\xi}^{2}(j) = \frac{j\gamma^{2}}{8\pi^{2}\sigma^{2}} \tag{5.34}$$

and

$$\gamma = \sqrt{1 + 4\pi^{2}\sigma^{4}k^{2}} \tag{5.35}$$

It was also shown in Section 2.2 of Chapter 2 that $\mu_{\xi}(l) > \mu_{\xi}(j)$, $\sigma_{\xi}(j) > 0$, and $\sigma_{\xi}(l) > 0$. Note that l can replace j in Equations 5.33 and 5.34.

Two values of ϵ are determined, where the first is for the overlap between the first and second order harmonics. The second value of ϵ is for the overlap between the second and third order harmonics. Before finding ϵ, we will determine $\mu_{\xi}(j)$ and $\sigma_{\xi}^{2}(j)$ for $j = 1$, $j = 2$, and $j = 3$. Using Equations 5.33 and 5.34, it can be shown that $\mu_{\xi}(1) \approx 600x10^{6}$, $\mu_{\xi}(2) \approx 1200x10^{6}$, $\mu_{\xi}(3) \approx 1800x10^{6}$, $\sigma_{\xi}(1) \approx 99x10^{6}$, $\sigma_{\xi}(1) \approx 140x10^{6}$, and $\sigma_{\xi}(1) \approx 171x10^{6}$. Substituting these values into Equation 5.32 for $j = 1$ and $l = 2$ yields $\epsilon_{12} = 0.159$, which is the overlap between the first and second order harmonics. Substituting these values into Equation 5.32 for $j = 2$ and $l = 3$ yields $\epsilon_{23} = 0.269$, which is the overlap between the second and third order harmonics. Note that $\epsilon_{23} > \epsilon_{12}$, indicates that more overlap occurs for the second and third order harmonics. We assume that the overlap, determined by ϵ_{12} and ϵ_{23}, is small enough for accurate device characterization.

5.3.2 Circuit Model Design

$D = 5$ circuit models are considered in these simulations and are referred to as $\Upsilon = \{\Upsilon_1, ...\Upsilon_D\}$. Υ_d is known as the d^{th} circuit model, where $d \in \{1, ...D\}$. Circuit model Υ_5 is the noise only model. The circuit models $\{\Upsilon_1, ...\Upsilon_4\}$ have a distinct nonlinearity of order $M = 3$. The circuit models for Υ_1 and Υ_3 use filters and the circuit models for Υ_2 and Υ_4 do not use filters. As discussed in Section 2.2.1 of Chapter 2, the Gaussian chirp signal can be designed to estimate the filter response of the circuits with filters if the filter response is known a priori. This requires that the

Table 5.7
Circuit Model Parameters Used in the Gaussian Chirp Simulations.

	Υ_1	Υ_2	Υ_3	Υ_4
a_1	0.01	0.001	0.003	0.007
a_2	0.008	0.0009	0.001	0.0009
a_3	0.009	0.00007	0.0007	0.00007
Filter Passband (MHz)	400-450	N/A	670-710	N/A
Filter Order	2	N/A	4	N/A

passband of the filters in Υ_1 and Υ_3 are within the frequency band (i.e., f_0 to f_1) of the Gaussian chirp signal. As will be shown, the passband of both filters in Υ_1 and Υ_3 are within the frequency band of the Gaussian chirp signal and can therefore be estimated. Figure 5.8 shows an example of a power spectrum of a return signal generated by each circuit model in response to the probe signal defined in Equation 5.29, where the noise power spectrum is $\sigma_c^2 = 5x10^{-9}$. As shown in Figures 5.8(a) and 5.8(c), the Gaussian chirp signal is used to estimate the filter response. In addition, the Gaussian chirp signal is used to produce harmonic distortion as shown in Figures 5.8(b) and 5.8(d).

The nonlinearities and filter parameters for the circuit models are shown in Table 5.7. The nonlinearities are chosen such that the passband of the filters in Υ_1 generates, in response to the Gaussian chirp signal, a filter response with higher energy than that of Υ_3. Also, the nonlinearities are chosen such that Υ_2 generates, in response to the Gaussian chirp signal, harmonic distortions with higher energy compared with that of Υ_4, where the harmonic distortion for Υ_4 is near the noise floor.

As mentioned at the beginning of this Section, multiple noise power spectrums are used in each circuit model. We will consider the following noise power spectrums: $\sigma_C = \{\sigma_{c_1}^2 = 5x10^{-10}, \sigma_{c_2}^2 = 5x10^{-9}, \sigma_{c_3}^2 = 1x10^{-8}, \sigma_{c_4}^2 = 5x10^{-8}, \sigma_{c_5}^2 = 5x10^{-7}\}$. The

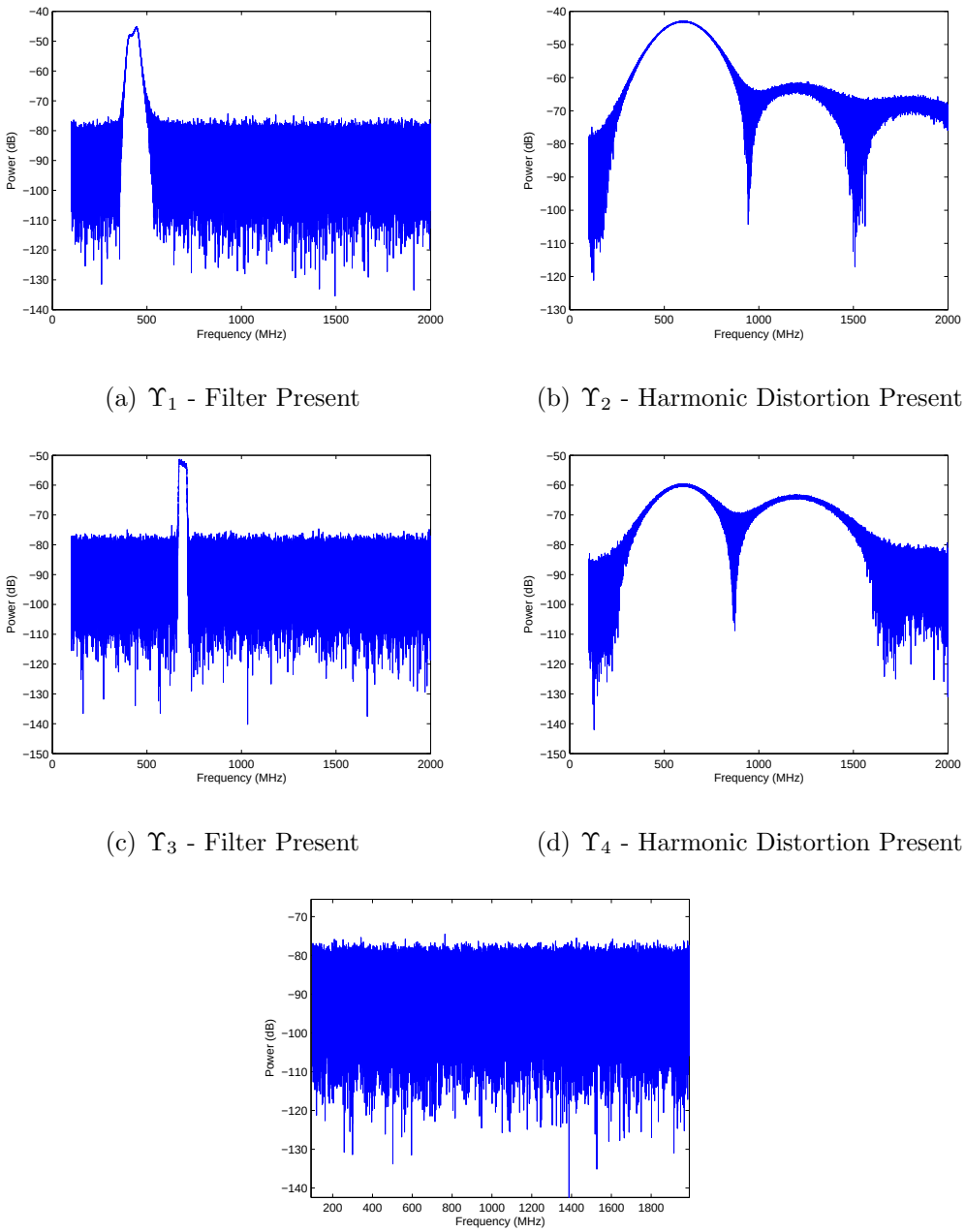

(a) Υ_1 - Filter Present

(b) Υ_2 - Harmonic Distortion Present

(c) Υ_3 - Filter Present

(d) Υ_4 - Harmonic Distortion Present

(e) Υ_5 - Noise

Fig. 5.8. Example Power Spectrums of the Return Signal From Each Circuit Model.

notation $\sigma_{c_n} \in \sigma_C$ is used to denote the n^{th} noise power spectrum, where $n \in \{1, ...N\}$ and $N = 5$.

5.3.3 Generation of the Return Signals

The circuit models are used to generate simulated data in response to the set of Gaussian chirp signals in P. Each circuit model, using a particular noise power spectrum, outputs L return signals, where $L = 500$. Each return signal will have a label (ground truth) associated with it, which is used to denote the circuit model that generated the return signal. Each return signal and label pair are known as an observation. Circuit model Υ_d, using the noise power spectrum σ_{c_n}, generates the follow set of observations in response to the set P:

$$O_{(n,d)} = \{[r_{(n,d,1)}(t), \gamma_{(n,d,1)} = d], ...[r_{(n,d,L)}(t), \gamma_{(n,d,L)} = d]\} \tag{5.36}$$

where the notation d signifies the circuit model Υ_d and n signifies the noise power spectrum $\sigma^2_{c_n}$, $\gamma_{(n,d,l)}$ is the ground truth label, and $r_{(n,d,l)}(t)$ is the return signal generated in response to the probe $p_l(t)$. The set of observations produced by all circuit models and all noise power spectrums is

$$O = \{O_{(1,1)}, ...O_{(1,5)}, O_{(2,1)}, ...O_{(2,5)}, ..., ...O_{(5,1)}, ...O_{(5,5)}\} \tag{5.37}$$

Note that the total number of return signals is 12,500. The power spectrums are obtained for all return signals in the set O from Equation 5.37. The power spectrums of the return signals in the set $O_{(n,d)}$ are

$$P_{O_{(n,d)}} = \{[P_{r_{(n,d,1)}}(f), \gamma_{(n,d,1)} = d], ...[P_{r_{(n,d,L)}}(f), \gamma_{(n,d,L)} = d]\} \tag{5.38}$$

where

$$P_{r_{(n,d,l)}}(f) = R_{(n,d,l)}(f)[R_{(n,d,l)}(f)]^* \tag{5.39}$$

and

$$R_{(n,d,l)}(f) = \int_{-\infty}^{\infty} r_{(n,d,l)}(t) e^{-i2\pi ft} dt \tag{5.40}$$

Table 5.8
Average SNR for Each Circuit Model and Each Noise Power. SNR is Defined in dB.

	Υ_1	Υ_2	Υ_3	Υ_4
$\sigma^2_{c_1}$	28.1	37.9	20.6	22.9
$\sigma^2_{c_2}$	18.1	27.9	10.6	12.9
$\sigma^2_{c_3}$	15.04	24.9	7.54	9.9
$\sigma^2_{c_4}$	8.05	17.9	0.55	2.91
$\sigma^2_{c_5}$	-1.94	7.93	-9.45	-7.09

The power spectrums of the return signals form the set

$$P_O = \{P_{O_{(1,1)}}, ...P_{O_{(5,5)}}\} \tag{5.41}$$

We will next determine the average SNR for each set $P_{O_{(n,d)}}$ of power spectrums. First, by using Equation 5.4, we can define the SNR for the given power spectrum $P_{r_{(n,d,l)}}(f)$ as $SNR_{(n,d,l)}$, where $P_{r_{(n,d,l)}}(f) \in P_{O_{(n,d)}}$. Then, we will define the average SNR for the power spectrums in $P_{O_{(n,d)}}$ as

$$\text{ASNR}_{(n,d)} = \frac{\sum_{l=1}^{L} \text{SNR}_{(n,d,l)}}{L} \tag{5.42}$$

where $d \neq 5$ in Equation 5.42 since the SNR is not determined for the noise model. The average SNR is shown in Table 5.8. Note that the average SNR for row $\sigma^2_{c_5}$ and columns Υ_1, Υ_3, and Υ_4 are low relative to the other average SNR values.

5.3.4 Features Selected at Regular Intervals

Features are extracted from each power spectrum in P_O of Equation 5.41. The methods used for feature extraction were discussed in Section 3.2 of Chapter 3. As discussed, amplitudes (features) were sampled from a power spectrum and formed

into a feature vector. The locations of the samples are determined based on one of two methods: features selected at regular intervals and features selected at precise locations. Each method will be implemented separately and will constitute a different simulation. The process of selecting features at regular interval is discussed in this Section.

When features are selected at regular intervals, $G = 34$ features are used. The frequency range sampled is 200MHz - 1900MHz in increments of Δ_G, where $\Delta_G =$ 50MHz. This frequency range is chosen so that the first, second, and third order harmonic distortions are sampled. As discussed in Section 3.2 of Chapter 3, the set of frequencies corresponding to the features are $\rho_g = \rho_{g-1} + \Delta$, for $2 \leq g \leq G$. Δ is a constant offset value and $\rho_1 = 200$MHz. The amplitude is sampled at:

$$e_{(k,g)} = P_{r_{(n,d,l)}}(\rho_g) \tag{5.43}$$

where, given any values of n, d, and l, $k = (n-1)DL+(d-1)L+l$, $k \in \{1, ...K\}$, and $K = 12,500$. The features form the feature vector

$$\boldsymbol{\eta}_k = [\mathbf{e}_{(k,1)} \ ... \ \mathbf{e}_{(k,G)}] \tag{5.44}$$

where $\boldsymbol{\eta}_k \in \Re^G$. Also, we let

$$\Gamma_k = \gamma_{(n,d,l)} \tag{5.45}$$

We can then order the feature vectors and labels as

$$\{[\boldsymbol{\eta}_1, \Gamma_1], ...[\boldsymbol{\eta}_K, \Gamma_K]\} \tag{5.46}$$

where $[\boldsymbol{\eta}_k, \Gamma_k]$ is known as the k^{th} observation (ground truth). Each observation in Equation 5.46 is randomly divided into the training and testing sets. The concept training and testing sets were introduced in Chapter 4. Before dividing the observations in Equation 5.46, first let $\nu(k)$ be a random variable with a uniform

distribution on the interval [0 1] indexed by the integer k [4]. For the k^{th} observation in Equation 5.46, we let

$$\begin{aligned} \{\boldsymbol{\theta}_j = \boldsymbol{\eta}_k,\, \tau_j = \Gamma_k\} \quad &, \quad \nu(k) \geq 0.5 \\ \{\boldsymbol{\omega}_i = \boldsymbol{\eta}_k,\, \lambda_i = \Gamma_k\} \quad &, \quad \nu(k) < 0.5 \end{aligned} \tag{5.47}$$

where $\boldsymbol{\theta}_j$ is the j^{th} training vector with a label τ_j, and $\boldsymbol{\omega}_i$ is the i^{th} test vector with a label λ_i. The training vectors form the set

$$\boldsymbol{\Theta} = \{[\boldsymbol{\theta}_1, \tau_1], ...[\boldsymbol{\theta}_{\mathbf{J}}, \tau_{\mathbf{J}}]\} \tag{5.48}$$

Note that since we are randomly dividing the observations in Equation 5.46, $\mathbf{J}$ is a discrete random variable where $\mathbf{J} \in \{0, 1, ...K\}$.

The test vectors form the set

$$\boldsymbol{\Omega} = \{[\boldsymbol{\omega}_1, \lambda_1], ...[\boldsymbol{\omega}_{\mathbf{I}}, \lambda_{\mathbf{I}}]\} \tag{5.49}$$

Also note $\mathbf{I}$ is a discrete random variable where $\mathbf{I} \in \{0, 1, ...K\}$ and $K = \mathbf{J} + \mathbf{I}$. We will introduce the notation $\Omega_{(n,d)}$, which signifies the set of test vectors with features extracted from the power spectrums in $P_{O_{(n,d)}}$. This notation is necessary when discussing the classification results presented in the next Section.

For the training set described by Equation 5.48, the number of total observations and the number observations per category are shown in Table 5.9, where $\mathbf{Q}_d \in \mathbf{J}$ was defined in Chapter 4 as the number of observations that have the label $\tau_j = d$. For the test set in Equation 5.49, the total number of observations and the number observations per category are shown in Table 5.10, where $\mathbf{R}_d \in \mathbf{I}$ was defined in Chapter 4 as the number of observations that have the label $\lambda_i = d$.

[4]These simulations used the *MATLAB* function *rand()* to generate a pseudorandom number drawn from the uniform distribution.

Table 5.9
Number of Feature Vectors Per Category for the Training Set. Features are Sampled at Regular Intervals.

J	$\mathbf{Q}_1$	$\mathbf{Q}_2$	$\mathbf{Q}_3$	$\mathbf{Q}_4$	$\mathbf{Q}_5$
6243	1261	1217	1294	1249	1222

Table 5.10
Number of Feature Vectors Per Category for the Testing Set. Features are Sampled at Regular Intervals.

I	$\mathbf{R}_1$	$\mathbf{R}_2$	$\mathbf{R}_3$	$\mathbf{R}_4$	$\mathbf{R}_5$
6257	1239	1283	1206	1251	1278

Simulation Results

We will measure the average classification accuracy for each circuit model in Υ. As discussed in Chapter 4, this accuracy is

$$P_d = \frac{\sum_{\substack{i=1 \\ \lambda_i = d}}^{I} I_f(i)}{R_d} \tag{5.50}$$

where

$$I_f(i) = \begin{cases} 1 & , \quad \lambda_i = \chi_i \\ 0 & , \quad \text{else} \end{cases} \tag{5.51}$$

is the indicator function and χ_i is the predicted label decided by the classifier. The K nearest neighbor (K-NN) classifier, Parzen window (PW) classifier, and support vector machine (SVM) require parameters prior to classification. As discussed in Section 5.2.5, we will define a set of parameters $\Pi = \{\pi_1, ...\pi_V\}$ for each classifier to determine the highest classification accuracy. The K-NN classifier requires the number of nearest neighbors, K_J, prior to classification. Let the parameter set for the K-NN classifier be $\Pi = \{\pi_1 = 1, ...\pi_4 = 4\}$, where the parameters correspond to the number of nearest neighbors used by the classifier. This set of nearest neighbors was chosen initially to determine the accuracy of the K-NN. As will be shown, the classification accuracies for this set of parameters is high, therefore no other parameters are tested. It was determined that $v_{max} = 3$, therefore $K_J = \pi_3 = 3$. The PW classifier requires the window width, h, prior to classification. Define the parameter set for the PW classifier as $\Pi = \{\pi_1 = 0.1, \pi_2 = 0.3, ...\pi_{25} = 4.9\}$, where these parameters correspond to the window width used by the classifier. It was determined that $v_{max} = 10$, therefore $h = \pi_{10} = 2.9$. The SVM classifier requires two inputs C and γ prior to classification. Note that $C \in \{c_1 = 1, c_2 = 3, ...c_{10} = 19\}$ and $\gamma \in \{\gamma_1 = 0.01, \gamma_2 = 0.03, ...\gamma_{100} = 1.99\}$. Let the parameter set for the SVM classifier be $\Pi = \{\pi_1 = \{c_1, \gamma_1\}, ...\pi_{1000} = \{c_{10}, \gamma_{100}\}\}$. It was determined that $v_{max} = 201$, therefore $C = 5$ and $\gamma = 0.01$.

Table 5.11
Average Classification Accuracies for the Gaussian Chirp Simulations Using Features Sampled at Regular Intervals.

	P_1	P_2	P_3	P_4	P_5
SVM	100%	99.9%	100%	99.9%	100%
BTC	99.9%	100%	99.8%	100%	99.7%
Bayesian$_\mu$	79.5%	100%	79.5%	78.4%	79.3%
Bayesian$_\Sigma$	100%	100%	99.9%	87.1%	100%
PW	100%	100%	100%	100%	100%
K-NN	100%	100%	100%	100%	100%

The average classification accuracy of each classifier for each circuit model is shown in Table 5.11. Recall that $\Omega_{(n,d)}$ denotes the set of test vectors with features that are extracted from the power spectrums in $P_{O_{(n,d)}}$. All classifiers produce high classification accuracies except for the Bayesian$_\mu$ classifier and the Bayesian$_\Sigma$ classifier. Classification errors occur for the Bayesian$_\mu$ classifier using test vectors in $\Omega_{(n=5,1)}$, $\Omega_{(n=5,3)}$, $\Omega_{(n=5,4)}$, and $\Omega_{(n=5,5)}$. Note that $n = 5$, signifies the noise power spectrum $\sigma^2_{c_5}$. The reason for these classification errors is due to the increase in noise power, which is evident by the average SNR values for $\sigma^2_{c_5}$ of Table 5.8. To better clarify these classification errors, consider the power spectrums in Figure 5.9. These power spectrums are examples generated by the circuit models in response to the Gaussian chirp signal using the noise power spectrum $\sigma^2_{c_5}$. As indicated in the Figures, all power spectrums are noisy, which is the cause of the classification errors.

Classification errors also occur for the Bayesian$_\Sigma$ classifier for test vectors in $\Omega_{(5,4)}$. The reason for these errors is due to the increase in noise power, which is evident by the average SNR value for row $\sigma^2_{c_5}$ and column Υ_4 of Table 5.8. This is also evident in Figure 5.9(c), which is a power spectrum from $P_{O_{(5,4)}}$. As shown in this Figure, the harmonic distortion is near the noise floor, therefore the test vectors in $\Omega_{(5,4)}$ are being classified as noise.

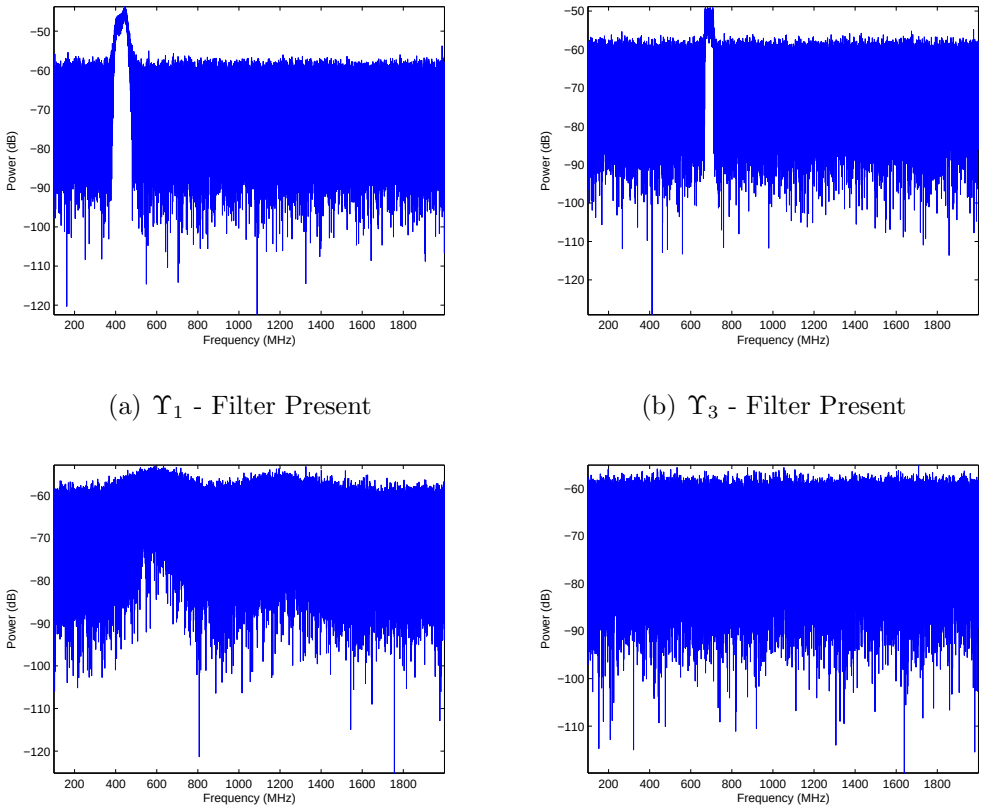

(a) Υ_1 - Filter Present

(b) Υ_3 - Filter Present

(c) Υ_4 - Harmonic Distortion Present

(d) Υ_5 - Noise

Fig. 5.9. Example of Power Spectrums Generated by Circuit Models Υ_1, Υ_3, Υ_4, and Υ_5 in Response to a Gaussian Chirp Signal Using the Noise Power Spectrum $\sigma^2_{c_5}$.

5.3.5 Features Selected at Precise Locations

In this Section, features are selected at precise locations as described in Section 3.2 of Chapter 3. This feature selection technique uses the a priori information of the harmonic distortion and filter response to sample the highest amplitudes available in a given power spectrum. This is done since the highest amplitudes are most resilient to noise. For the given set of power spectrums in Equation 5.41, we will sample the locations of the estimated filter responses generated by Υ_1 and Υ_3 in response to the Gaussian chirp signal. We will also sample the peak locations of the

harmonic distortion that is generated by Υ_2 and Υ_4 in response to the Gaussian chirp signal. The features are selected as follows. First, examine the filter response of Υ_1 in Figure 5.10. We will sample three frequencies in the passband of this filter. As is illustrated, the frequencies $\rho_1 = 410$MHz, $\rho_2 = 430$MHz, and $\rho_3 = 445$MHz are sampled. Next, consider the first harmonic in the power spectrum generated by Υ_2 as is shown in Figure 5.11. This Figure illustrates that the power spectrum is sampled at the three frequencies corresponding to the peak of the first harmonic. These frequency locations are $\rho_4 = 598$MHz, $\rho_5 = 600$MHz, and $\rho_6 = 602$MHz. The filter response of Υ_3 is sampled using the same procedure as described for Υ_1. As shown in Figure 5.12, the filter response of Υ_3 is sampled at the frequencies $\rho_7 = 682$MHz, $\rho_8 = 690$MHz, and $\rho_9 = 698$MHz. Finally, a close examination of the second and third harmonics in Figure 5.11 illustrates that amplitudes are selected as frequencies $\rho_{10} = 1198$MHz, $\rho_{11} = 1200$MHz, $\rho_{12} = 1202$MHz, $\rho_{13} = 1798$MHz, $\rho_{14} = 1800$MHz, and $\rho_{15} = 1802$MHz. The set of frequencies form the set $\rho = \{\rho_1, ...\rho_{15}\}$.

As discussed in Section 3.2 of Chapter 3, the set of frequencies are $\rho = \{\rho_1, ...\rho_G\}$. Let ρ_g denote the g^{th} frequency, where $g \in \{1, ...G\}$. The amplitude at each frequency in ρ is determined by

$$e_{(k,g)} = P_{r_{(n,d,l)}}(\rho_g) \tag{5.52}$$

where, given any values of n, d, and l, $k = (n-1)DL + (d-1)L + l$, $k \in \{1, ...K\}$, $K = 12500$. The features form the feature vector

$$\boldsymbol{\eta}_k = [\mathbf{e}_{(k,1)} \ ... \ \mathbf{e}_{(k,G)}] \tag{5.53}$$

where $\boldsymbol{\eta}_k \in \Re^G$. We can then order the feature vectors and labels as

$$\{[\boldsymbol{\eta}_1, \Gamma_1], ...[\boldsymbol{\eta}_K, \Gamma_K]\} \tag{5.54}$$

where Γ_k was defined by Equation 5.45. The training and testing sets are then determined using the exact same procedure as described in Section 5.3.4 for features

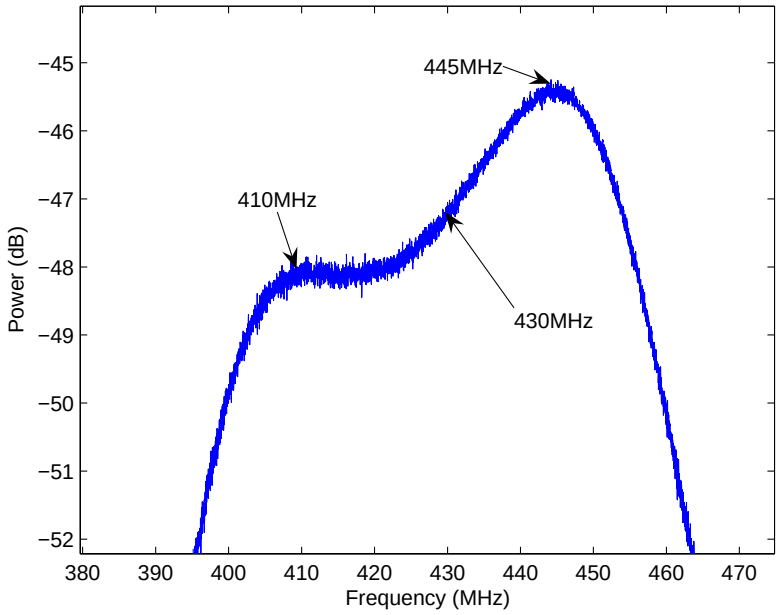

Fig. 5.10. Estimated Filter Response of the Power Spectrum of by Υ_1 in response to a Gaussian Chirp Signal. Features are Precisely Chosen in the Passband of the Filter Response.

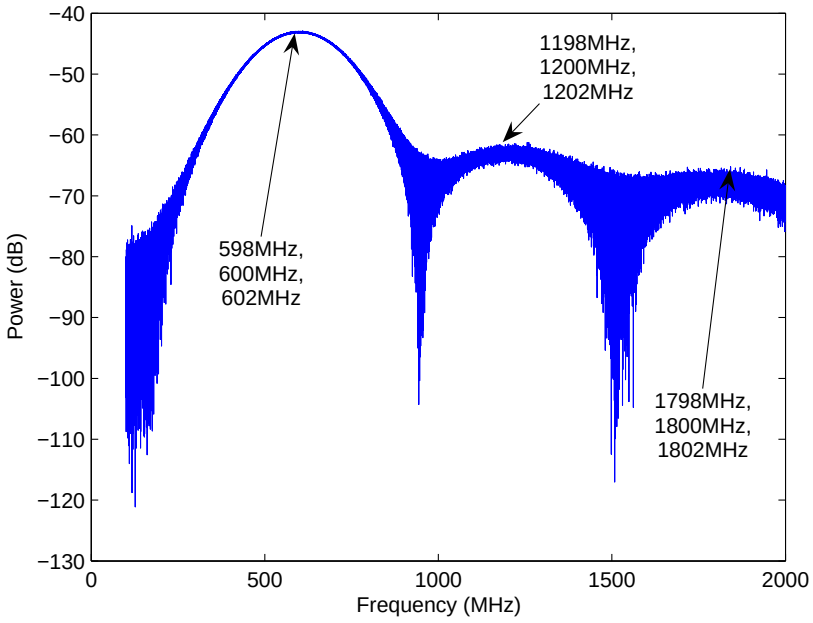

Fig. 5.11. Gaussian Harmonic Distortion of Υ_2 in response to a Gaussian Chirp Signal. Features are Precisely Chosen at Peaks of Each Harmonic.

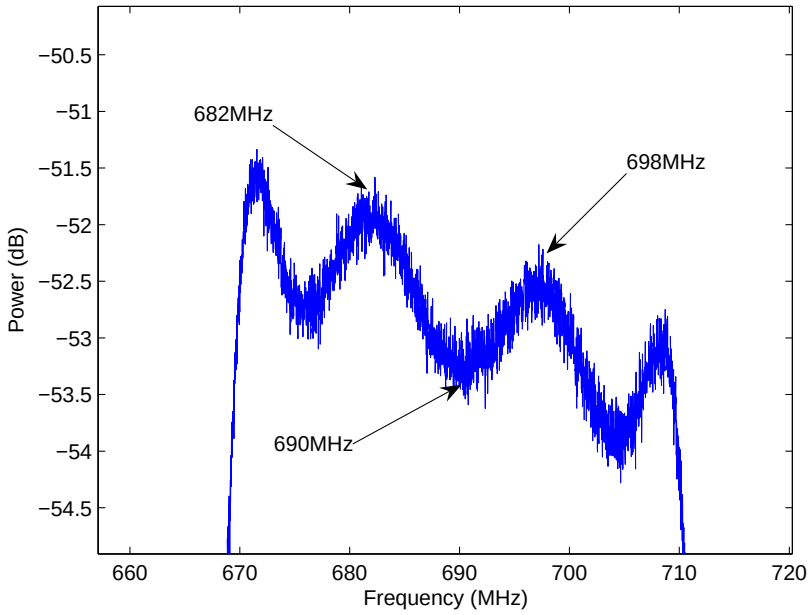

Fig. 5.12. Estimated Filter Response of a Power Spectrum of Υ_3 in response to a Gaussian Chirp Signal. Features are Precisely Chosen in the Passband of the Filter Response.

Table 5.12
Number of Feature Vectors Per Category for the Training Set. Features are Sampled at Precise Locations.

$\mathbf{J}$	$\mathbf{Q}_1$	$\mathbf{Q}_2$	$\mathbf{Q}_3$	$\mathbf{Q}_4$	$\mathbf{Q}_5$
6279	1264	1241	1249	1276	1249

Table 5.13
Number of Feature Vectors Per Category for the Testing Set. Features are Sampled at Precise Locations.

$\mathbf{I}$	$\mathbf{R}_1$	$\mathbf{R}_2$	$\mathbf{R}_3$	$\mathbf{R}_4$	$\mathbf{R}_5$
6221	1236	1259	1251	1224	1251

selected at regular intervals. For the simulation discussed in this Section, the training vectors form the set

$$\mathbf{\Theta} = \{[\boldsymbol{\theta}_1, \tau_1], ...[\boldsymbol{\theta}_\mathbf{J}, \tau_\mathbf{J}]\} \tag{5.55}$$

and the testing vectors form the set

$$\mathbf{\Omega} = \{[\boldsymbol{\omega}_1, \lambda_1], ...[\boldsymbol{\omega}_\mathbf{I}, \lambda_\mathbf{I}]\} \tag{5.56}$$

For the training set defined by Equation 5.55, the number of total observations and the number observations per category are shown in Table 5.12. For the testing set in Equation 5.56, the total number of observations and the number observations per category are shown in Table 5.13.

Classification Results

An average classification accuracy is measured for each category and each classifier using the same procedure discussed in Section 5.3.4. Once again, several parameters must be tested for the K-NN classifier, PW classifier, and SVM classifier priori to

classification. The K-NN classifier requires the number of nearest neighbors, K_J, prior to classification. Let the parameter set for the K-NN classifier be $\Pi = \{\pi_1 = 1, ...\pi_4 = 4\}$, where the parameters correspond to the number of nearest neighbors used by the classifier. This set of nearest neighbors was chosen initially to determine the accuracy of the K-NN. As will be shown, the classification accuracies for this set of parameters is high, therefore no other parameters are tested. It was determined that $v_{max} = 1$, therefore $K_J = \pi_1 = 1$. The PW classifier requires the window width, h, prior to classification. Define the parameter set for the PW classifier as $\Pi = \{\pi_1 = 0.1, \pi_2 = 0.3, ...\pi_{25} = 4.9\}$, where these parameters correspond to the window width used by the classifier. It was determined that $v_{max} = 10$, therefore $h = \pi_{10} = 2.9$, which is the same window width used above for features selected at regular intervals described in Section 5.3.4. The SVM classifier requires two inputs C and γ prior to classification. Note that $C \in \{c_1 = 1, c_2 = 3, ...c_{10} = 19\}$ and $\gamma \in \{\gamma_1 = 0.01, \gamma_2 = 0.03, ...\gamma_{100} = 1.99\}$. Let the parameter set for the SVM classifier be $\Pi = \{\pi_1 = \{c_1, \gamma_1\}, ...\pi_{1000} = \{c_{10}, \gamma_{100}\}\}$. It was determined that $v_{max} = 1$, therefore $C = 1$ and $\gamma = 0.01$.

The average classification accuracy of each classifier for each circuit model is shown in Table 5.14. The results are very similar to the results for features selected at regular intervals, as described in Section 5.3.4. The classifications errors for the Bayesian$_\mu$ and Bayesian$_\Sigma$ classifiers in Table 5.14 are caused by the increase in noise, as discussed in Section 5.3.4. However, an average classification accuracy increase is indicated by P_4 in Table 5.14 for both the Bayesian$_\mu$ and Bayesian$_\Sigma$ classifiers. The average classification accuracy for the Bayesian$_\mu$ classifier increased from 78.4% to 100%. The average classification accuracy for the Bayesian$_\Sigma$ classifier increased from 87.1% to 92.6%. These results demonstrate that the sampling technique effects the classification accuracy and that features sampled at precise locations increases the classification accuracy.

Table 5.14
Average Classification Accuracies for the Gaussian Chirp Simulations Using Features Sampled at Precise Locations.

	P_1	P_2	P_3	P_4	P_5
SVM	100%	100%	100%	100%	100%
BTC	100%	99.4%	100%	99.5%	99.6%
Bayesian$_\mu$	79.4%	100%	79.5%	100%	79.9%
Bayesian$_\Sigma$	100%	100%	100%	92.6%	100%
PW	100%	100%	100%	100%	100%
K-NN	100%	100%	100%	100%	100%

5.3.6 Conclusions

For the Gaussian chirp simulations, we presented a method to forensically characterize circuit models using features of the harmonic distortion and features of an estimated filter response. It was shown that classification errors occur for features sampled from a power spectrum with low SNR. In addition, we demonstrated that features sampled at precise locations increased the average classification accuracy. The SVM, BT, PW, and K-NN classifiers had near perfect classification accuracies.

5.4 Linear Chirp Probe Signal Simulations and Experiments

In this Section, we present a method to forensically characterize actual RF circuits and circuit models using the filter response of two Chebyshev filters. The filter response is estimated using a linear chirp signal. In Section 5.4.1, two actual RF circuits are considered. A set of linear chirp probe signals are input into the two RF circuits and return signals are measured. Once power spectrums of the return signals are obtained, features are extracted and then classified. In Section 5.4.2, two circuit models are considered to simulate the experiment in Section 5.4.1. For both

the experiment and simulation, we will characterize the circuits (real and simulated) by the estimated filter response.

5.4.1 Linear Chirp Experiments

Two RF circuits are used in the experiments presented in this Section. The RF circuits are known as $\Upsilon = \{\Upsilon_1, \Upsilon_2\}$. A block diagram of these RF circuits are shown in Figure 5.13. The input probe signal $p(t)$ is a linear chirp signal (not windowed) and $r(t)$ is the return signal. Each circuit has a bandpass filter and an amplifier. The same amplifier is used in both RF circuits, however, the filters are different. For both RF circuits, the probe signal is filtered and sent to the amplifier. The amplifier reflects the incident signal, where the reflected signal is passed back through filter and is measured.

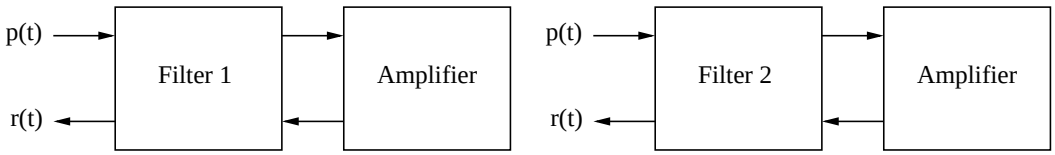

(a) Υ_1 (b) Υ_2

Fig. 5.13. Block Diagram of the Two RF Circuits Used in the Linear Chirp Experiments.

Three circuit components are considered for the RF circuits shown in Figure 5.13. These components are a Trilithic 4BC500/20-3-KK bandpass filter, a K&L Microwave 5MC10-500/T25-O/O bandpass filter, and a Hittite HMC479ST89 MMIC amplifier. The Trilithic 4BC500/20-3-KK bandpass filter is a 4^{th} order Chebyshev bandpass filter with a center frequency of 500MHz, a passband of 20MHz, and a passband ripple of 0.05dB and is labelled as Filter 1 in the block diagram of Figure 5.13. The K&L Microwave 5MC10-500/T25-O/O bandpass filter is a 5^{th} order Chebyshev filter

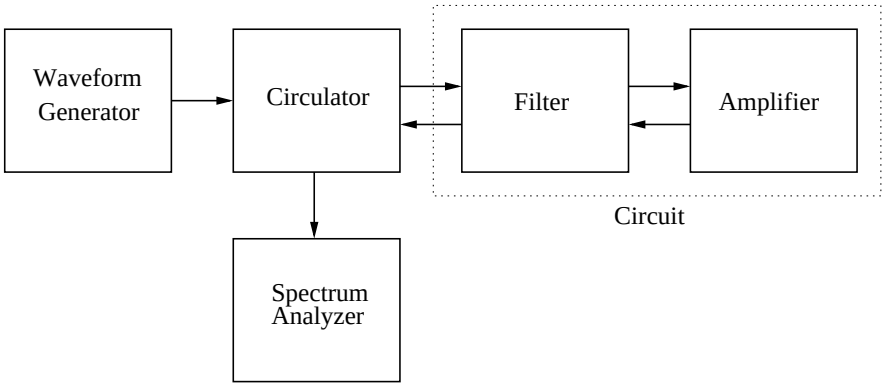

Fig. 5.14. RF Circuit Measurement System Used in the Linear Chirp Experiments.

with a center frequency of 500MHz, a passband of 25MHz, and a passband ripple of 0.05dB and is labelled as Filter 2 in the block diagram of Figure 5.13.

The return signal $r(t)$ in Figure 5.13 is measured using the system illustrated in Figure 5.14 [5]. This system uses a waveform generater to produce a linear chirp signal. The RF circuit is connected to the waveform generater by a circulator. Note that the probe signal is not transmitted through the environment to the circuit. The circulator is used to connect the probe signal to the RF circuit and connect the return signal to a spectrum analyzer. The spectrum analyzer measures the response from the RF circuit.

Probe Signal Design

The probe signal used by the waveform generator of Figure 5.14 is a combination of multiple signals

$$p(t) = \begin{cases} 0 & , \quad 0 \leq t < 50ns \\ A\cos(2\pi f_0 t) & , \quad 50ns \leq t < 550ns \\ Acos(2\pi(f_1 + \frac{(f_1 - f_0)}{2t_1}t)t) & , \quad 550ns \leq t < 1550ns \\ A\cos(2\pi f_0 t) & , \quad 1550ns \leq t < 2050ns \end{cases} \tag{5.57}$$

[5] All measurements were taken at North Carolina State University.

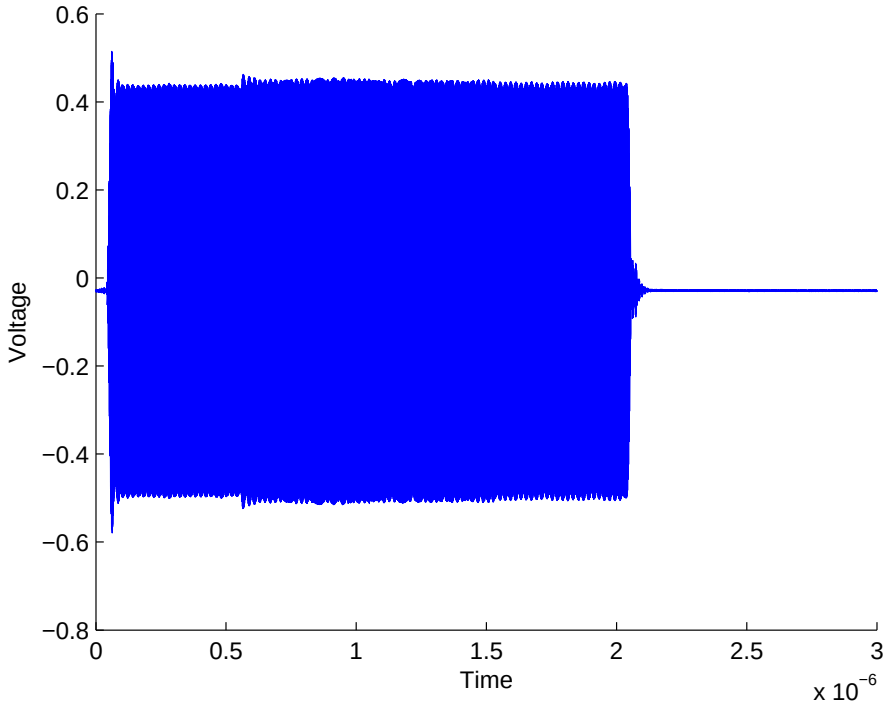

Fig. 5.15. Example of the Probe Signal Used in the Linear Chirp Experiments.

where A is the amplitude, $f_0 = 495$MHz, $f_1 = 505$MHz, and $t_1 = 1550$ nanoseconds (ns). The first signal is a cosine function and is used before the linear chirp signal to eliminate any transients. The cosine function is active for 500ns. At 550ns, the cosine function is deactivated and the linear chirp signal is activated. The linear chirp signal is designed to probe the frequency band 495MHz - 505MHz, which is within the passband of both filters. After 1000ns seconds, the linear chirp signal is deactivated and the cosine function is activated for 500ns. An example of this response is shown in Figure 5.15.

The waveform generator produces three sets of probe signals at different amplitudes A. The first set of probe signals is $P_1 = \{p_{(1,1)}(t), ...p_{(1,L)}(t)\}$, where $p_{(1,l)}(t) = p(t)$, A=0.316 volts, $l \in \{1, ...L\}$, and $L = 100$. The second set of probe signals is $P_2 = \{p_{(2,1)}(t), ...p_{(2,L)}(t)\}$, where $p_{(2,l)}(t) = p(t)$, and A=0.562 volts. The third set of probe signals is $P_3 = \{p_{(3,1)}(t), ...p_{(3,L)}(t)\}$, where $p_{(3,l)}(t) = p(t)$, and A=1.0 volts.

Generation of the Return Signals

The probe signals are input into each RF circuit and the responses are measured by the spectrum analyzer of Figure 5.14. The set of probe signals P_1 is input into both RF circuits. The set of probe signals P_2 is input into circuit Υ_1. The set of probe signals P_3 is input into circuit Υ_2. The return signal is $r_{(n,d,l)}(t)$, where $n \in \{1,2,3\}$ denotes the set P_n, $d \in \{1,2\}$ denotes the RF circuit Υ_d, and $l \in \{1,....L\}$ denotes the probe signal $p_l(t) \in P_n$. Each return signal will have a label (ground truth) associated with it, which is used to denote the RF circuit that generated the return signal. Each return signal and label pair are known as an observation. The set of observations [6] is

$$\{[r_{(n,d,1)}(t), \gamma_{(n,d,1)} = d], ...[r_{(n,d,L)}(t), \gamma_{(n,d,L)} = d]\} \tag{5.58}$$

where $\gamma_{(n,d,l)} = d$ is the ground truth label.

The linear chirp signal is used to estimate the filter response. The linear chirp signal is active in the probe $p(t)$ of Equation 5.57 between 550ns - 1550ns. We will therefore extract a section of the return signal $r_{(n,d,l)}(t)$ between 550ns - 1550ns, which is done to study the filter response. Let the offset time be $T = 550$ns. Each return signal $r_{(n,d,l)}(t)$ is redefined as

$$s_{(n,d,l)}(t) = \begin{cases} r_{(n,d,l)}(t+T) & , \quad 0ns \leq t \leq 1000ns \\ 0 & , \quad \text{else} \end{cases} \tag{5.59}$$

The observations from Equation 5.58 are then

$$O_{(n,d)} = \{[s_{(n,d,1)}(t), \gamma_{(n,d,1)} = d], ...[s_{(n,d,L)}(t), \gamma_{(n,d,L)} = d]\} \tag{5.60}$$

The set of observations produced by all RF circuits is

$$O = \{O_{(1,1)}, O_{(1,2)}, O_{(2,1)}, O_{(3,2)}\} \tag{5.61}$$

[6] This set of observations were measured at North Carolina State University.

Note that the subscript notation in Equation 5.61 is not ordered. The notation is only used to indicate the RF circuit Υ_d, and the set of probe signals P_n that are input into Υ_d. The total number of signals in Equation 5.61 is 400. The power spectrums of the signals in the set $O_{(n,d)}$ are

$$P_{O_{(n,d)}} = \{[P_{s_{(n,d,1)}}(f), \gamma_{(n,d,1)} = d], ...[P_{s_{(n,d,L)}}(f), \gamma_{(n,d,L)} = d]\} \tag{5.62}$$

where

$$P_{s_{(n,d,l)}}(f) = S_{(n,d,l)}(f)[S_{(n,d,l)}(f)]^* \tag{5.63}$$

and

$$S_{(n,d,l)}(f) = \int_{-\infty}^{\infty} s_{(n,d,l)}(t)e^{-i2\pi ft}dt \tag{5.64}$$

The power spectrums form the set

$$P_O = \{P_{O_{(1,1)}}, P_{O_{(1,2)}}, P_{O_{(2,1)}}, P_{O_{(3,2)}}\} \tag{5.65}$$

Features Selection

Features are extracted from each power spectrum in P_O of Equation 5.65. The method used for feature extraction was discussed in Section 3.3 of Chapter 3. As discussed, the set of frequencies corresponding to the features are $\rho_g = \rho_{g-1} + \Delta$, for $2 \leq g \leq G$. Δ is a constant offset value. Let $\rho_1 = 495$MHz, $G = 10$, and $\Delta = 1$MHz. Features are therefore selected between 495MHz-505MHz in increments of 1MHz. We will describe the feature extraction process for each set $P_{O_{(n,d)}}$ of power spectrums separately. The features extracted from the set of power spectrums $P_{O_{(1,1)}}$ are

$$\varrho_{(k,g)} = P_{s_{(1,1,l)}}(\rho_g) \tag{5.66}$$

where $k = l$, $k \in \{1, ...100\}$, and let the ground truth label be $\Gamma_k = \gamma_{(1,1,l)}$. The features extracted from the set of power spectrums $P_{O_{(1,2)}}$ are

$$\varrho_{(k,g)} = P_{s_{(1,2,l)}}(\rho_g) \tag{5.67}$$

where $k = 100 + l$, $k \in \{101, ...200\}$, and let $\Gamma_k = \gamma_{(1,2,l)}$. The features extracted from the set of power spectrums $P_{O_{(2,1)}}$ are

$$\varrho_{(k,g)} = P_{s_{(2,1,l)}}(\rho_g) \tag{5.68}$$

where $k = 200 + l$, $k \in \{201, ...300\}$, and let $\Gamma_k = \gamma_{(2,1,l)}$. The features extracted from the set of power spectrums $P_{O_{(3,2)}}$ are

$$\varrho_{(k,g)} = P_{s_{(3,2,l)}}(\rho_g) \tag{5.69}$$

where $k = 300 + l$, $k \in \{301, ...400\}$, and let $\Gamma_k = \gamma_{(3,2,l)}$. The features for a given k form the set $\varrho_k = \{\varrho_{(k,1)}, ...\varrho_{(k,G)}\}$. The samples are then normalized from 0 to 1. Scaling the features maintains the "pattern" of the passband ripple in the filter response. Each feature $\varrho_{(k,g)}$ is scaled as follows

$$e_{(k,g)} = \frac{\varrho_{(k,g)} - min(\varrho_k)}{max(\varrho_k) - min(\varrho_k)} \tag{5.70}$$

where the function $min(\varrho_k)$ is the minimum value of ϱ_k and the function $max(\varrho_k)$ is the maximum value of ϱ_k. The features form the feature vector

$$\boldsymbol{\eta}_k = [\mathbf{e}_{(k,1)} \ ... \ \mathbf{e}_{(k,G)}] \tag{5.71}$$

where $\boldsymbol{\eta}_k \in \Re^G$. We can then order the feature vectors and labels as

$$\{[\boldsymbol{\eta}_1, \Gamma_1], ...[\boldsymbol{\eta}_K, \Gamma_K]\} \tag{5.72}$$

where $[\boldsymbol{\eta}_k, \Gamma_k]$ is known as the k^{th} observation and K=400. Each observation in Equation 5.72 is randomly divided into the training and testing sets. The training and testing sets were introduced in Chapter 4. Before dividing the observations in

Equation 5.72, first let $\nu(k)$ be a uniform random variable on the interval [0 1] indexed by the integer k [7]. For the k^{th} observation in Equation 5.72, we let

$$\begin{aligned} \{\boldsymbol{\theta}_j = \boldsymbol{\eta}_k,\, \tau_j = \Gamma_k\} \quad &, \quad \nu(k) \geq 0.5 \\ \{\boldsymbol{\omega}_i = \boldsymbol{\eta}_k,\, \lambda_i = \Gamma_k\} \quad &, \quad \nu(k) < 0.5 \end{aligned} \tag{5.73}$$

where $\boldsymbol{\theta}_j$ is the j^{th} training vector with a label τ_j, and $\boldsymbol{\omega}_i$ is the i^{th} test vector with a label λ_i. The training vectors form the set

$$\boldsymbol{\Theta} = \{[\boldsymbol{\theta}_1, \tau_1], ...[\boldsymbol{\theta}_{\mathbf{J}}, \tau_{\mathbf{J}}]\} \tag{5.74}$$

Note that since we are randomly dividing the observations in Equation 5.72, $\mathbf{J}$ is a discrete random variable where $\mathbf{J} \in \{0, 1, ...K\}$. The test vectors form the set

$$\boldsymbol{\Omega} = \{[\boldsymbol{\omega}_1, \lambda_1], ...[\boldsymbol{\omega}_{\mathbf{I}}, \lambda_{\mathbf{I}}]\} \tag{5.75}$$

Also note that $\mathbf{I}$ is a discrete random variable where $\mathbf{I} \in \{0, 1, ...K\}$ and $K = \mathbf{J}+\mathbf{I}$.

For the training set described by Equation 5.74, the number of total observations and the number observations per category are shown in Table 5.15, where $\mathbf{Q}_d \in \mathbf{J}$ was defined in Chapter 4 as the number of observations that have the label $\tau_j = d$. For the test set in Equation 5.75, the total number of observations and the number observations per category are shown in Table 5.16, where $\mathbf{R}_d \in \mathbf{I}$ was described in Chapter 4 as the number of observations that have the label $\lambda_i = d$.

[7] These simulations used the *MATLAB* function *rand()* to generate a pseudorandom number drawn from the uniform distribution.

Table 5.15
Number of Feature Vectors Per Category for the Training Set. Features are Used in the Linear Chirp Experiments.

$\mathbf{J}$	$\mathbf{Q}_1$	$\mathbf{Q}_2$
211	103	108

Table 5.16
Number of Feature Vectors Per Category for the Testing Set. Features are Used in the Linear Chirp Experiments.

$\mathbf{I}$	$\mathbf{R}_1$	$\mathbf{R}_2$
189	97	92

Experimental Results

We will find the average classification accuracy for each RF circuit in Υ. As discussed in Chapter 4, this accuracy is

$$P_d = \frac{\sum_{\substack{i=1 \\ \lambda_i = d}}^{I} I_f(i)}{R_d} \tag{5.76}$$

where

$$I_f(i) = \begin{cases} 1 & , \quad \lambda_i = \chi_i \\ 0 & , \quad \text{else} \end{cases} \tag{5.77}$$

is the indicator function and χ_i is the predicted label decided by the classifier. The K nearest neighbor (K-NN) classifier, Parzen window (PW) classifier, and support vector machine (SVM) require input parameters priori to classification. As discussed in Section 5.2.5, we will define a set of parameters $\Pi = \{\pi_1, ...\pi_V\}$ for each classifier to determine the highest classification accuracy. The K-NN classifier requires the number of nearest neighbors, K_J, prior to classification. Let the parameter set for the K-NN classifier be $\Pi = \{\pi_1 = 1, ...\pi_{99} = 99\}$, where the parameters correspond to the number of nearest neighbors used by the classifier. It was determined that all parameters obtained perfect classification accuracy. We will therefore use $v_{max} = 1$ which yields $K_J = \pi_1 = 1$. The PW classifier requires the window width, h, prior to classification. Define the parameter set for the PW classifier as $\Pi = \{\pi_1 = 0.1, \pi_2 = 0.2, ...\pi_{50} = 5.0\}$, where these parameters correspond to the window width used by the classifier. It was determined that all parameters obtained perfect classification accuracy. We will therefore use $v_{max} = 1$ which yields $h = \pi_1 = 0.1$. The SVM classifier requires two inputs C and γ prior to classification. Note that $C \in \{c_1 = 1, c_2 = 2, ...c_{19} = 19\}$ and $\gamma \in \{\gamma_1 = 0.1, \gamma_2 = 0.2, ...\gamma_{19} = 1.9\}$. Let the parameter set for the SVM classifier be $\Pi = \{\pi_1 = \{c_1, \gamma_1\}, ...\pi_{361} = \{c_{19}, \gamma_{19}\}\}$. It was determined that all parameters obtained perfect classification accuracy. We will therefore use $v_{max} = 1$ which yields $C = 1$ and $\gamma = 0.1$.

Table 5.17
Classification Results for the Linear Chirp Experiment.

	P_1	P_2
SVM	100%	100%
BT	100%	98%
Bayesian$_\mu$	100%	100%
Bayesian$_\Sigma$	100%	100%
PW	100%	100%
K-NN	100%	100%

The average classification accuracy of each classifier for each RF circuit is shown in Table 5.17. All classifiers obtained near perfect classification accuracies. These results indicate that the ripple in the passband of the filter response is distinct. This fact is illustrated in Figure 5.16 where an example power spectrum is shown for Υ_1 and Υ_2. A distinct ripple pattern is present in the passband. The simulations presented in the next Section are used to verify these results.

5.4.2 Linear Chirp Simulations

Our goal is to use our simulation techniques to attempt to verify the experimental results we described above. For the simulations, two circuit models are considered. Each circuit model is shown in Figure 5.17. $p(t)$ is the input probe signal and $d(t)$ is the output from the second filter that is added to the noise $n_c(t)$. $r(t)$ is the return signal. The noise $n_c(t)$ is modeled as a white noise random process with a power spectrum, σ_c^2. The nonlinearity in both circuit models is modeled by a power series of order $M = 3$ as defined by Equation 5.1. The power series coefficients are adjusted to obtain a filter response at the same power level as the experiments as shown in Figure 5.16(a). The coefficients are defined as $a_1 = a_2 = a_3 = 0.6$. The filters in each circuit model, which are identical, are designed to simulate the filters of

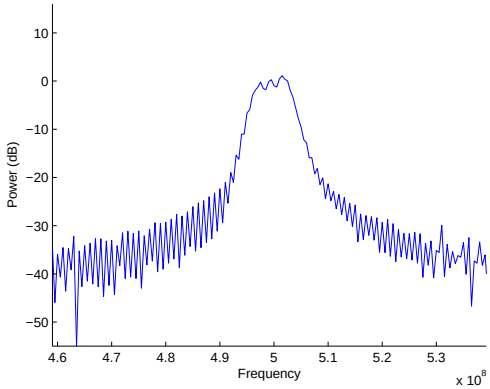

(a) Example Power Spectrum from Circuit Υ_1

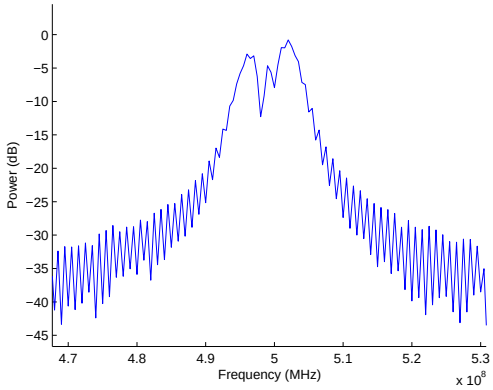

(b) Example Power Spectrum from Circuit Υ_2

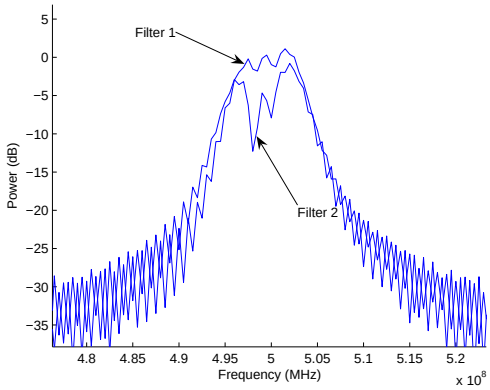

(c) Example Power Spectrum from Circuits Υ_1 and Υ_2

Fig. 5.16. Power Spectrums for the Linear Chirp Experiments. As is Illustrated, the Passband Ripple is Distinct.

the experiments. Therefore Υ_1 uses two 4^{th} order Chebyshev bandpass filters with a center frequency of 500MHz, a passband of 20MHz, and a passband ripple of 0.05dB. Υ_2 uses two 5^{th} order Chebyshev bandpass filters with a center frequency of 500MHz, a passband of 25MHz, and a passband ripple of 0.05dB. The noise power spectrum σ_c^2 is chosen to generate noise similar to the noise from the experiments. An example power spectrum from $P_{O_{(n,d)}}$, as described by Equation 5.62, is shown in Figure 5.18 with the noise floor at -45dB. To simulate this noise, the power spectrum of $n_c(t)$ is $\sigma_c^2 = 3x10^{-5}$.

The probe signal used to probe Υ_1 and Υ_2 for the simulations is a linear chirp probe signal

$$p(t) = Acos(2\pi(f_0 + \frac{(f_1 - f_0)}{2t_1}t)t) \tag{5.78}$$

where A is the amplitude, f_0=495MHz is the start frequency at $t = 0$, f_1=505MHz is the end frequency at $t_1 = 1000ns$. Since transients are not a concern here, only the linear chirp signal is used to probe each circuit model.

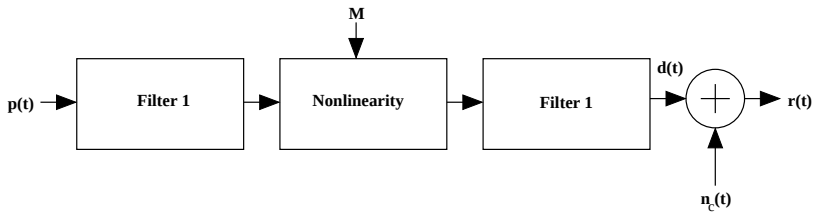

(a) Υ_1

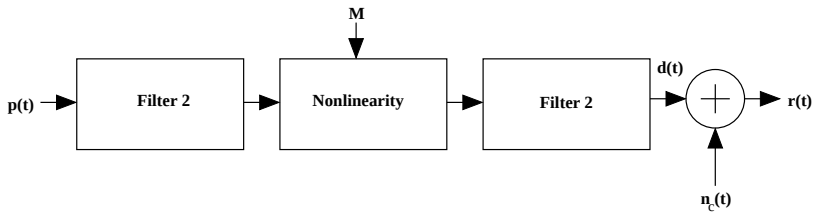

(b) Υ_2

Fig. 5.17. Circuit Models Used in the Simulations.

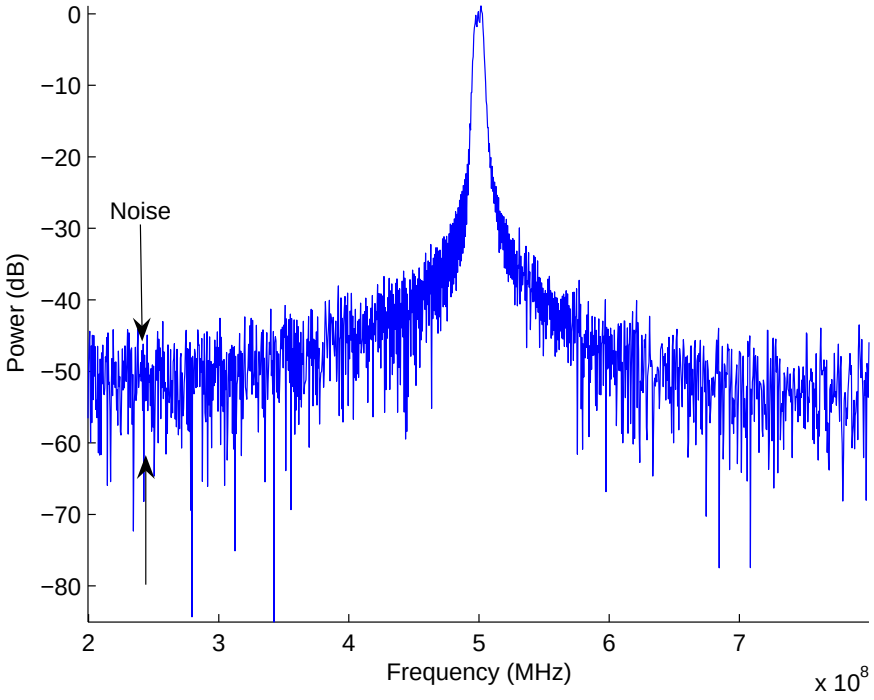

Fig. 5.18. Example Power Spectrum from the Linear Chirp Experiments. The noise is between -55dB and -45dB.

Three sets of probe signals are designed using $p(t)$ in Equation 5.78. Each set will use a different amplitude A. The first set of probe signals is $P_1 = \{p_{(1,1)}(t), ...p_{(1,L)}(t)\}$, where $p_{(1,l)}(t) = p(t)$, A=0.316 volts, $l \in \{1, ...L\}$, and $L = 100$. The second set of probe signals is $P_2 = \{p_{(2,1)}(t), ...p_{(2,L)}(t)\}$, where $p_{(2,l)}(t) = p(t)$, and A=0.562 volts. The third set of probe signals is $P_3 = \{p_{(3,1)}(t), ...p_{(3,L)}(t)\}$, where $p_{(3,l)}(t) = p(t)$, and A=1.0 volts.

Generation of the Return Signals

The return signals for the simulations are created by a similar procedure as used in the experiments, except that the probe signals are input into the circuit models instead of physical RF circuits. The probe signals in P_1 are input into both circuit models Υ_1 and Υ_2. The probe signals in P_2 are input into Υ_1. The probe signals in P_3 are input into Υ_2. A given return signal is known as $r_{(n,d,l)}(t)$, where $n \in \{1, 2, 3\}$ denotes the set P_n, $d \in \{1, 2\}$ denotes the RF circuit Υ_d, and $l \in \{1, ...L\}$ denotes the probe signal $p_l(t) \in P_n$. Each return signal will have a label (ground truth) associated with it, which is used to denote the circuit model and the return signal. Each return signal and label pair are known as an observation. The set of observations is defined as

$$O_{(n,d)} = \{[r_{(n,d,1)}(t), \gamma_{(n,d,1)} = d], ...[r_{(n,d,L)}(t), \gamma_{(n,d,L)} = d]\} \tag{5.79}$$

where $\gamma_{(n,d,l)} = d$ is the ground truth label. The set of observations produced by both circuit models is

$$O = \{O_{(1,1)}, O_{(1,2)}, O_{(2,1)}, O_{(3,2)}\} \tag{5.80}$$

Note that the total number of signals in Equation 5.80 is 400. The power spectrums of the signals in the set $O_{(n,d)}$ are

$$P_{O_{(n,d)}} = \{[P_{r_{(n,d,1)}}(f), \gamma_{(n,d,1)} = d], ...[P_{r_{(n,d,L)}}(f), \gamma_{(n,d,L)} = d]\} \tag{5.81}$$

where

$$P_{r_{(n,d,l)}}(f) = R_{(n,d,l)}(f)[R_{(n,d,l)}(f)]^* \tag{5.82}$$

and

$$R_{(n,d,l)}(f) = \int_{-\infty}^{\infty} r_{(n,d,l)}(t)e^{-i2\pi ft}dt \tag{5.83}$$

The power spectrums form the set

$$P_O = \{P_{O_{(1,1)}}, P_{O_{(1,2)}}, P_{O_{(2,1)}}, P_{O_{(3,2)}}\} \tag{5.84}$$

Features Selection

Features are extracted from each power spectrum in Equation 5.84 using the exact same procedure described in Section 5.4.1 for the experiments. A set of training vectors are formed by

$$\boldsymbol{\Theta} = \{[\boldsymbol{\theta}_1, \tau_1], ...[\boldsymbol{\theta}_\mathbf{J}, \tau_\mathbf{J}]\} \tag{5.85}$$

and a set of test vectors are formed by

$$\boldsymbol{\Omega} = \{[\boldsymbol{\omega}_1, \lambda_1], ...[\boldsymbol{\omega}_\mathbf{I}, \lambda_\mathbf{I}]\} \tag{5.86}$$

For the training set in Equation 5.85, the number of total observations and the number observations per category are shown in Table 5.18. For the test set in Equation 5.86, the total number of observations and the number observations per category are shown in Table 5.19.

Simulation Results

An average classification accuracy is measured for each category and each classifier using the exact same procedure discussed in Section 5.4.1. Once again, several

Table 5.18
Number of Feature Vectors Per Category for the Training Set. Features Vectors are Used in the Linear Chirp Simulations.

$\mathbf{J}$	$\mathbf{Q}_1$	$\mathbf{Q}_2$
199	95	104

Table 5.19
Number of Feature Vectors Per Category for the Testing Set. Features Vectors are Used in the Linear Chirp Simulations.

$\mathbf{I}$	$\mathbf{R}_1$	$\mathbf{R}_2$
201	105	96

parameters must be tested for the K-NN classifier, PW classifier, and SVM classifier priori to classification. The K-NN classifier requires the number of nearest neighbors, K_J, prior to classification. Let the parameter set for the K-NN classifier be $\Pi = \{\pi_1 = 1, ...\pi_{99} = 99\}$, where the parameters correspond to the number of nearest neighbors used by the classifier. It was determined that $v_{max} = 50$, therefore $K_J = \pi_{50} = 50$. The PW classifier requires the window width, h, prior to classification. Let the parameter set for the PW classifier be $\Pi = \{\pi_1 = 0.1, \pi_2 = 0.2, ...\pi_{50} = 5.0\}$, where these parameters correspond to the window width used by the classifier. It was determined that $v_{max} = 2$, therefore $h = \pi_2 = 0.2$. The SVM classifier requires two inputs C and γ prior to classification. Note that $C \in \{c_1 = 1, c_2 = 2, ...c_{19} = 19\}$ and $\gamma \in \{\gamma_1 = 0.1, \gamma_2 = 0.2, ...\gamma_{19} = 1.9\}$. Let the parameter set for the SVM classifier be $\Pi = \{\pi_1 = \{c_1, \gamma_1\}, ...\pi_{361} = \{c_{19}, \gamma_{19}\}\}$. It was determined that $v_{max} = 109$, therefore $C = 6$ and $\gamma = 1.4$.

The average classification accuracy of each classifier for each circuit model is shown in Table 5.20. As shown, a large number of classification errors occur. These results indicate that the ripple in the passband of the filter response is not distinct. This fact is illustrated using Figure 5.19 where an example power spectrum is shown for Υ_1 and Υ_2, the passband ripple pattern is not distinct.

These results are disappointing in that they are different from those of the experiments discussed in Section 5.4.1. For the experiments, the ripple patterns were distinct thereby leading to high classification accuracies. This suggests that the distinct ripple patterns produced by the Chebyshev filters in the RF circuits from the experiments could be generated by another source. For example, the ripple patterns could be caused by nonlinearities of the circulator used in the measurement system of Figure 5.14. These results indicate that our simulation approach needs further investigation to validate it against actual measurement data.

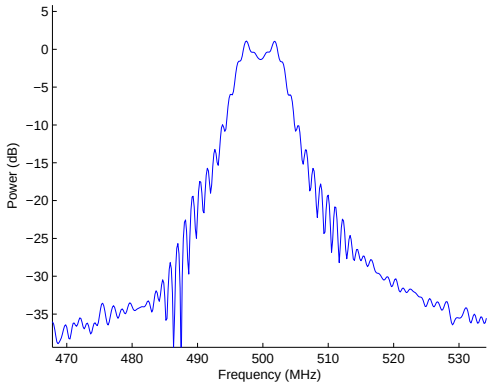

(a) Example Power Spectrum from Υ_1

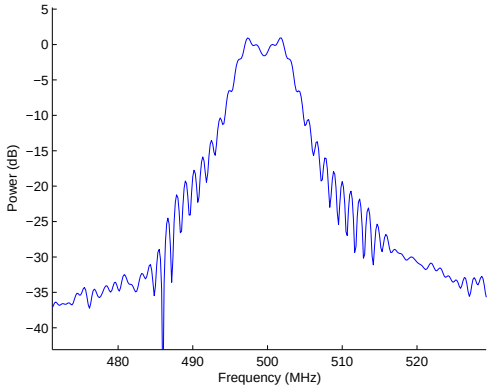

(b) Example Power Spectrum from Υ_2

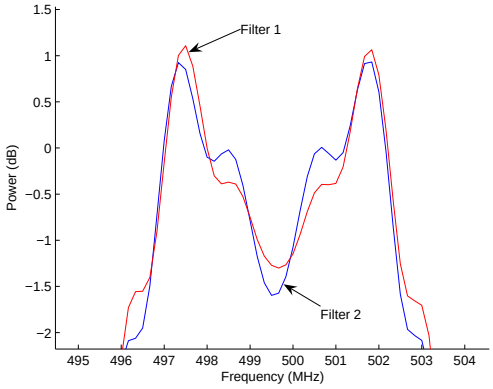

(c) Example Power Spectrum from Υ_1 and Υ_2

Fig. 5.19. Power Spectrums for the Linear Chirp Simulations. The Passband Ripple is Not Distinct.

Table 5.20
Classification Results for the Linear Chirp Simulation.

	P_1	P_2
SVM	54.3%	59.4%
BT	48.6%	47.9%
Bayesian$_\mu$	3.8%	100%
Bayesian$_\Sigma$	51.4%	57.3%
PW	56.2%	54.2%
K-NN	46%	73%

5.4.3 Conclusions

The results of the experiment indicate that the ripple patterns in the passband of the estimated filter response for each Chebyshev filter are distinct. This distinct pattern can be used to characterize each real RF circuit. However, these results were not verified by the simulations. The distinct ripple patterns produced by the Chebyshev filters in the RF circuits could be generated by another source. Further experimentation is required to determine if the ripple patterns, or other features of the estimated filter response, can be used to characterize the RF filter. These results indicate that our simulation approach needs further investigation to validate it against actual measurement data.

For example, consider the passband of the RF filters used in the experiment. The passband of Filter 1 of Figure 5.13 from Section 5.4.1 is defined to be 487.5MHz - 512.5MHz. Also, the passband of Filter 2 of Figure 5.13 is defined to be 490MHz - 510MHz. Remember that the linear chirp probe signal was defined using $f_0 = 495$MHz - $f_1 = 505$MHz, which does not cover the entire passband of either filter. Therefore, it may be possible that if the linear chirp probe signal was defined over the entire passband of both filters, for example $f_0 = 485$MHz - $f_1 = 515$MHz, then other distinct information may be available.

5.5 Summary of Simulations

Three simulations and one experiment were presented in this Chapter. In the first simulation presented in Section 5.2, we developed a method to forensically characterize RF circuit models using first order distortion (FOD) and intermodulation distortion (IMD) caused by a nonlinearity in response to a two-tone probe signal. Classification errors occurred when the return signal is close to the noise floor. In the second simulation presented in Section 5.3, we developed a method to forensically characterize RF circuit models using harmonic distortion and using the estimated filter response. Again, classification errors occurred when the return signal is close to the noise floor. In Section 5.4, we developed a method to forensically characterize physical RF circuits and circuit models using the filter response of two Chebyshev filters. The results indicated that further experimentation is needed to determine if the ripple patterns can be used to characterize the filter responses.

Although the linear chirp simulations/experiments of Section 5.4 demonstrated that the experimental results were inconclusive and further study is needed, there is no evidence to suggest that the results for the two-tone simulations of Section 5.2 and the Gaussian chirp simulations of Section 5.3 are also inconclusive. For the two-tone simulations, the circuit models were designed to simulate experimental data that was described in Section 1.3 of Chapter 1. The features used in the Gaussian chirp simulations are a mix of features taken from the harmonic distortion and the estimated filter responses. The results of the Gaussian chirp simulations demonstrated a high classification accuracy based on using these mixed features. It is therefore possible that these features can be used to accurately characterize physical RF circuits.

Of the three simulations presented in this Chapter, the Gaussian chirp simulations demonstrated that circuit models can be characterized based on features sampled from harmonic distortion produced by nonlinearities and based on features from the estimated filter response. We believe that the Gaussian chirp probe signal is the most effective probe signal of the three that were examined in this dissertation. Two

feature extraction techniques were implemented in the Gaussian chirp simulations. It was shown in Section 5.3.5 that features selected at precise locations produced higher classification accuracies then features selected at regular intervals. We therefore conclude that smaller sized feature vectors that contain feature patterns selected at precise locations produce a higher classification accuracy than larger sized feature vectors sampled at regular intervals.

6. CONCLUSIONS AND FUTURE WORK

In this dissertation we have proposed a forensic fingerprinting approach for RF device. This approach can theoretically be used to characterize any RF device. In this Chapter, we will briefly summarize the main contributions of this dissertation and discuss possible future developments.

6.1 Contributions

The contributions of this dissertation are as follows:

- Mathematical analysis of the output of a nonlinear system when a Gaussian chirp signal is its input. The power spectral density is derived in closed form. This analysis was used in the simulations.
- Developed methods for forensically characterizing circuit models using intermodulation distortion generated by nonlinearities in response to a two-tone probe signal. Classification errors were examined when the return signal is close to the noise floor. These simulations were presented in Section 5.2 of Chapter 5.
- Developed methods for forensically characterizing circuit models using harmonic distortion generated by nonlinearities in response to a Gaussian chirp signal. Classification errors were examined when the return signal is close to the noise floor. These simulations were presented in Section 5.3 of Chapter 5.
- Developed methods for forensically characterizing circuit models using the filter response of two Chebyshev filters. The filter response was estimated by the Gaussian probe signal. Both experimental and simulation results were com-

pared. These results indicated that the distinct oscillating patterns in the passband of the "real" RF circuits may be caused by other sources.

- Comparison of classification accuracy of the pattern recognition methods.

6.2 Future Work

The following issues need to be further studied:

- Our RF model is relatively simple and needs to be validated against real observations.
- The methods we developed are based on simulations. How these techniques can be used to characterize actual RF devices needs to be studied.
- The generation of arbitrary RF probe signals, in particular chirped waveforms, is a difficult problem and also needs further study.
- How well our approach scales relative to a large number of RF circuits has not been determined.
- We did not investigate the computational complexity of our methods. How these techniques would be deployed in an actual system needs further investigation.
- We did not investigate characterizing circuit models with filters using intermodulation distortion generated by nonlinearities in response to a two-tone probe signal. When the filters are used in the circuit models, a priori information of the filter response is needed. Assuming that we have a priori information of the filter response, we can design the probe frequencies of the two-tone signal to be within the passband of the filter. Therefore the return signal, generated by a circuit model using a bandpass filter, in response to a two-tone probe signal with probe frequencies within the passband of this filter, would contain first order distortion and intermodulation distortion that can be used to characterize the circuit model.

- Additional chirp probe signals should be considered when characterizing RF devices. One example of an additional chirp signal is the exponential chirp signal [111], where its instantaneous frequency increases exponentially over time. Furthermore, different window functions, other then the Gaussian window, should be considered for the linear chirp signal. One popular window function is the rectangular window [80], which has been used with the linear chirp signal for several applications [48] [112]. Other window functions include Hanning and Hamming [8].

- A possible alternative RF device identification technique is synthetic aperture radar (SAR) imaging [113] [114]. With SAR a "radar" image of a target area is obtained. To construct a SAR image, several probe signals are first transmitted to the target area. The probe signals are scattered from the target area and are received by the SAR system. The received signals are used to form an image of the target area. Providing that an RF device is in the target area, a signature would be present in the SAR image and features can therefore be extracted based on this signature. The features from the SAR image can then be combined with features generated from a feature extraction method discussed in Chapter 3 of this dissertation. The "fused" features can then be used to characterize the RF device.

6.3 Publications

Journal Papers:

1. A.F. Martone and E.J. Delp, "Transcript Synchronization Using Local Dynamic Programming," IEEE Transactions on Multimedia (Pending Review).

2. A.F. Martone and E.J. Delp, "RF Fingerprinting Using Linear Chirp Signals," IEEE Transactions on Microwave Theory and Techniques (Pending Review).

Conference Papers:

1. A.F. Martone and E.J. Delp, "Characterization of RF Devices using Two-Tone Probe Signals," in Proceedings of the 2007 IEEE Workshop on Statistical Signal Processing, Madison, WI, August 2007.

2. K. Ranney, A. Martone, and M. Soumekh, "Indication of Slowly Moving Targets via Change Detection," in Proceedings of the SPIE Conference on Radar Sensor Technology XI, Orlando, Fl, April 2007, Volume 6547 - 65470L.

3. N. Khanna, A.K. Mikkilineni, A.F. Martone, G.N. Ali, G.T.C. Chiu, J.P. Allebach, and E.J. Delp, "A Survey of Forensic Characterization Methods for Physical Devices," in Proceedings of the 6th Workshop on Digital Forensics Research, Lafayette, Indiana, August 2006, pp. 17-28.

4. A.F. Martone, A.K. Mikkilineni, and E.J. Delp, "Forensics of things," in Proceedings of the 2006 IEEE Southwest Symposium on Image Analysis and Interpretation, Denver, Colorado, March 2006, pp. 149-152.

5. A.F. Martone and E.J. Delp, "Forensic characterization of RF circuits," in Proceedings of Government Microcircuit Applications and Critical Technology Conference 06 (GOMACTech06), San Diego, California, March 2006, pp. 224-227.

6. A.F. Martone and E.J. Delp, "An Overview of the Use of Closed Caption Information for Video Indexing and Searching," in Proceedings of the 4th International Workshop on Content-Based Multimedia Indexing (CBMI), Riga, Latvia, June 21-23, 2005.

7. A.F. Martone, C. Taskiran, and E.J. Delp, "Multimodal Approach for Speaker Identification in News Programs," in Proceedings of the SPIE International Conference on Storage and Retrieval Methods and Applications for Multimedia, San Jose, CA, January 2005.

8. A. Martone, C. Taskiran, R. Browning, and E. Delp, "A Toolset for Broadcast Automation for the C-SPAN Networks," in Proceedings of the 5th International Workshop on Image Analysis for Multimedia Interactive Services (WIAMIS), Lisbon, Portugal, April 21-23, 2004.

9. A.F. Martone, C. Taskiran, and E.J. Delp, "Automated closed-captioning using text alignment," in Proceedings of the SPIE International Conference on Storage and Retrieval Methods and Applications for Multimedia, San Jose, CA, Jan. 20-22, 2004, pp. 108-116.

LIST OF REFERENCES

LIST OF REFERENCES

[1] A. L. Walker, "Behavioral modeling and characterization of nonlinear operation in rf and microwave systems," Ph.D. dissertation, North Carolina State University, 2005.

[2] J. Pedro and N. Carvalho, *Intermodulation Distortion in Microwave and Wireless Circuits*. Norwood, MA: Artech House, INC., 2003.

[3] V. Golikov, S. Hienonen, and P. Vainikainen, "Passive intermodulation distortion measurements in mobile communication antennas," in *Proceedings of the IEEE 54th Conference on Vehicular Technology*, vol. 4, Atlantic City, NJ, October 2001, pp. 2623–2625.

[4] A. Ortiz, C. Gherasim, M. Manana, C. Renedo, L. Eguiluz, and R. Belmans, "Total harmonic distortion decomposition depending on distortion origin," *IEEE Transactions on Power Delivery*, vol. 20, no. 4, pp. 2651–2656, October 2005.

[5] D. Shmilovitz, "On the definition of total harmonic distortion and its effects on measurement interpretation," *IEEE Transactions on Power Delivery*, vol. 20, no. 1, pp. 526–528, January 2005.

[6] G. Heiter, "Characterization of nonlinearities in microwave devices and systems," *IEEE Transactions on Microwave Theory and Techniques*, vol. 21, no. 12, pp. 797–805, June 1973.

[7] K. Gharaibeh, K. Gard, H. Gutierrez, and M. B. Steer, "The importance of nonlinear order in modeling intermodulation distortion and spectral regrowth," in *Proceedings of the IEEE 2002 Conference on Radio and Wireless*, November 2002, pp. 161–164.

[8] J. Proakis and D. Manolakis, *Digital Signal Processing*, 4th ed. Upper Saddle River, NJ: Prentice-Hall, 1996.

[9] A. Oppenheim, A. Willsky, and H. Nawab, *Signals and Systems*, 2nd ed. Upper Saddle River, NJ: Prentice-Hall, 1997.

[10] N. B. Carvalho, J. C. Pedro, W. Jang, and M. B. Steer, "Nonlinear simulation of mixers for assessing system-level performance," *International Journal on Microwave and Millimeter Wave Computer Aided Engineering*, vol. 15, no. 4, pp. 350–361, July 2005.

[11] R. Ludwig and P. Bretchko, *RF circuit design theory and application.* Upper Saddle River, NJ: Prentice-Hall, 2000.

[12] L. Besser and R. Gilmore, *Practical RF Circuit Design for Modern Wireless Systems*, 1st ed. Norwood, MA: Artech House Inc, 2003.

[13] F. Deflaviis, T. Rozzi, F. Moglie, A. Sgreccia, and A. Panzeri, "Accurate analysis and design of millimeter wave mixers," *IEEE Transactions on Microwave Theory and Techniques*, vol. 41, no. 5, pp. 870 – 873, May 1993.

[14] S. Peng, P. McCleer, and G. Haddad, "Nonlinear models for the intermodulation analysis of fet mixers," *IEEE Transactions on Microwave Theory and Techniques*, vol. 43, no. 5, pp. 1037 – 1045, May 1995.

[15] G. Rhyne and M. Steer, "Generalized power series analysis of intermodulation distortion in a mesfet amplifier: Simulation and experiment," *IEEE Transactions on Microwave Theory and Techniques*, vol. 35, no. 12, pp. 1248–1255, December 1987.

[16] P. Rudge, R. Miles, M. Steer, and C. Snowden, "Investigation into intermodulation distortion in hemts using a quasi-2-d physical model," *IEEE Transactions on Microwave Theory and Techniques*, vol. 49, no. 12, pp. 2315–2321, December 2001.

[17] ——, "Two-tone intermodulation distortion simulations in the time domain using a quasi-2d physical phemt model," in *Proceedings of the 2001 IEEE MTT-S International Microwave Symposium Digest*, vol. 1, Phoenix, AZ, May 2001, pp. 439–442.

[18] S. Hienonen, V. Golikov, P. Vainikainen, and A. Raisanen, "Near-field scanner for the detection of passive intermodulation sources in base station antennas," *IEEE Transactions on Electromagnetic Compatibility*, vol. 46, no. 4, pp. 661–667, November 2004.

[19] P. Lui, "Passive intermodulation interference in communication systems," *Electronics and Communication Engineering Journal*, vol. 2, no. 3, pp. 109–118, June 1990.

[20] P. Lui and A. D. Rawlins, "Passive non-linearities in antenna systems," in *Proceedings of the IEE Colloquium on Passive Intermodulation Products in Antennas and Related Structures*, June 1989, pp. 6/1–6/7.

[21] J. Russert, A. Ramachandrant, A. Cangellaris, and P. Russer, "Phenomenological modeling of passive intermodulation (pim) due to electron tunnelling at metallic contacts," in *Proceedings of the IEEE MTT-S International Microwave Symposium Digest*, San Francisco, CA, June 2006, pp. 1129–1132.

[22] A. Ramachandran and A. Cangellaris, "Passive intermodulation in planar transmission lines due to ohmic loss heating," in *Proceedings of Government Microcircuit Applications and Critical Technology Conference 06 (GOMACTech06)*, San Diego, CA, March 2006, pp. 27 – 30.

[23] J. Henrie, A. Christianson, and W. Chappell, "Prediction of passive intermodulation from coaxial connectors in microwave networks," *IEEE Transactions on Microwave Theory and Techniques (Pending Publication)*, July 2007.

[24] W. Chappell, A. Christianson, and J. Henrie, "Nonlinear measurements of high power passive components for differentiation of passive intermodulation sources," in *Proceedings of Government Microcircuit Applications and Critical Technology Conference 06 (GOMACTech06)*, San Diego, CA, March 2006, pp. 19 – 22.

[25] J. Martins and N. Carvalho, "Multitone phase and amplitude measurement for nonlinear device characterization," *IEEE Transactions on Microwave Theory and Techniques*, vol. 53, no. 6, pp. 1982–1989, June 2005.

[26] K. Gharaibeh, K. Gard, and M. Steer, "In-band distortion of multisines," *IEEE Transactions on Microwave Theory and Techniques*, vol. 54, no. 8, pp. 3227–3236, August 2006.

[27] K. Remely, D. Williams, D. Schreurs, and J. Wood, "Simplifying and interpreting two-tone measurements," *IEEE Transactions on Microwave Theory and Techniques*, vol. 52, no. 11, pp. 2576–2584, November 2004.

[28] A. F. Martone and E. J. Delp, "Forensic characterization of rf circuits," in *Proceedings of Government Microcircuit Applications and Critical Technology Conference 06 (GOMACTech-06)*, San Diego, California, March 2006, pp. 224–227.

[29] N. Boulejfen, A. Harguem, and F. Ghannouchi, "New closed-form expressions for the prediction of multitone intermodulation distortion in fifth-order nonlinear rf circuits/systems," *IEEE Transactions on Microwave Theory and Techniques*, vol. 52, no. 1, pp. 121 – 132, January 2004.

[30] K. G. Gard, H. Gutierrez, and M. B. Steer, "A statistical relationship for power spectral regrowth in digital cellular radio," in *Proceedings of the IEEE MTT-S International Microwave Symposium Digest*, vol. 2, Baltimore, MD, June 1998, pp. 989–992.

[31] J. Pla and W. Struble, "Nonlinear model for predicting intermodulation distortion in gaas fet rf switch devices," in *Proceedings of the IEEE MTT-S International Microwave Symposium Digest*, vol. 2, Atlanta, GA, May 1993, pp. 641–644.

[32] J. Chen and S. Kang, "An algorithm for automatic model-order reduction of nonlinear mems devices," in *Proceedings of the 2000 IEEE International Symposium on Circuits and Systems*, Geneva, May 2000, pp. 445–448.

[33] F. Tuttle and W. Kock, "A holographic pulse compression technique employing amplitude modulation," *Proceedings of the IEEE*, vol. 58, no. 1, pp. 153 – 154, January 1970.

[34] L. Guizhou, H. Qiang, and W. Zhensheng, "A new chirp-coded radar waveform," in *Proceedings of the International Conference on Computational Electromagnetics and Its Applications*, November 2004, pp. 344 – 347.

[35] P. Dalachartre, D. Vray, F. Peyrin, A. Dziedzic, and G. Gimenez, "Time-frequency analysis applied to sandy bottom echoes," in *Proceedings of the IEEE 1992 Symposium on Ultrasonics*, vol. 1, Tucson, AZ, October 1992, pp. 345 – 348.

[36] C. Cook, "Linear fm signal formats for beacon and communication systems," *IEEE Transactions on Aerospace and Electronic Systems*, vol. 10, no. 4, pp. 471–478, July 1974.

[37] J. Wilhjelm, "Bandwidth expressions of gaussian weighted chirp," *Electronics Letters*, vol. 29, no. 25, pp. 2161 – 2162, December 1993.

[38] M. Skolnik, *Introduction to Radar Systems*. New York, NY: McGraw-Hill, 2001.

[39] T. Folkestad and K. S. Mylvaganam, "Chirp excitation of ultrasonic probes and algorithm for filtering transit times in high-rangeability gas flow," *IEEE Transactions on Ultrasonics, Ferroelectrics, and frequency control*, vol. 40, no. 3, pp. 193–215, May 1993.

[40] A. Biggs, "High power microwave generation with pulse compression," in *Proceedings of the Tenth IEEE International Conference on Pulsed Power*, vol. 1, Albuquerque, NM, July 1995, pp. 697–698.

[41] N. Tzannes, *Communication and Radar Systems*. Englewood Cliffs, NJ: Prentice-Hall, 1985.

[42] G. Turin, "An introduction to matched filters," *IEEE Transactions on Information Theory*, vol. 6, no. 3, pp. 311– 329, July 1960.

[43] M. Bennett, S. McLauglin, T. Anderson, and N. McDicken, "Filtering of chirped ultrasound echo signals with the fractional fourier transform," in *Proceedings of the 2004 IEEE Symposium on Ultrasonics*, vol. 3, August 2004, pp. 2036 – 2040.

[44] S. Hengstler, D. Kasilingam, and A. Costa, "A novel chirp modulation spread spectrum technique for multiple access," in *Proceedings of the IEEE Seventh International Symposium on Spread Spectrum Techniques and Applications*, vol. 1, September 2002, pp. 73 – 77.

[45] R. Pickholtz, D. Schilling, and L. Milstein, "Theory of spread-spectrum communications - a tutorial," *IEEE Transactions on Communications*, vol. 30, no. 5, pp. 855 – 884, May 1982.

[46] M. Farhang and J. Salehi, "Spread-time/time-hopping uwb cdma communication," in *Proceedings of the IEEE International Symposium on Communications and Information Technologies*, vol. 2, October 2004, pp. 1047 – 1050.

[47] T. Wang, Y. Wang, and K. Chen, "Ultra wideband impulse radio spectrum control independent of time hopping codes," in *Proceedings of the IEEE 59th Conference on Vehicular Technology*, vol. 3, May 2004, pp. 1401 – 1405.

[48] I. Lin, J. McKinney, and A. Weiner, "Shaping the power spectrum of ultra-wideband radio-frequency signals," *IEEE Transactions on Microwave Theory and Techniques*, vol. 54, no. 12, pp. 4247–4255, December 2006.

[49] ——, "Photonic synthesis of broadband microwave arbitrary waveforms applicable to ultra-wideband communication," *IEEE Microwave and Wireless Components Letters*, vol. 15, no. 4, pp. 226 – 228, April 2005.

[50] A. F. Martone, A. K. Mikkilineni, and E. J. Delp, "Forensics of things," in *Proceedings of the 2006 IEEE Southwest Symposium on Image Analysis and Interpretation*, Denver, Colorado, March 2006, pp. 149–152.

[51] K. Fukunaga, *Introduction to Statistical Pattern Recognition*. San Diego, Ca: Academic Press, 1990.

[52] T. Ko, "Fingerprint enhancement by spectral analysis techniques," in *Proceedings of the 31st Workshop on Applied Imagery Pattern Recognition*, October 2002, pp. 133–139.

[53] D. Keiswetter, I. Won, J. Miller, T. Bell, E. Cepedes, and K. O'Neill, "Discriminating capabilities of multifrequency emi data," in *Proceedings of the International Symposium on Geoscience and Remote Sensing, 2000*, vol. 4, Honolulu, HI, July 2000, pp. 1415–1417.

[54] I. Won, D. Keiswetter, and T. Bell, "Electromagnetic induction spectroscopy for clearing landmines," *IEEE Transactions on Geoscience and Remote Sensing*, vol. 39, no. 4, pp. 703–709, April 2001.

[55] Z. Li and Y. Tan, "Content-based video copy detection with video signature," in *Proceedings of the IEEE International Symposium on Circuits and Systems*, May 2006, pp. 4321–4324.

[56] A. Joly, O. Buisson, and C. Frelicot, "Statistical similarity search applied to content-based video copy detection," in *Proceedings of the 21st International Conference on Data Engineering Workshops*, April 2005, pp. 1285–1295.

[57] J. Oostveen, T. Kalker, and J. Haitsma, "Feature extraction and a database strategy for video fingerprinting," in *Proceedings of the 5th International Conference on Recent Advances in Visual Information Systems*, London, UK, February 2004, pp. 67 – 81.

[58] G. N. Ali, P.-J. Chiang, A. K. Mikkilineni, J. P. Allebach, G. T. Chiu, and E. J. Delp, "Intrinsic and extrinsic signatures for information hiding and secure printing with electrophotographic devices," in *Proceedings of the IS&T's NIP19: International Conference on Digital Printing Technologies*, vol. 19, New Orleans, LA, September 2003, pp. 511–515.

[59] G. N. Ali, P.-J. Chiang, A. K. Mikkilineni, G. T.-C. Chiu, E. J. Delp, and J. P. Allebach, "Application of principal components analysis and gaussian mixture models to printer identification," in *Proceedings of the IS&T's NIP20: International Conference on Digital Printing Technologies*, vol. 20, Salt Lake City, UT, October/November 2004, pp. 301–305.

[60] A. K. Mikkilineni, G. N. Ali, P.-J. Chiang, G. T. Chiu, J. P. Allebach, and E. J. Delp, "Signature-embedding in printed documents for security and forensic applications," in *Proceedings of the SPIE International Conference on Security, Steganography, and Watermarking of Multimedia Contents VI*, vol. 5306, San Jose, CA, January 2004, pp. 455–466.

[61] P.-J. Chiang, G. N. Ali, A. K. Mikkilineni, G. T.-C. Chiu, J. P. Allebach, and E. J. Delp, "Extrinsic signatures embedding using exposure modulation for information hiding and secure printing in electrophotographic devices," in *Proceedings of the IS&T's NIP20: International Conference on Digital Printing Technologies*, vol. 20, Salt Lake City, UT, October/November 2004, pp. 295–300.

[62] A. K. Mikkilineni, P.-J. Chiang, G. N. Ali, G. T.-C. Chiu, J. P. Allebach, and E. J. Delp, "Printer identification based on textural features," in *Proceedings of the IS&T's NIP20: International Conference on Digital Printing Technologies*, vol. 20, Salt Lake City, UT, October/November 2004, pp. 306–311.

[63] A. K. Mikkilineni, P.-J. Chiang, G. N. Ali, G. T. C. Chiu, J. P. Allebach, and E. J. Delp, "Printer identification based on graylevel co-occurrence features for security and forensic applications," in *Proceedings of the SPIE International Conference on Security, Steganography, and Watermarking of Multimedia Contents VII*, vol. 5681, San Jose, CA, March 2005, pp. 430–440.

[64] A. K. Mikkilineni, O. Arslan, P.-J. Chiang, R. M. Kumontoy, J. P. Allebach, G. T.-C. Chiu, and E. J. Delp, "Printer forensics using svm techniques," in *Proceedings of the IS&T's NIP21: International Conference on Digital Printing Technologies*, vol. 21, Baltimore, MD, October 2005, pp. 223–226.

[65] O. Arslan, R. M. Kumontoy, P.-J. Chiang, A. K. Mikkillineni, J. P. Allebach, G. T. C. Chiu, and E. J. Delp, "Identification of inkjet printers for forensic applications," in *Proceedings of the IS&T's NIP21: International Conference on Digital Printing Technologies*, vol. 21, Baltimore, MD, October 2005, pp. 235–238.

[66] P.-J. Chiang, A. K. Mikkilineni, O. Arslan, R. M. Kumontoy, G. T.-C. Chiu, E. J. Delp, and J. P. Allebach, "Extrinsic signature embedding in text document using exposure modulation for information hiding and secure printing in electrophotography," in *Proceedings of the IS&T's NIP21: International Conference on Digital Printing Technologies*, vol. 21, Baltimore, MD, October 2005, pp. 231–234.

[67] A. K. Mikkilineni, P.-J. Chiang, S. Suh, G. T. C. Chiu, J. P. Allebach, and E. J. Delp, "Information embedding and extraction for electrophotographic printing processes," in *Proceedings of the SPIE International Conference on Security, Steganography, and Watermarking of Multimedia Contents VIII*, San Jose, CA, January 2006.

[68] N. Khanna, A. Mikkilineni, A. Martone, G. Ali, G. Chiu, J. Allebach, and E. Delp, "A survey of forensic characterization methods for physical devices," *Digital Investigation*, vol. 3, no. 1, pp. 17–28, 2006.

[69] G. C. Holst, *CCD Arrays Cameras and Displays*. Bellingham, WA: SPIE Optical Engineering Press, 1998.

[70] N. Khanna, A. K. Mikkilineni, G. T. C. Chiu, J. P. Allebach, and E. J. Delp, "Forensic classification of imaging sensor types," in *Proceedings of the IX SPIE Conference on Security, Steganography, and Watermarking of Multimedia Contents*, vol. 6505, 02 2007, p. 65050U.

[71] ——, "Scanner identification using sensor pattern noise," in *Proceedings of the SPIE International Conference on Security, Steganography, and Watermarking of Multimedia Contents IX*, vol. 6505, 02 2007, p. 65051K.

[72] S. Sieka, "Active fingerprinting of 802.11 devices by timing analysis," in *Proceedings of the 3rd IEEE Conference on Consumer Communications and Networking*, January 2006, pp. 15–19.

[73] J. Franklin, D. McCoy, P. Tabriz, V. Neagoe, J. Randwyk, and D. Sicker, "Passive data link layer 802.11 wireless device driver fingerprinting," in *Proceedings of the 15th USENIX Symposium on Security*, Vancouver, Canada, July 2006, pp. 167–178.

[74] T. Kohno, A. Broido, and K. C. Claffy, "Remote physical device fingerprinting," *IEEE Transactions on Dependable Secure Computing*, vol. 2, no. 2, pp. 93–108, 2005.

[75] *Part 15 - Radio Frequency Devices*, Federal Communications Commission, 2006.

[76] *Part 15 - Radio Frequency Devices*, Federal Communications Commission, 2006, section 15.5, Part B.

[77] *Part 15 - Radio Frequency Devices*, Federal Communications Commission, 2006, section 15.3, Definitions.

[78] R. Sea, "An algebraic formula for amplitudes of intermodulation products involving an arbitrary number of frequencies," *Proceedings of the IEEE*, vol. 56, no. 8, pp. 1388–1389, August 1968.

[79] R. Sea and A. Vacroux, "On the computation of intermodulation products for a power series nonlinearity," *Proceedings of the IEEE*, vol. 57, no. 3, pp. 337–338, March 1969.

[80] L. Cohen, *Time-Frequency Analysis*. Upper Saddle River, NJ: Prentice Hall, 1995.

[81] Y. Shin, E. Powers, T. Choe, C. Hong, E. Song, J. Yook, and J. Park, "Application of time-frequency domain reflectometry for detection and localization of a fault on a coaxial cable," *IEEE Transactions on Instrumentation and Measurement*, vol. 54, no. 6, pp. 2493–2500, December 2005.

[82] C. Capus and K. Brown, "Fractional fourier transform of the gaussian and fractional domain signal support," *IEE Vision, Image, and Signal Processing*, vol. 150, no. 2, pp. 99 – 106, April 2003.

[83] C. J. C. Burges, "A tutorial on support vector machines for pattern recognition," *Data Mining and Knowledge Discovery*, vol. 2, no. 2, pp. 121–167, 1998.

[84] R. Duta, P. Hart, and D. Stork, *Pattern Classification*, 2nd ed. New York, NY: John Wiley and Sons INC, 2001.

[85] A. Papoulis and S. Pillai, *Probability, Random Variables, and Stochastic Processes*, 4th ed. New York, NY: McGraw-Hill, 2002.

[86] R. Duta and P. Hart, *Pattern Classification and Scene Analysis*. New York, NY: John Wiley and Sons INC, 1973.

[87] Y. Muto, H. Nagase, and Y. Hamamoto, "Evaluation of a modified parzen classifier in high dimensional spaces," in *Proceedings of the International Conference on Pattern Recognition*, vol. 2, Barcelona, Spain, September 2000, pp. 67 – 70.

[88] S. Fralick and R. Scott, "Nonparametric bayes-risk estimation," *IEEE Transactions on Information Theory*, vol. 17, no. 4, pp. 440 – 444, July 1971.

[89] G. Babich and O. Camps, "Weighted parzen windows for pattern classification," *IEEE Transactions on Pattern Analysis and Machine Intelligence*, vol. 18, no. 5, pp. 567 – 570, May 1996.

[90] G. Babich and L. Sibul, "Weighted parzen windows for radial basis function network design," in *Proceedings of the Asilomar Conference on Signals, Systems, and Computers*, vol. 2, Pacific Grove, CA, November 1994, pp. 897 – 901.

[91] N. Kwak and C. Choi, "Input feature selection by mutual information based on parzen window," *IEEE Transactions on Pattern Analysis and Machine Intelligence*, vol. 24, no. 12, pp. 1667 – 1671, December 2002.

[92] D. Tax and R. Duin, "Data description in subspaces," in *Proceedings of the International Conference on Pattern Recognition*, vol. 2, Barcelona, Spain, September 2000, pp. 672 – 675.

[93] A. Farag, R. Mohamed, and H. Mahdi, "Experiments in multimodality image classification and data fusion," in *Proceedings of the International Conference on Information Fusion*, vol. 1, July 2002, pp. 299 – 308.

[94] A. Garcia, *Probability and Random Processes for Electrical Engineering*, 2nd ed. NY: Addison-Wesley, 1994.

[95] L. Devroye, "Automatic pattern recognition: A study of the probability of error," *IEEE Transactions on Pattern Analysis and Machine Intelligence*, vol. 10, no. 4, pp. 530 – 543, July 1988.

[96] L. Breiman, J. Friedman, R. Olshen, and C. Stone, *Classification and Regression Trees*. Belmont, CA: Wadsworth, 1984.

[97] S. Safavian and D. Landgrebe, "A survey of decision tree classifier methodology," *IEEE Transactions on systems, Man, and Cybernetics*, vol. 21, no. 3, pp. 660–674, June 1991.

[98] S. Gelfand, C. Ravishankar, and E. Delp, "An iterative growing and pruning algorithm for classification tree design," *IEEE Transactions on Pattern Analysis and Machine Intelligence*, vol. 13, no. 2, pp. 163 – 174, February 1991.

[99] Y. Sun, "Normal mammogram analysis," Ph.D. dissertation, School of Electrical and Computer Engineering, Purdue University, August 2004.

[100] Y. Sun, C. Babbs, and E. Delp, "Normal mammogram classification based on regional analysis," in *Proceedings of the 45th Midwest Symposium on Circuits and Systems*, vol. 2, 2002, pp. 375 – 378.

[101] B. Schlkopf, C. Burges, and A. Smola, *Advances in Kernel Methods Support Vector Learning*. Cambridge, MA: MIT Press, 1999.

[102] J. Suykens, T. Gestel, J. Brabanter, B. Moor, and J. Vandewalle, *Least Squares Support Vector Machines*. River Edge, NJ: World Scientific Publishing Co., 2002.

[103] E. Chong and S. Zak, *An introduction to optimization*, 2nd ed. New York, NY: John Wiley and Sons, Inc., 2001.

[104] K. Muller, S. Mika, G. Rtsch, K. Tsuda, and B. Scholkopf, "An introduction to kernel-based learning algorithms," *IEEE Transactions on Neural Networks*, vol. 12, no. 2, pp. 181–201, March 2001.

[105] B. E. Boser, I. Guyon, and V. Vapnik, "A training algorithm for optimal margin classifiers," in *Proceedings of the fifth annual workshop on Computational learning theory*, Pittsburgh, Pennsylvania, 1992, pp. 144–152.

[106] S. Lyu, "Mercer kernels for object recognition with local features," in *Proceedings of the IEEE Computer Society Conference on Computer Vision and Pattern Recognition*, vol. 2, June 2005, pp. 223 – 229.

[107] C.-C. Chang and C.-J. Lin, *LIBSVM: a library for support vector machines*, 2001, software available at http://www.csie.ntu.edu.tw/~cjlin/libsvm.

[108] Q. Gu, *RF System Design of Transceivers for Wireless Communications*. New York, NY: Springer, 2005.

[109] M. Steer and P. Khan, "An algebraic formula for the output of a system with large-signal, multifrequency excitation," *Proceedings of the IEEE*, vol. 71, no. 1, pp. 177–179, January 1983.

[110] G. Vendelin, A. Pavio, and U. Rohde, *Mircowave Circuit Design Using Linear and Nonlinear Techniques*, 2nd ed. Hoboken, NJ: John Wiley and Sons Inc., 2005.

[111] G. Bonmassar and E. Schwartz, "Geometric invariance in space-variant vision systems: the exponential chirp transform," in *Proceedings of the 12th IAPR International Conference on Pattern Recognition*, vol. 3, Jerusalem, Israel, October 1994, pp. 204 – 207.

[112] T. Misaridis and J. Jensen, "An effective coded excitation scheme based on a predistorted fm signal and an optimized digital filter," in *Proceedings of the 1999 IEEE Symposium on Ultrasonics*, vol. 2, Tahoe, NV, October 1999, pp. 1589 – 1593.

[113] D. Yanting, P. Runkle, L. Carin, R. Damarla, A. Sullivan, M. Ressler, and J. Sichina, "Multi-aspect detection of surface and shallow-buried unexplodedordnance via ultra-wideband synthetic aperture radar," *IEEE Transactions on Geoscience and Remote Sensing*, vol. 39, no. 6, pp. 1259–1270, June 2001.

[114] K. Ranney, A. Martone, and M. Soumekh, "Indication of slowly moving targets via change detection," in *Proceedings of SPIE Radar Sensor Technology XI*, vol. 6547, Orlando, Fl, May 2007, p. 65470L.

[115] H. Anton and A. Herr, *Calculus with Analytical Geometry*, 5th ed. NY: John Wiley and Sons, 1995.

[116] C. Chui, *An introduction to wavelets*. San Diego, CA: Academic press, INC, 1992.

[117] E. Saff and A. Snider, *Funamentals of Complex Analysis*, 3rd ed. London: Pearson Education, Inc, 2003.

APPENDICES

A: Two-Tone Signal in the Time Domain

The derivation of the two-tone signal in the time domain is presented in this Section. The two-tone signal is defined as

$$x(t) = A_1 \cos(2\pi f_1 t) + A_2 \cos(2\pi f_2 t) \tag{A.1}$$

This signal is input into a power series of order M=3

$$y(t) = \sum_{j=1}^{3} a_j [A_1 \cos(2\pi f_1 t) + A_2 \cos(2\pi f_2 t)]^j \tag{A.2}$$

Equation A.2 is expanded as follows

$$\begin{aligned}
y(t) &= \sum_{j=1}^{3} a_j [A_1 \cos(2\pi f_1 t) + A_2 \cos(2\pi f_2 t)]^j \\
&= a_1 [A_1 \cos(2\pi f_1 t) + A_2 \cos(2\pi f_2 t)] + a_2 [A_1 \cos(2\pi f_1 t) + A_2 \cos(2\pi f_2 t)]^2 \\
&\quad + a_3 [A_1 \cos(2\pi f_1 t) + A_2 \cos(2\pi f_2 t)]^3 \\
&= a_1 A_1 \cos(2\pi f_1 t) + a_1 A_2 \cos(2\pi f_2 t) + a_2 (A_1)^2 \cos(2\pi f_1 t)^2 \\
&\quad + a_2 2 A_1 A_2 \cos(2\pi f_1 t) \cos(2\pi f_2 t) + a_2 (A_2)^2 \cos(2\pi f_2 t)^2 \\
&\quad + a_3 (A_1)^3 \cos(2\pi f_1 t)^3 + 3 a_3 (A_1)^2 A_2 \cos(2\pi f_1 t)^2 \cos(2\pi f_2 t) \\
&\quad + 3 a_3 A_1 (A_2)^2 \cos(2\pi f_1 t) \cos(2\pi f_2 t)^2 + a_3 (A_2)^3 \cos(2\pi f_2 t)^3
\end{aligned}$$

Two trigonometry identities are used to expand this development further. These identities are [115]

$$cos^2(a) = \frac{1}{2}(1 + cos[2a]) \tag{A.3}$$

$$cos(a)cos(b) = \frac{1}{2}cos(a+b) + \frac{1}{2}cos(a-b) \tag{A.4}$$

Applying these trigonometry identities produces the following

$$
\begin{aligned}
y(t) &= a_1 A_1 \cos(2\pi f_1 t) + a_1 A_2 \cos(2\pi f_2 t) + \frac{a_2 (A_1)^2}{2}[1 + \cos(2\pi [2f_1]t)] \\
&\quad + a_2 A_1 A_2 \cos(2\pi [f_1 + f_2]t) + a_2 A_1 A_2 \cos(2\pi [f_2 - f_1]t) \\
&\quad + \frac{a_2 (A_2)^2}{2}[1 + \cos(2\pi [2f_2]t)] + \frac{a_3 (A_1)^3}{2}\cos(2\pi f_1 t)[1 + \cos(2\pi [2f_1]t)] \\
&\quad + \frac{3a_3 (A_1)^2 A_2}{2}\cos(2\pi f_2 t)[1 + \cos(2\pi [2f_1]t)] \\
&\quad + \frac{3a_3 A_1 (A_2)^2}{2}\cos(2\pi f_1 t)[1 + \cos(2\pi [2f_2]t)] \\
&\quad + \frac{a_3 (A_2)^3}{2}\cos(2\pi f_2 t)[1 + \cos(2\pi [2f_2]t)] \\
&= a_1 A_1 \cos(2\pi f_1 t) + a_1 A_2 \cos(2\pi f_2 t) + \frac{a_2 (A_1)^2}{2}[1 + \cos(2\pi [2f_1]t)] \\
&\quad + a_2 A_1 A_2 \cos(2\pi [f_1 + f_2]t) + a_2 A_1 A_2 \cos(2\pi [f_2 - f_1]t) \\
&\quad + \frac{a_2 (A_2)^2}{2}[1 + \cos(2\pi [2f_2]t)] + \frac{a_3 (A_1)^3}{2}\cos(2\pi f_1 t) \\
&\quad + \frac{a_3 (A_1)^3}{4}[\cos(2\pi [3f_1]t) + \cos(2\pi [f_1]t)] + \frac{3a_3 (A_1)^2 A_2}{2}\cos(2\pi f_2 t) \\
&\quad + \frac{3a_3 (A_1)^2 A_2}{4}[\cos(2\pi [2f_1 + f_2]t) + \cos(2\pi [2f_1 - f_2]t)] \\
&\quad + \frac{3a_3 A_1 (A_2)^2}{2}\cos(2\pi f_1 t) + \frac{3a_3 A_1 (A_2)^2}{4}[\cos(2\pi [2f_2 + f_1]t) \\
&\quad + \cos(2\pi [2f_2 - f_1]t)] + \frac{a_3 (A_2)^3}{2}\cos(2\pi f_2 t) \\
&\quad + \frac{a_3 (A_2)^3}{4}[\cos(2\pi [3f_2]t) + \cos(2\pi [f_2]t)]
\end{aligned}
$$

Further reduction produces the following

$$
\begin{aligned}
y(t) &= a_1A_1\cos(2\pi f_1t) + a_1A_2\cos(2\pi f_2t) + \frac{a_2(A_1)^2}{2} + \frac{a_2(A_1)^2}{2}\cos(2\pi[2f_1]t) \\
&\quad + a_2A_1A_2\cos(2\pi[f_1+f_2]t) + a_2A_1A_2\cos(2\pi[f_2-f_1]t) + \frac{a_2(A_2)^2}{2} \\
&\quad + \frac{a_2(A_2)^2}{2}\cos(2\pi[2f_2]t) + \frac{a_3(A_1)^3}{2}\cos(2\pi f_1t) + \frac{a_3(A_1)^3}{4}\cos(2\pi[3f_1]t) \\
&\quad + \frac{a_3(A_1)^3}{4}\cos(2\pi f_1t) + \frac{3a_3(A_1)^2A_2}{2}\cos(2\pi f_2t) \\
&\quad + \frac{3a_3(A_1)^2A_2}{4}\cos(2\pi[2f_1+f_2]t) + \frac{3a_3(A_1)^2A_2}{4}\cos(2\pi[2f_1-f_2]t) \\
&\quad + \frac{3a_3A_1(A_2)^2}{2}\cos(2\pi f_1t) + \frac{3a_3A_1(A_2)^2}{4}\cos(2\pi[2f_2+f_1]t) \\
&\quad + \frac{3a_3A_1(A_2)^2}{4}\cos(2\pi[2f_2-f_1]t) + \frac{a_3(A_2)^3}{2}\cos(2\pi f_2t) \\
&\quad + \frac{a_3(A_2)^3}{4}\cos(2\pi[3f_2]t) + \frac{a_3(A_2)^3}{4}\cos(2\pi f_2t) \\
&= [\frac{a_2(A_1)^2}{2} + \frac{a_2(A_2)^2}{2}] \\
&\quad + [a_1A_1 + \frac{a_3(A_1)^3}{2} + \frac{a_3(A_1)^3}{4} + \frac{3a_3A_1(A_2)^2}{2}]\cos(2\pi f_1t) \\
&\quad + [a_1A_2 + \frac{3a_3(A_1)^2A_2}{2} + \frac{a_3(A_2)^3}{2} + \frac{a_3(A_2)^3}{4}]\cos(2\pi f_2t) \\
&\quad + [\frac{a_2(A_1)^2}{2}]\cos(2\pi[2f_1]t) + [\frac{a_2(A_2)^2}{2}]\cos(2\pi[2f_2]t) + [\frac{a_3(A_1)^3}{4}]\cos(2\pi[3f_1]t) \\
&\quad + [\frac{a_3(A_2)^3}{4}]\cos(2\pi[3f_2]t) + [a_2A_1A_2]\cos(2\pi[f_1+f_2]t) \\
&\quad + [a_2A_1A_2]\cos(2\pi[f_2-f_1]t) + [\frac{3a_3(A_1)^2A_2}{4}]\cos(2\pi[2f_1+f_2]t) \\
&\quad + [\frac{3a_3(A_1)^2A_2}{4}]\cos(2\pi[2f_1-f_2]t) + [\frac{3a_3A_1(A_2)^2}{4}]\cos(2\pi[2f_2+f_1]t) \\
&\quad + [\frac{3a_3A_1(A_2)^2}{4}]\cos(2\pi[2f_2-f_1]t)
\end{aligned}
$$

For simplicity, the constant coefficients will be defined by the parameters in Table A.1. $y(t)$ then becomes

Table A.1
Parameter Definitions for the Constants in $y(t)$.

Parameters	Parameter Description	Parameter Definition
b_0^1	Constant	$\frac{a_2(A_1)^2}{2} + \frac{a_2(A_2)^2}{2}$
b_1^1	1^{st} order harmonic	$a_1A_1 + \frac{a_3(A_1)^3}{2} + \frac{a_3(A_1)^3}{4} + \frac{3a_3A_1(A_2)^2}{2}$
b_1^2	1^{st} order harmonic	$a_1A_2 + \frac{3a_3(A_1)^2A_2}{2} + \frac{a_3(A_2)^3}{2} + \frac{a_3(A_2)^3}{4}$
b_2^1	2^{nd} order harmonic	$\frac{a_2(A_1)^2}{2}$
b_2^2	2^{nd} order harmonic	$\frac{a_2(A_2)^2}{2}$
b_3^1	3^{rd} order harmonic	$\frac{a_3(A_1)^3}{4}$
b_3^2	3^{rd} order harmonic	$\frac{a_3(A_2)^3}{4}$
b_4^1	2^{nd} order intermodulation	$a_2A_1A_2$
b_4^2	2^{nd} order intermodulation	$a_2A_1A_2$
b_5^1	3^{rd} order intermodulation	$\frac{3a_3(A_1)^2A_2}{4}$
b_5^2	3^{rd} order intermodulation	$\frac{3a_3(A_1)^2A_2}{4}$
b_5^3	3^{rd} order intermodulation	$\frac{3a_3A_1(A_2)^2}{4}$
b_5^4	3^{rd} order intermodulation	$\frac{3a_3A_1(A_2)^2}{4}$

$$
\begin{aligned}
y(t) &= b_0^1 + b_1^1\cos(2\pi f_1 t) + b_1^2\cos(2\pi f_2 t) + b_2^1\cos(2\pi[2f_1]t) + b_2^2\cos(2\pi[2f_2]t) \\
&+ b_3^1\cos(2\pi[3f_1]t) + b_3^2\cos(2\pi[3f_2]t) + b_4^1\cos(2\pi[f_1+f_2]t) + b_4^2\cos(2\pi[f_2-f_1]t) \\
&+ b_5^1\cos(2\pi[2f_1+f_2]t) + b_5^2\cos(2\pi[2f_1-f_2]t) + b_5^3\cos(2\pi[2f_2+f_1]t) \\
&+ b_5^4\cos(2\pi[2f_2-f_1]t)
\end{aligned}
\tag{A.5}
$$

Note that Equation A.5 is the same as Equation 2.7 from Chapter 2.

B: Two-Tone Signal in the Frequency Domain

$y(t)$, as defined by Equation A.5 in Appendix A, is transformed into the frequency domain by the Fourier transform:

$$Y(f) = F[y(t)] = \int_{-\infty}^{\infty} y(t)e^{-i2\pi ft}dt \tag{B.1}$$

For comparison purposes, we will also derive the Fourier transform of $x(t)$ in Equation A.1. First, let the Fourier transform of the constant $b \in \Re$ and the cosine function be [116] [9]

$$F[b] = b\delta(f) \tag{B.2}$$

$$F[\cos(bt)] = \frac{\delta(f - \frac{b}{2\pi}) + \delta(f + \frac{b}{2\pi})}{2} \tag{B.3}$$

where $\delta(f)$ is the Dirac Delta Function at $f = 0$. The Dirac Delta Function is defined in terms of the sifting property

$$z(f_1) = \int_{-\infty}^{\infty} z(f)\delta(f - f_1)df \tag{B.4}$$

where $f_1 \in \Re$ and $z(f)$ is a continuous function at f_1 and f_1 is a constant. Another property of the Dirac Delta Function is [41]

$$\delta(f - f_1) = 0 \tag{B.5}$$

for $f \neq f_1$. The Fourier transform of $x(t)$ is [9]

$$
\begin{aligned}
X(f) = F[x(t)] &= \int_{-\infty}^{\infty} x(t)e^{-i2\pi ft}dt \\
&= \int_{-\infty}^{\infty} [A_1\cos(2\pi f_1 t) + A_2\cos(2\pi f_2 t)]e^{-i2\pi ft}dt \\
&= A_1\int_{-\infty}^{\infty}\cos(2\pi f_1 t)e^{-i2\pi ft}dt + A_2\int_{-\infty}^{\infty}\cos(2\pi f_2 t)e^{-i2\pi ft}dt \\
&= \tfrac{A_1\delta(f-f_1)+A_1\delta(f+f_1)}{2} + \tfrac{A_2\delta(f-f_2)+A_2\delta(f+f_2)}{2}
\end{aligned}
\tag{B.6}
$$

where f_1 and f_2 are constants. Note that Equation B.6 is the same as Equation 2.2 from Chapter 2. The Fourier transform of $y(t)$ is derived as follows

$$
\begin{aligned}
Y(f) &= F[y(t)] \\
&= F[b_0^1 + b_1^1\cos(2\pi f_1 t) + b_1^2\cos(2\pi f_2 t) + b_2^1\cos(2\pi[2f_1]t) + b_2^2\cos(2\pi[2f_2]t) \\
&\quad + b_3^1\cos(2\pi[3f_1]t) + b_3^2\cos(2\pi[3f_2]t) + b_4^1\cos(2\pi[f_1+f_2]t) \\
&\quad + b_4^2\cos(2\pi[f_2-f_1]t) + b_5^1\cos(2\pi[2f_1+f_2]t) + b_5^2\cos(2\pi[2f_1-f_2]t) \\
&\quad + b_5^3\cos(2\pi[2f_2+f_1]t) + b_5^4\cos(2\pi[2f_2-f_1]t)]
\end{aligned}
$$

Using the linearity property [9] of the Fourier transform, $F[y(t)]$ is rewritten as

$$
\begin{aligned}
F[y(t)] &= F[b_0^1] + b_1^1 F[\cos(2\pi f_1 t)] + b_1^2 F[\cos(2\pi f_2 t)] + b_2^1 F[\cos(2\pi [2f_1] t)] \\
&\quad + b_2^2 F[\cos(2\pi [2f_2] t)] + b_3^1 F[\cos(2\pi [3f_1] t)] + b_3^2 F[\cos(2\pi [3f_2] t)] \\
&\quad + b_4^1 F[\cos(2\pi [f_1 + f_2] t)] + b_4^2 F[\cos(2\pi [f_2 - f_1] t)] \\
&\quad + b_5^1 F[\cos(2\pi [2f_1 + f_2] t)] + b_5^2 F[\cos(2\pi [2f_1 - f_2] t)] \\
&\quad + b_5^3 F[\cos(2\pi [2f_2 + f_1] t)] + b_5^4 F[\cos(2\pi [2f_2 - f_1] t)] \\
&= b_0^1 \delta(f) + \frac{b_1^1}{2}[\delta(f - f_1) + \delta(f + f_1)] + \frac{b_1^2}{2}[\delta(f - f_2) + \delta(f + f_2)] \\
&\quad + \frac{b_2^1}{2}[\delta(f - [2f_1]) + \delta(f + [2f_1])] + \frac{b_2^2}{2}[\delta(f - [2f_2]) + \delta(f + [2f_2])] \\
&\quad + \frac{b_3^1}{2}[\delta(f - [3f_1]) + \delta(f + [3f_1])] + \frac{b_3^2}{2}[\delta(f - [3f_2]) + \delta(f + [3f_2])] \\
&\quad + \frac{b_4^1}{2}[\delta(f - [f_1 + f_2]) + \delta(f + [f_1 + f_2])] \\
&\quad + \frac{b_4^2}{2}[\delta(f - [f_2 - f_1]) + \delta(f + [f_2 - f_1])] \\
&\quad + \frac{b_5^1}{2}[\delta(f - [2f_1 + f_2]) + \delta(f + [2f_1 + f_2])] \\
&\quad + \frac{b_5^2}{2}[\delta(f - [2f_1 - f_2]) + \delta(f + [2f_1 - f_2])] + \frac{b_5^3}{2}[\delta(f - [2f_2 + f_1]) \\
&\quad + \delta(f + [2f_2 + f_1])] + \frac{b_5^4}{2}[\delta(f - [2f_2 - f_1]) + \delta(f + [2f_2 - f_1])]
\end{aligned}
$$

The above can be rewritten as

$$
\begin{aligned}
&Y(f) = b_0^1 \delta(f) + \tfrac{b_1^1}{2}\delta(f - f_1) + \tfrac{b_1^1}{2}\delta(f + f_1) + \tfrac{b_1^2}{2}\delta(f - f_2) + \tfrac{b_1^2}{2}\delta(f + f_2) \\
&+ \tfrac{b_2^1}{2}\delta(f - [2f_1]) + \tfrac{b_2^1}{2}\delta(f + [2f_1]) + \tfrac{b_2^2}{2}\delta(f - [2f_2]) + \tfrac{b_2^2}{2}\delta(f + [2f_2]) \\
&+ \tfrac{b_3^1}{2}\delta(f - [3f_1]) + \tfrac{b_3^1}{2}\delta(f + [3f_1]) + \tfrac{b_3^2}{2}\delta(f - [3f_2]) + \tfrac{b_3^2}{2}\delta(f + [3f_2]) \\
&+ \tfrac{b_4^1}{2}\delta(f - [f_1 + f_2]) + \tfrac{b_4^1}{2}\delta(f + [f_1 + f_2]) + \tfrac{b_4^2}{2}\delta(f - [f_2 - f_1]) \\
&+ \tfrac{b_4^2}{2}\delta(f + [f_2 - f_1]) + \tfrac{b_5^1}{2}\delta(f - [2f_1 + f_2]) + \tfrac{b_5^1}{2}\delta(f + [2f_1 + f_2]) \\
&+ \tfrac{b_5^2}{2}\delta(f - [2f_1 - f_2]) + \tfrac{b_5^2}{2}\delta(f + [2f_1 - f_2])] + \tfrac{b_5^3}{2}\delta(f - [2f_2 + f_1]) \\
&+ \tfrac{b_5^3}{2}\delta(f + [2f_2 + f_1]) + \tfrac{b_5^4}{2}\delta(f - [2f_2 - f_1]) + \tfrac{b_5^4}{2}\delta(f + [2f_2 - f_1])
\end{aligned}
\tag{B.7}
$$

Note that Equation B.7 is the same as Equation 2.8 from Chapter 2.

The power spectrum of $Y(f)$ is determined by multiplying $Y(f)$ by its complex conjugate $Y^*(f)$, $P_y(f) = Y(f)Y^*(f)$. For the purposes of this research, we assume $\delta^*(f) = \delta(f)$. $P_y(f)$ is obtained as follows:

$$\begin{aligned}
P_y(f) &= Y(f)Y^*(f) = Y(f)^2 \\
&= [b_0^1\delta(f)]^2 + [b_0^1\delta(f)\frac{b_1^1}{2}\delta(f-f_1)] + ... + [b_0^1\delta(f)\frac{b_5^4}{2}\delta(f+[2f_2-f_1])] \\
&\quad +[\frac{b_1^1}{2}\delta(f-f_1)b_0^1\delta(f)] + ... + [\frac{b_1^1}{2}\delta(f-f_1)\frac{b_5^4}{2}\delta(f+[2f_2-f_1])] \\
&\quad + \quad ... \\
&\quad ... \\
&\quad + \quad ... \\
&\quad +[\frac{b_5^4}{2}\delta(f+[2f_2-f_1])b_0^1\delta(f)] + ... + [\frac{b_5^4}{2}\delta(f+[2f_2-f_1])]^2
\end{aligned}$$

The above equation contains square-terms and cross-terms. The square-terms consist of $\{\delta(f)^2, \delta(f-f_1)^2, ...\delta(f+[2f_2-f_1])^2\}$. Note that there exists 25 square-terms. The cross-terms consist of the set $\{[b_0^1\delta(f)][\frac{b_1^1}{2}\delta(f-f_1)], ...[\frac{b_5^4}{2}\delta(f+[2f_2-f_1])\frac{b_5^4}{2}\delta(f-[2f_2-f_1])]\}$. Since $f_1 \neq f_2$, Equation B.5 can be used to show that for any value of f, $\delta(f-f_1)\delta(f-f_2) = 0$. $P_y(f)$ is then

$$\begin{aligned}
&P_y(f) = [b_0^1]^2\delta(f)^2 + [\tfrac{b_1^1}{2}]^2\delta(f-f_1)^2 \\
&+[\tfrac{b_1^1}{2}]^2\delta(f+f_1)^2 + [\tfrac{b_1^2}{2}]^2\delta(f-f_2)^2 + [\tfrac{b_1^2}{2}]^2\delta(f+f_2)^2 \\
&+[\tfrac{b_2^1}{2}]^2\delta(f-[2f_1])^2 + [\tfrac{b_2^1}{2}]^2\delta(f+[2f_1])^2 + [\tfrac{b_2^2}{2}]^2\delta(f-[2f_2])^2 + [\tfrac{b_2^2}{2}]^2\delta(f+[2f_2])^2 \\
&+[\tfrac{b_3^1}{2}]^2\delta(f-[3f_1])^2 + [\tfrac{b_3^1}{2}]^2\delta(f+[3f_1])^2 + [\tfrac{b_3^2}{2}]^2\delta(f-[3f_2])^2 + [\tfrac{b_3^2}{2}]^2\delta(f+[3f_2])^2 \\
&+[\tfrac{b_4^1}{2}]^2\delta(f-[f_1+f_2])^2 + [\tfrac{b_4^1}{2}]^2\delta(f+[f_1+f_2])^2 + [\tfrac{b_4^2}{2}]^2\delta(f-[f_2-f_1])^2 \\
&+[\tfrac{b_4^2}{2}]^2\delta(f+[f_2-f_1])^2 + [\tfrac{b_5^1}{2}]^2\delta(f-[2f_1+f_2])^2 + [\tfrac{b_5^1}{2}]^2\delta(f+[2f_1+f_2])^2 \\
&+[\tfrac{b_5^2}{2}]^2\delta(f-[2f_1-f_2])^2 + [\tfrac{b_5^2}{2}]^2\delta(f+[2f_1-f_2])^2 + [\tfrac{b_5^3}{2}]^2\delta(f-[2f_2+f_1])^2 \\
&+[\tfrac{b_5^3}{2}]^2\delta(f+[2f_2+f_1])^2 + [\tfrac{b_5^4}{2}]^2\delta(f-[2f_2-f_1])^2 + [\tfrac{b_5^4}{2}]^2\delta(f+[2f_2-f_1])^2
\end{aligned} \tag{B.8}$$

Note that Equation B.8 is the same as Equation 2.9 from Chapter 2.

C: Fourier Transform of the Gaussian Chirp Signal

This Appendix provides the derivation of the Fourier Transform of the Gaussian Chirp Signal. Recall that $y(t)$ is the following

$$y(t) = \sum_{j=1}^{M} a_j (C_1)^j e^{ij\phi(t)} e^{\frac{-j(t-\mu)^2}{2\sigma^2}} \tag{C.1}$$

The Fourier transform of $y(t)$ is

$$\begin{aligned}
Y(f) &= \int_{-\infty}^{\infty} [\sum_{j=1}^{M} a_j (C_1)^j e^{ij\phi(t)} e^{\frac{-j(t-\mu)^2}{2\sigma^2}}] e^{-i2\pi ft} dt \\
&= \int_{-\infty}^{\infty} [\sum_{j=1}^{M} a_j (C_1)^j e^{ij[2\pi f_0 t + \pi k t^2]} e^{\frac{-j[t^2 - 2\mu t + \mu^2]}{2\sigma^2}}] e^{-i2\pi ft} dt \\
&= \int_{-\infty}^{\infty} [\sum_{j=1}^{M} a_j (C_1)^j e^{ij2\pi f_0 t} e^{ij\pi k t^2} e^{\frac{-jt^2}{2\sigma^2}} e^{\frac{j2\mu t}{2\sigma^2}} e^{\frac{-j\mu^2}{2\sigma^2}} e^{-i2\pi ft} dt \\
&= \sum_{j=1}^{M} [a_j (C_1)^j e^{\frac{-j\mu^2}{2\sigma^2}} \int_{-\infty}^{\infty} e^{-(\frac{j}{2\sigma^2} - ji\pi k)t^2 + (ji2\pi f_0 + \frac{j\mu}{\sigma^2} - i2\pi f)t} dt]
\end{aligned}$$

Define $p_1 = \frac{j}{2\sigma^2} - ji\pi k$, $p_2 = ji2\pi f_0 + \frac{j\mu}{\sigma^2} - i2\pi f$, and $(p_3)^2 = \frac{1}{2p_1}$. Substitute p_1 and p_2 into the above expression and reform the integral into a Gaussian density function. The integration of a Gaussian density function with full support is 1 [85].

$$
\begin{aligned}
Y(f) &= \sum_{j=1}^{M}[a_j(C_1)^j e^{\frac{-j\mu^2}{2\sigma^2}} \int_{-\infty}^{\infty} e^{-(p_1)t^2+(p_2)t} dt] \\
&= \sum_{j=1}^{M}[a_j(C_1)^j e^{\frac{-j\mu^2}{2\sigma^2}} \int_{-\infty}^{\infty} e^{-p_1[t^2-(\frac{p_2}{p_1})t+(\frac{-p_2}{2p_1})^2-(\frac{-p_2}{2p_1})^2]} dt] \\
&= \sum_{j=1}^{M}[a_j(C_1)^j e^{\frac{-j\mu^2}{2\sigma^2}} \int_{-\infty}^{\infty} e^{-p_1[t^2-(\frac{p_2}{p_1})t+(\frac{-p_2}{2p_1})^2]+p_1(\frac{-p_2}{2p_1})^2} dt] \\
&= \sum_{j=1}^{M}[a_j(C_1)^j e^{\frac{-j\mu^2}{2\sigma^2}} \int_{-\infty}^{\infty} e^{-p_1[t-\frac{p_2}{2p_1}]^2+\frac{(p_2)^2}{4p_1}} dt] \\
&= \sum_{j=1}^{M}[a_j(C_1)^j e^{\frac{-j\mu^2}{2\sigma^2}+\frac{(p_2)^2}{4p_1}} \int_{-\infty}^{\infty} e^{\frac{-[t-\frac{p_2}{2p_1}]^2}{2(p_3)^2}} \frac{\sqrt{2\pi(p_3)^2}}{\sqrt{2\pi(p_3)^2}} dt] \\
&= \sum_{j=1}^{M}[a_j(C_1)^j e^{\frac{-j\mu^2}{2\sigma^2}+\frac{(p_2)^2}{4p_1}} \sqrt{2\pi(p_3)^2}]
\end{aligned}
$$

Replace the definitions of p_1, p_2, and p_3 into the above produces

$$
\begin{aligned}
Y(f) &= \sum_{j=1}^{M} a_j(C_1)^j e^{\frac{-j\mu^2}{2\sigma^2}+\frac{(p_2)^2}{4p_1}} \sqrt{2\pi(p_3)^2} \\
&= \sum_{j=1}^{M} a_j(C_1)^j e^{\frac{-j\mu^2}{2\sigma^2}} e^{\frac{[ji2\pi f_0+\frac{j\mu}{\sigma^2}-i2\pi f]^2}{4[\frac{j}{2\sigma^2}-ji\pi k]}} \sqrt{2\pi(\frac{1}{2p_1})} \\
&= \sum_{j=1}^{M} a_j(C_1)^j e^{\frac{-j\mu^2}{2\sigma^2}} e^{\frac{(i)^2[j2\pi f_0+\frac{i}{i^2}\frac{j\mu}{\sigma^2}-2\pi f]^2}{\frac{4j}{2}[\frac{1}{\sigma^2}-2i\pi k]}} \sqrt{\frac{2\pi}{2[\frac{j}{2\sigma^2}-ji\pi k]}} \\
&= \sum_{j=1}^{M} a_j(C_1)^j e^{\frac{-j\mu^2}{2\sigma^2}} e^{\frac{-[j2\pi f_0-\frac{ij\mu}{\sigma^2}-2\pi f]^2}{2j[\frac{1}{\sigma^2}-2i\pi k]}} \sqrt{\frac{\pi}{\frac{j}{2\sigma^2}-ji\pi k}}
\end{aligned}
$$

The resulting expression for $Y(f)$ is

$$
Y(f) = \sum_{j=1}^{M} \frac{\sqrt{\pi} a_j(C_1)^j e^{\frac{-j\mu^2}{2\sigma^2}}}{\sqrt{\frac{j}{2\sigma^2}-ij\pi k}} e^{\frac{-(2\pi f-j2\pi f_0+\frac{ij\mu}{\sigma^2})^2}{2j(\frac{1}{\sigma^2}-i2\pi k)}} \tag{C.2}
$$

Equation C.2 is formed into its magnitude and phase components. The equation will be split into 4 parts and rewritten as $Y(f) = \sum_{j=1}^{M} \frac{p_4}{p_7} e^{\frac{p_5}{p_6}}$, where the terms p_4, p_5, p_6, and p_7 are defined and expanded below.

$$p_4 = \sqrt{\pi} a_j (C_1)^j e^{\frac{-j\mu^2}{2\sigma^2}} \tag{C.3}$$

$$\begin{aligned}
p_5 &= -(2\pi f - j2\pi f_0 + \tfrac{ij\mu}{\sigma^2})^2 \\
&= -(4\pi^2 f^2 - 4\pi^2 j f_0 f + \tfrac{2\pi ij\mu f}{\sigma^2} - 4\pi^2 j f_0 f + j^2 4\pi^2 f_0^2 \\
&- \tfrac{i2\pi j^2 f_0 \mu}{\sigma^2} + \tfrac{i2\pi j\mu f}{\sigma^2} - \tfrac{ij^2 2\pi\mu f_0}{\sigma^2} - \tfrac{j^2\mu^2}{\sigma^4}) \\
&= -4\pi^2 f^2 + 8\pi^2 j f_0 f - \tfrac{i4\pi j\mu f}{\sigma^2} + \tfrac{i4\pi j^2 f_0 \mu}{\sigma^2} - j^2 4\pi^2 f_0^2 + \tfrac{j^2\mu^2}{\sigma^4} \\
&= [-4\pi^2 f^2 + 8\pi^2 j f_0 f - j^2 4\pi^2 f_0^2 + \tfrac{j^2\mu^2}{\sigma^4}] + i[\tfrac{4\pi j^2 f_0 \mu}{\sigma^2} - \tfrac{4\pi j\mu f}{\sigma^2}] \\
&= [p_8 + i p_9]
\end{aligned} \tag{C.4}$$

$$\begin{aligned}
p_6 &= 2j(\tfrac{1}{\sigma^2} - i2\pi k) \\
&= \tfrac{2j}{\sigma^2}(1 - i2\pi\sigma^2 k) \\
&= \tfrac{2j}{\sigma^2}\sqrt{1 + (2\pi\sigma^2 k)^2} e^{i \arctan(\frac{-2\pi\sigma^2 k}{1})} \\
&= \tfrac{2j}{\sigma^2}\sqrt{1 + 4\pi^2\sigma^4 k^2} e^{-i \arctan(2\pi\sigma^2 k)} \\
&= \tfrac{2j}{\sigma^2}\gamma e^{-i \arctan(2\pi\sigma^2 k)}
\end{aligned} \tag{C.5}$$

$$\begin{aligned}
p_7 &= \sqrt{\tfrac{j}{2\sigma^2} - ij\pi k} \\
&= \sqrt{(\tfrac{j}{2\sigma^2})(1 - i2\pi\sigma^2 k)} \\
&= \sqrt{\tfrac{j}{2\sigma^2}}\sqrt{1 - i2\pi\sigma^2 k} \\
&= \sqrt{\tfrac{j}{2\sigma^2}}\sqrt{\sqrt{1 + (2\pi\sigma^2 k)^2} e^{i \arctan(\frac{-2\pi\sigma^2 k}{1})}} \\
&= \sqrt{\tfrac{j}{2\sigma^2}}(1 + 4\pi^2\sigma^4 k^2)^{\frac{1}{4}} e^{-i\frac{\arctan(2\pi\sigma^2 k)}{2}} \\
&= \sqrt{\tfrac{j}{2\sigma^2}}\sqrt{\gamma} e^{-i\frac{\arctan(2\pi\sigma^2 k)}{2}}
\end{aligned} \tag{C.6}$$

Three substitutions, p_8, p_9, and γ, are made in Equations C.3 - C.6. These substitutions are defined as

$$p_8 = -4\pi^2 f^2 + 8\pi^2 j f_0 f - j^2 4\pi^2 f_0^2 + \frac{j^2\mu^2}{\sigma^4} \tag{C.7}$$

$$p_9 = \frac{4\pi j^2 f_0 \mu}{\sigma^2} - \frac{4\pi j\mu f}{\sigma^2} \tag{C.8}$$

$$\gamma = \sqrt{1 + 4\pi^2\sigma^4 k^2} \tag{C.9}$$

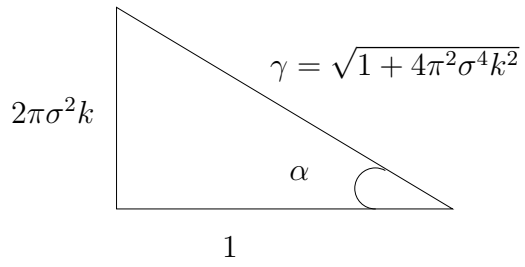

Fig. C.1. Right Triangle Where γ is the Length of the Hypothenuse.

Substitute back in p_4, p_5, p_6, and p_7 into $Y(f) = \sum_{j=1}^{M} \frac{p_4}{p_7} e^{\frac{p_5}{p_6}}$ to obtain

$$\begin{aligned} Y(f) &= \sum_{j=1}^{M} \frac{p_4}{p_7} e^{\frac{p_5}{p_6}} \\ &= \sum_{j=1}^{M} \frac{\sqrt{\pi} a_j (C_1)^j e^{\frac{-j\mu^2}{2\sigma^2}}}{\sqrt{\frac{j}{2\sigma^2}}\sqrt{\gamma} e^{-i\frac{\arctan(2\pi\sigma^2 k)}{2}}} e^{\frac{p_8 + ip_9}{\frac{2j}{\sigma^2}\gamma e^{-i\arctan(2\pi\sigma^2 k)}}} \\ &= \sum_{j=1}^{M} \frac{\sqrt{2\pi\sigma^2} a_j (C_1)^j e^{\frac{-j\mu^2}{2\sigma^2}} e^{i\frac{\arctan(2\pi\sigma^2 k)}{2}}}{\sqrt{j\gamma}} e^{\frac{\sigma^2[p_8 + ip_9]e^{i\arctan(2\pi\sigma^2 k)}}{2j\gamma}} \end{aligned}$$

$Y(f)$ is now rewritten as

$$Y(f) = \frac{\sqrt{2\pi\sigma^2} e^{i\frac{\arctan(2\pi\sigma^2 k)}{2}}}{\sqrt{\gamma}} \sum_{j=1}^{M} \frac{a_j (C_1)^j e^{\frac{-j\mu^2}{2\sigma^2}}}{\sqrt{j}} e^{\frac{\sigma^2[p_8 + ip_9]e^{i\arctan(2\pi\sigma^2 k)}}{2j\gamma}} \tag{C.10}$$

The expression $e^{i\arctan(2\pi\sigma^2 k)}$ in Equation C.10 will be rewritten below using Euler's formula [117]. Let $\alpha = \arctan(2\pi\sigma^2 k)$ thereby $e^{i\arctan(2\pi\sigma^2 k)} = e^{i\alpha}$. α can be conceptualized as an angle in a right triangle as shown by Figure C.1. The length of the hypothenuse in this triangle is γ. Therefore $\cos[\alpha] = \frac{1}{\gamma}$ and $\sin[\alpha] = \frac{2\pi\sigma^2 k}{\gamma}$. Using these facts, $e^{i\arctan(2\pi\sigma^2 k)}$ is becomes

$$\begin{aligned} e^{i\arctan(2\pi\sigma^2 k)} &= e^{i\alpha} \\ &= \cos[\alpha] + i\sin[\alpha] \\ &= \frac{1}{\gamma} + i\frac{2\pi\sigma^2 k}{\gamma} \end{aligned}$$

Substituting this into Equation C.10 produces

$$
\begin{aligned}
Y(f) &= \frac{\sqrt{2\pi\sigma^2}e^{i\frac{\arctan(2\pi\sigma^2 k)}{2}}}{\sqrt{\gamma}} \sum_{j=1}^{M} \frac{a_j (C_1)^j e^{\frac{-j\mu^2}{2\sigma^2}}}{\sqrt{j}} e^{\frac{\sigma^2[p_8+ip_9]e^{i\arctan(2\pi\sigma^2 k)}}{2j\gamma}} \\
&= \frac{\sqrt{2\pi\sigma^2}e^{i\frac{\arctan(2\pi\sigma^2 k)}{2}}}{\sqrt{\gamma}} \sum_{j=1}^{M} \frac{a_j (C_1)^j e^{\frac{-j\mu^2}{2\sigma^2}}}{\sqrt{j}} e^{\frac{\sigma^2[p_8+ip_9][\frac{1}{\gamma}+i\frac{2\pi\sigma^2 k}{\gamma}]}{2j\gamma}} \\
&= \frac{\sqrt{2\pi\sigma^2}e^{i\frac{\arctan(2\pi\sigma^2 k)}{2}}}{\sqrt{\gamma}} \sum_{j=1}^{M} \frac{a_j (C_1)^j e^{\frac{-j\mu^2}{2\sigma^2}}}{\sqrt{j}} e^{\frac{\sigma^2(p_8-p_9 2\pi\sigma^2 k)}{2j\gamma^2}} e^{\frac{i(2\pi\sigma^2 k p_8+p_9)\sigma^2}{2j\gamma^2}}
\end{aligned}
$$

Substituting the expressions of p_8 and p_9 into the magnitude of the above yields

$$
\begin{aligned}
Y(f) &= \frac{\sqrt{2\pi\sigma^2}e^{i\frac{\arctan(2\pi\sigma^2 k)}{2}}}{\sqrt{\gamma}}\sum_{j=1}^{M}\frac{a_j(C_1)^j e^{-\frac{j\mu^2}{2\sigma^2}}}{\sqrt{j}} e^{\frac{\sigma^2(p_8-p_9 2\pi\sigma^2 k)}{2j\gamma^2}} e^{\frac{i(2\pi\sigma^2 k p_8+p_9)\sigma^2}{2j\gamma^2}} \\
&= \frac{\sqrt{2\pi\sigma^2}e^{i\frac{\arctan(2\pi\sigma^2 k)}{2}}}{\sqrt{\gamma}}\sum_{j=1}^{M}\frac{a_j(C_1)^j e^{-\frac{j\mu^2}{2\sigma^2}}}{\sqrt{j}} \\
&\quad e^{\frac{\sigma^2([-4\pi^2 f^2+8\pi^2 j f_0 f-j^2 4\pi^2 f_0^2+\frac{j^2\mu^2}{\sigma^4}]-[\frac{4\pi j^2 f_0\mu}{\sigma^2}-\frac{4\pi j\mu f}{\sigma^2}]2\pi\sigma^2 k)}{2j\gamma^2}} e^{\frac{i(2\pi\sigma^2 k p_8+p_9)\sigma^2}{2j\gamma^2}} \\
&= \frac{\sqrt{2\pi\sigma^2}e^{i\frac{\arctan(2\pi\sigma^2 k)}{2}}}{\sqrt{\gamma}}\sum_{j=1}^{M}\frac{a_j(C_1)^j e^{-\frac{j\mu^2}{2\sigma^2}}}{\sqrt{j}}[e^{\frac{-2\pi^2\sigma^2 f^2}{j\gamma^2}} e^{\frac{4\pi^2 f_0\sigma^2 f}{\gamma^2}} \\
&\quad e^{\frac{4\pi^2\mu k\sigma^2 f}{\gamma^2}} e^{\frac{-2\pi^2\sigma^2 j f_0^2}{\gamma^2}} e^{\frac{j\mu^2}{2\sigma^2\gamma^2}} e^{\frac{-4\pi^2\sigma^2 k\mu f_0 j}{\gamma^2}}] e^{\frac{i(2\pi\sigma^2 k p_8+p_9)\sigma^2}{2j\gamma^2}} \\
&= \frac{\sqrt{2\pi\sigma^2}e^{i\frac{\arctan(2\pi\sigma^2 k)}{2}}}{\sqrt{\gamma}}\sum_{j=1}^{M}\frac{a_j(C_1)^j e^{-\frac{j\mu^2}{2\sigma^2}}}{\sqrt{j}}[e^{\frac{j\mu^2}{2\sigma^2\gamma^2}-\frac{4\pi^2\sigma^2 k\mu f_0 j}{\gamma^2}-\frac{2\pi^2\sigma^2 j f_0^2}{\gamma^2}}] \\
&\quad [e^{\frac{-2\pi^2\sigma^2(f^2-2jf_0 f-2j\mu k f)}{j\gamma^2}}] e^{\frac{i(2\pi\sigma^2 k p_8+p_9)\sigma^2}{2j\gamma^2}} \\
&= \frac{\sqrt{2\pi\sigma^2}e^{i\frac{\arctan(2\pi\sigma^2 k)}{2}}}{\sqrt{\gamma}}\sum_{j=1}^{M}\frac{a_j(C_1)^j e^{-\frac{j\mu^2}{2\sigma^2}}}{\sqrt{j}}[e^{\frac{j\mu^2}{2\sigma^2\gamma^2}-\frac{4\pi^2\sigma^2 k\mu f_0 j}{\gamma^2}-\frac{2\pi^2\sigma^2 j f_0^2}{\gamma^2}}] \\
&\quad [e^{\frac{-2\pi^2\sigma^2(f^2-(2f_0 j+2j\mu k)f+[-jf_0-j\mu k]^2-[-jf_0-j\mu k]^2)}{j\gamma^2}}] e^{\frac{i(2\pi\sigma^2 k p_8+p_9)\sigma^2}{2j\gamma^2}} \\
&= \frac{\sqrt{2\pi\sigma^2}e^{i\frac{\arctan(2\pi\sigma^2 k)}{2}}}{\sqrt{\gamma}}\sum_{j=1}^{M}\frac{a_j(C_1)^j e^{-\frac{j\mu^2}{2\sigma^2}}}{\sqrt{j}}[e^{\frac{j\mu^2}{2\sigma^2\gamma^2}-\frac{4\pi^2\sigma^2 k\mu f_0 j}{\gamma^2}-\frac{2\pi^2\sigma^2 j f_0^2}{\gamma^2}}] \\
&\quad [e^{\frac{-2\pi^2\sigma^2(f^2-(2f_0 j+2j\mu k)f+[-jf_0-j\mu k]^2)}{j\gamma^2}} e^{\frac{2\pi^2\sigma^2[-jf_0-j\mu k]^2}{j\gamma^2}}] e^{\frac{i(2\pi\sigma^2 k p_8+p_9)\sigma^2}{2j\gamma^2}} \\
&= \frac{\sqrt{2\pi\sigma^2}e^{i\frac{\arctan(2\pi\sigma^2 k)}{2}}}{\sqrt{\gamma}}\sum_{j=1}^{M}\frac{a_j(C_1)^j e^{-\frac{j\mu^2}{2\sigma^2}}}{\sqrt{j}}[e^{\frac{j\mu^2}{2\sigma^2\gamma^2}-\frac{4\pi^2\sigma^2 k\mu f_0 j}{\gamma^2}-\frac{2\pi^2\sigma^2 j f_0^2}{\gamma^2}}] \\
&\quad [e^{\frac{-2\pi^2\sigma^2(f-jf_0-j\mu k)^2}{j\gamma^2}} e^{\frac{2\pi^2\sigma^2 j(f_0+\mu k)^2}{\gamma^2}}] e^{\frac{i(2\pi\sigma^2 k p_8+p_9)\sigma^2}{2j\gamma^2}}
\end{aligned}
$$

For simplicity, two substitutions are made to the above expression

$$C_2 = \frac{\sqrt{2\pi\sigma^2}e^{\frac{i\arctan(2\pi\sigma^2 k)}{2}}}{\sqrt{\gamma}} \tag{C.11}$$

$$C_3(j) = \frac{a_j(C_1)^j e^{-\frac{j\mu^2}{2\sigma^2}}}{\sqrt{j}} e^{\frac{j\mu^2}{2\sigma^2\gamma^2}} e^{\frac{-4\pi^2\sigma^2 k\mu f_0 j}{\gamma^2}} e^{\frac{2\pi^2\sigma^2 j(f_0+\mu k)^2}{\gamma^2}} e^{\frac{-2\pi^2\sigma^2 j f_0^2}{\gamma^2}} \tag{C.12}$$

C_2 is a constant variable and $C_3(j)$ is a function dependent on the nonlinearity of order M. Substituting C_2 and $C_3(j)$ into the above expression produces

$$Y(f) = C_2 \sum_{j=1}^{M} C_3(j) e^{\frac{-2\pi^2\sigma^2(f-jf_0-j\mu k)^2}{j\gamma^2}} e^{\frac{i(2\pi\sigma^2 p_8 + p_9)\sigma^2}{2j\gamma^2}}$$

Substituting in the expressions for p_8 and p_9 into the phase component of $Y(f)$ produces

$$
\begin{aligned}
Y(f) &= C_2 \sum_{j=1}^{M} C_3(j) e^{\frac{-2\pi^2\sigma^2(f-jf_0-j\mu k)^2}{j\gamma^2}} e^{\frac{i(2\pi\sigma^2 k p_8+p_9)\sigma^2}{2j\gamma^2}} \\
&= C_2 \sum_{j=1}^{M} C_3(j) e^{\frac{-2\pi^2\sigma^2(f-jf_0-j\mu k)^2}{j\gamma^2}} \\
&\quad e^{\frac{i(2\pi\sigma^2 k[-4\pi^2 f^2+8\pi^2 jf_0 f-j^2 4\pi^2 f_0^2+\frac{j^2\mu^2}{\sigma^4}]+[\frac{4\pi j^2 f_0\mu}{\sigma^2}-\frac{4\pi j\mu f}{\sigma^2}])\sigma^2}{2j\gamma^2}} \\
&= C_2 \sum_{j=1}^{M} C_3(j) e^{\frac{-2\pi^2\sigma^2(f-jf_0-j\mu k)^2}{j\gamma^2}} \\
&\quad [e^{\frac{-i4\pi^3\sigma^4 kf^2}{j\gamma^2}} e^{\frac{i8\pi^3\sigma^4 kf_0 f}{\gamma^2}} e^{\frac{-ijk4\pi^3\sigma^4 f_0^2}{\gamma^2}} e^{\frac{ijk\pi\mu^2}{\gamma^2}} e^{\frac{i2\pi jf_0\mu}{\gamma^2}} e^{\frac{-i2\pi\mu f}{\gamma^2}}] \\
&= C_2 \sum_{j=1}^{M} C_3(j) e^{\frac{-2\pi^2\sigma^2(f-jf_0-j\mu k)^2}{j\gamma^2}} \\
&\quad [e^{\frac{ijk\pi\mu^2}{\gamma^2}-\frac{ijk4\pi^3\sigma^4 f_0^2}{\gamma^2}+\frac{i2\pi jf_0\mu}{\gamma^2}}][e^{\frac{-i4\pi^3\sigma^4 kf^2}{j\gamma^2}-\frac{i2\pi\mu jf}{j\gamma^2}+\frac{i8\pi^3\sigma^4 kf_0 jf}{j\gamma^2}}] \\
&= C_2 \sum_{j=1}^{M} C_3(j) e^{\frac{-2\pi^2\sigma^2(f-jf_0-j\mu k)^2}{j\gamma^2}} [e^{\frac{ijk\pi\mu^2}{\gamma^2}-\frac{ijk4\pi^3\sigma^4 f_0^2}{\gamma^2}+\frac{i2\pi jf_0\mu}{\gamma^2}}] \\
&\quad [e^{\frac{-i4\pi^3\sigma^4 k}{j\gamma^2}(f^2-2jf_0 f)-\frac{i2j\pi\mu f}{j\gamma^2}}] \\
&= C_2 \sum_{j=1}^{M} C_3(j) e^{\frac{-2\pi^2\sigma^2(f-jf_0-j\mu k)^2}{j\gamma^2}} [e^{\frac{ijk\pi\mu^2}{\gamma^2}-\frac{ijk4\pi^3\sigma^4 f_0^2}{\gamma^2}+\frac{i2\pi jf_0\mu}{\gamma^2}}] \\
&\quad [e^{\frac{-i4\pi^3\sigma^4 k}{j\gamma^2}(f^2-2jf_0 f+\frac{\mu jf}{2\pi^2\sigma^4 k})}] \\
&= C_2 \sum_{j=1}^{M} C_3(j) e^{\frac{-2\pi^2\sigma^2(f-jf_0-j\mu k)^2}{j\gamma^2}} [e^{\frac{ijk\pi\mu^2}{\gamma^2}-\frac{ijk4\pi^3\sigma^4 f_0^2}{\gamma^2}+\frac{i2\pi jf_0\mu}{\gamma^2}}] \\
&\quad [e^{\frac{-i4\pi^3\sigma^4 k}{j\gamma^2}(f^2-(2jf_0-\frac{\mu j}{2\pi^2\sigma^4 k})f+(-jf_0+\frac{\mu j}{4\pi^2\sigma^4 k})^2-(-jf_0+\frac{\mu j}{4\pi^2\sigma^4 k})^2)}] \\
&= C_2 \sum_{j=1}^{M} C_3(j) e^{\frac{-2\pi^2\sigma^2(f-jf_0-j\mu k)^2}{j\gamma^2}} [e^{\frac{ijk\pi\mu^2}{\gamma^2}-\frac{ijk4\pi^3\sigma^4 f_0^2}{\gamma^2}+\frac{i2\pi jf_0\mu}{\gamma^2}}] \\
&\quad [e^{\frac{-i4\pi^3\sigma^4 k}{j\gamma^2}(f+\frac{\mu j}{4\pi^2\sigma^4 k}-jf_0)^2} e^{i(\frac{4\pi^3\sigma^4 k}{j\gamma^2})(\frac{\mu j}{4\pi^2\sigma^4 k}-jf_0)^2}] \\
&= C_2 \sum_{j=1}^{M} C_3(j) e^{\frac{-2\pi^2\sigma^2(f-jf_0-j\mu k)^2}{j\gamma^2}} e^{i[\frac{jk\pi\mu^2}{\gamma^2}-\frac{jk4\pi^3\sigma^4 f_0^2}{\gamma^2}+\frac{2\pi jf_0\mu}{\gamma^2}+(\frac{4\pi^3\sigma^4 k}{j\gamma^2})(\frac{\mu j}{4\pi^2\sigma^4 k}-jf_0)^2]} \\
&\quad e^{i[\frac{-4\pi^3\sigma^4 k}{j\gamma^2}(f+\frac{\mu j}{4\pi^2\sigma^4 k}-jf_0)^2]}
\end{aligned}
$$

For simplicity, three substitutions are made to the above expression

$$C_4(j) = \frac{jk\pi\mu^2}{\gamma^2} - \frac{jk4\pi^3\sigma^4 f_0^2}{\gamma^2} + \frac{2\pi j f_0 \mu}{\gamma^2} + \frac{4\pi^3\sigma^4 k}{j\gamma^2}(\frac{\mu j}{4\pi^2\sigma^4 k} - jf_0)^2 \tag{C.13}$$

$$\psi(j,f) = \frac{-4\pi^3\sigma^4 k}{j\gamma^2}(f + \frac{j\mu}{4\pi^2\sigma^4 k} - jf_0)^2 \tag{C.14}$$

$$\xi(j,f) = e^{\frac{-2\pi^2\sigma^2(f-jf_0-j\mu k)^2}{j\gamma^2}} \tag{C.15}$$

$C_4(j)$ is a function dependent on the nonlinearity of order M. Equations C.14 and C.15 are dependent on frequency and the nonlinearity of order M. It is of interest to note that $\xi(j,f)$ has a Gaussian form. Substituting these equations into $Y(f)$ produces

$$Y(f) = C_2 \sum_{j=1}^{M} [C_3(j)e^{iC_4(j)}]\xi(j,f)e^{i\psi(j,f)} \tag{C.16}$$

Note that Equation C.16 is equal to Equation 2.20 from Chapter 2.

D: Power Spectrum of the Gaussian Chirp Signal

The derivation of the power spectrum for a Gaussian chirp signal is shown here. The power spectrum of $Y(f)$ is realized by multiplying $Y(f)$ by its complex conjugate $Y(f)^*$. $Y(f)$ was derived in Appendix C and was defined by Equation C.16. $P_y(f)$ is

$$
\begin{aligned}
P_y(f) &= \{Y(f)\}\{Y^*(f)\} = \{C_2 \sum_{j=1}^{M} C_3(j)\xi(j,f)e^{iC_4(j)}e^{i\psi(j,f)}\} \\
&\quad \{C_2^* \sum_{l=1}^{M} C_3(l)\xi(l,f)e^{-iC_4(l)}e^{-i\psi(l,f)}\} \\
&= C_2C_2^*\{C_3(1)\xi(1,f)e^{iC_4(1)}e^{i\psi(1,f)} + ... + C_3(M)\xi(M,f)e^{iC_4(M)}e^{i\psi(M,f)}\} \\
&\quad \{C_3(1)\xi(1,f)e^{-iC_4(1)}e^{-i\psi(1,f)} + ... + C_3(M)\xi(M,f)e^{-iC_4(M)}e^{-i\psi(M,f)}\} \\
&= C_2C_2^*\{[C_3(1)\xi(1,f)]^2 + [C_3(1)C_3(2)\xi(1,f)\xi(2,f)] \\
&\quad e^{i[C_4(1)-C_4(2)+\psi(1,f)-\psi(2,f)]} + ... + [C_3(1)C_3(M)\xi(1,f)\xi(M,f)] \\
&\quad e^{i[C_4(1)-C_4(M)+\psi(1,f)-\psi(M,f)]} \\
&\quad +... + \\
&\quad ... \\
&\quad +... + \\
&\quad +[C_3(M)C_3(1)\xi(M,f)\xi(1,f)]e^{i[C_4(M)-C_4(1)+\psi(M,f)-\psi(1,f)]} \\
&\quad +... + [C_3(M)\xi(M,f)]^2\}
\end{aligned}
$$

There exists a total of M^2 terms that are summed together. Define a square-term as any term in $Y(f)$ of order j that is multiplied by a term of the same order (i.e., $l = j$) in $Y^*(f)$. Note that there is no phase component for a square-term. For example, when $j = l$, a square-term would be $[C_3(j)C_3(l)\xi(j,f)\xi(l,f)]e^{i[C_4(j)-C_4(l)+\psi(j,f)-\psi(l,f)]}$ $= [C_3(j)C_3(j)\xi(j,f)\xi(j,f)]e^{i[C_4(j)-C_4(j)+\psi(j,f)-\psi(j,f)]} = [C_3(j)\xi(j,f)]^2$. There exists M

square-terms. The set of square-terms is $\{[C_3(1)\xi(1,f)]^2$, $[C_3(2)\xi(2,f)]^2$, ... $[C_3(M)\xi(M,f)]^2\}$. Define a cross-term as any term in $Y(f)$ of order j multiplied by a term of a different order ($l \neq j$) in $Y^*(f)$. There exists a magnitude and phase component for a cross-term. An example of a cross-term is $[C_3(j)C_3(l)\xi(j,f)\xi(l,f)]$ $e^{i[C_4(j)-C_4(l)+\psi(j,f)-\psi(l,f)]}$. Since there exists M square-terms, the number of cross-terms is $M^2 - M = M(M-1)$. The set of cross-terms is $\{C_3(1)\ C_3(2)\ \xi(1,f)\ \xi(2,f)\ e^{i[C_4(1)-C_4(2)+\psi(1,f)-\psi(2,f)]}$, $C_3(1)\ C_3(3)\ \xi(1,f)\ \xi(3,f)\ e^{i[C_4(1)-C_4(3)+\psi(1,f)-\psi(3,f)]}$, ... $C_3(M)C_3(M-1)\xi(M,f)\xi(M-1,f)e^{i[C_4(M)-C_4(M-1)+\psi(M,f)-\psi(M-1,f)]}\}$.

To simplify the power spectrum, let the function $W(j,l,f)$ be

$$W(j,l,f) = C_3(j)C_3(l)\xi(j,f)\xi(l,f) \tag{D.1}$$

This Equation replaces the magnitude components in $P_y(f)$. In addition, define the function $Q(j,l,f)$ as

$$Q(j,l,f) = C_4(j) - C_4(l) + \psi(j,f) - \psi(l,f) \tag{D.2}$$

This Equation replaces the phase components in $P_y(f)$. The following Lemma's are used to denote properties of $W(j,l,f)$ and $Q(j,l,f)$.

Lemma 1 (Gaussian Power Spectrum Lemma 1) *Let $W(j,l,f)$ be the function defined by Equation D.1. A property of this function is that $W(j,l,f) = W(l,j,f)$.*

Proof $W(j,l,f) = C_3(j)C_3(l)\xi(j,f)\xi(l,f) = C_3(l)C_3(j)\xi(l,f)\xi(j,f) = W(l,j,f)$ ■

Lemma 2 (Gaussian Power Spectrum Lemma 2) *Let $Q(j,l,f)$ be the function defined by Equation D.2. A property of this function is that $Q(j,l,f) = -Q(l,j,f)$.*

Proof $Q(j,l,f) = C_4(j) - C_4(l) + \psi(j,f) - \psi(l,f) = -[-C_4(j) + C_4(l) - \psi(j,f) + \psi(l,f)] = -[C_4(l) - C_4(j) + \psi(l,f) - \psi(j,f)] = -Q(l,j,f)$ ■

Note that $W(j,j,f)$ and $W(l,l,f)$ are square-terms and $W(j,l,f)e^{iQ(j,l,f)}$ and $W(l,j,f)e^{iQ(l,j,f)}$ are cross-terms. Substituting $W(j,l,f)$ and $Q(j,l,f)$ into $P_y(f)$ produces

$$
\begin{aligned}
P_y(f) &= C_2C_2^*\{[C_3(1)\xi(1,f)]^2 \\
&\quad +[C_3(1)C_3(2)\xi(1,f)\xi(2,f)]e^{i[C_4(1)-C_4(2)+\psi(1,f)-\psi(2,f)]} \\
&\quad +... + [C_3(1)C_3(M)\xi(1,f)\xi(M,f)]e^{i[C_4(1)-C_4(M)+\psi(1,f)-\psi(M,f)]} \\
&\quad +... + \\
&\quad ... \\
&\quad +... + \\
&\quad +[C_3(M)C_3(1)\xi(M,f)\xi(1,f)]e^{i[C_4(M)-C_4(1)+\psi(M,f)-\psi(1,f)]} \\
&\quad +... + [C_3(M)\xi(M,f)]^2\} \\
&= C_2C_2^*\{W(1,1,f) + W(1,2,f)e^{iQ(1,2,f)} + ... + W(1,M,f)e^{iQ(1,M,f)} \\
&\quad +... + \\
&\quad ... \\
&\quad +... + \\
&\quad +W(M,1,f)e^{iQ(M,1,f)} + ... + W(M,M,f)\}
\end{aligned}
$$

Grouping the square-terms and cross-terms produces

$$
\begin{aligned}
P_y(f) &= C_2C_2^*\{[W(1,1,f)+...+W(M,M,f)] \\
&\quad +[W(1,2,f)e^{iQ(1,2,f)}+...+W(1,M,f)e^{iQ(1,M,f)} \\
&\quad +W(2,1,f)e^{iQ(2,1,f)}+W(2,3,f)e^{iQ(2,3,f)}+...+W(2,M,f)e^{iQ(2,M,f)} \\
&\quad +... + \\
&\quad ... \\
&\quad +... + \\
&\quad +W(M,1,f)e^{iQ(M,1,f)}+W(M,2,f)e^{iQ(M,2,f)} \\
&\quad +...+W(M,M-1,f)e^{iQ(M,M-1,f)}]\} \\
&= C_2C_2^*\{[\sum_{j=1}^{M}W(j,j,f)]+ \\
&\quad [W(1,2,f)e^{iQ(1,2,f)}+W(2,1,f)e^{iQ(2,1,f)}]+[W(1,3,f)e^{iQ(1,3,f)} \\
&\quad +W(3,1,f)e^{iQ(3,1,f)}] \\
&\quad +...+[W(1,M,f)e^{iQ(1,M,f)}+W(M,1,f)e^{iQ(M,1,f)}] \\
&\quad +[W(2,3,f)e^{iQ(2,3,f)}+W(3,2,f)e^{iQ(3,2,f)}]+[W(2,4,f)e^{iQ(2,4,f)} \\
&\quad +W(4,2,f)e^{iQ(4,2,f)}] \\
&\quad +...+[W(2,M,f)e^{iQ(2,M,f)}+W(M,2,f)e^{iQ(M,2,f)}] \\
&\quad +... + \\
&\quad ... \\
&\quad +... + \\
&\quad +[W(M-1,M,f)e^{iQ(M-1,M,f)}+W(M,M-1,f)e^{iQ(M,M-1,f)}]\}
\end{aligned}
$$

Using Lemmas 1 and 2 produces

$$
\begin{aligned}
P_y(f) &= C_2C_2^*\{[\sum_{j=1}^{M} W(j,j,f)] + \\
&\quad [W(1,2,f)e^{iQ(1,2,f)} + W(1,2,f)e^{-iQ(1,2,f)}] + [W(1,3,f)e^{iQ(1,3,f)} \\
&\quad + W(1,3,f)e^{-iQ(1,3,f)}] \\
&\quad + ... + [W(1,M,f)e^{iQ(1,M,f)} + W(1,M,f)e^{-iQ(1,M,f)}] \\
&\quad + [W(2,3,f)e^{iQ(2,3,f)} + W(2,3,f)e^{-iQ(2,3,f)}] + [W(2,4,f)e^{iQ(2,4,f)} \\
&\quad + W(2,4,f)e^{-iQ(2,4,f)}] \\
&\quad + ... + [W(2,M,f)e^{iQ(2,M,f)} + W(2,M,f)e^{-iQ(2,M,f)}] \\
&\quad + ... + \\
&\quad ... \\
&\quad + ... + \\
&\quad + [W(M-1,M,f)e^{iQ(M-1,M,f)} + W(M-1,M,f)e^{-iQ(M-1,M,f)}]\} \\
&= C_2C_2^*\{[\sum_{j=1}^{M} W(j,j,f)] \\
&\quad + [\sum_{j=1}^{M-1}\sum_{l=j+1}^{M} (W(j,l,f)e^{iQ(j,l,f)} + W(j,l,f)e^{-iQ(j,l,f)})]\} \\
&= C_2C_2^*\{[\sum_{j=1}^{M} W(j,j,f)] + [\sum_{j=1}^{M-1}\sum_{l=j+1}^{M} 2W(j,l,f)\cos(Q(j,l,f))]\}
\end{aligned}
$$

Substituting the definitions of $W(j,l,f)$ and $Q(j,l,f)$ into the above

$$
\begin{aligned}
&Py(f) = C_2C_2^*\{\sum_{j=1}^{M}[C_3(j)\xi(j,f)]^2 + \\
&\sum_{j=1}^{M-1}\sum_{l=j+1}^{M} 2C_3(j)C_3(l)\xi(j,f)\xi(l,f)\cos(C_4(j) - C_4(l) + \psi(j,f) - \psi(l,f))\}
\end{aligned}
\tag{D.3}
$$

Note that Equation D.3 is equal to Equation 2.28 from Chapter 2.

If minimal overlap exists between the Gaussian functions in the cross-terms, then a minimal amount of interference is generated. A minimal overlap condition is defined as

$$\xi(j,f)\xi(l,f) = \epsilon \tag{D.4}$$

where $\epsilon \simeq 0$, and $l > j$. Equation D.4 is considered at the intercept point $f = f_{int}$. At $f = f_{int}$, $\xi(j, f_{int}) = \xi(l, f_{int})$. Then the following reduction can be made.

$$e^{\frac{-(f_{int}-\mu_\xi(j))^2}{2(\sigma_\xi(j))^2}} = e^{\frac{-(f_{int}-\mu_\xi(l))^2}{2(\sigma_\xi(l))^2}}$$

$$\frac{-(f_{int}-\mu_\xi(j))^2}{2(\sigma_\xi(j))^2} = \frac{-(f_{int}-\mu_\xi(l))^2}{2(\sigma_\xi(l))^2}$$

Note that $\mu_\xi(j) < f_{int} < \mu_\xi(l)$.

$$\frac{(f_{int}-\mu_\xi(j))}{\sqrt{2}\sigma_\xi(j)} = \frac{(f_{int}-\mu_\xi(l))}{\sqrt{2}\sigma_\xi(l)}$$

$$\frac{(f_{int}-\mu_\xi(j))}{\sqrt{2}\sigma_\xi(j)} = \frac{(f_{int}-\mu_\xi(l))}{\sqrt{2}\sigma_\xi(l)}$$

$$\frac{f_{int}}{\sigma_\xi(j)} - \frac{\mu_\xi(j)}{\sigma_\xi(j)} = \frac{\mu_\xi(l)}{\sigma_\xi(l)} - \frac{f_{int}}{\sigma_\xi(l)}$$

$$\frac{f_{int}}{\sigma_\xi(j)} + \frac{f_{int}}{\sigma_\xi(l)} = \frac{\mu_\xi(j)}{\sigma_\xi(j)} + \frac{\mu_\xi(l)}{\sigma_\xi(l)} = \frac{\mu_\xi(j)\sigma_\xi(l) + \mu_\xi(l)\sigma_\xi(j)}{\sigma_\xi(l)\sigma_\xi(j)}$$

$$\frac{f_{int}\sigma_\xi(j) + f_{int}\sigma_\xi(l)}{\sigma_\xi(l)\sigma_\xi(j)} = \frac{\mu_\xi(j)\sigma_\xi(l) + \mu_\xi(l)\sigma_\xi(j)}{\sigma_\xi(l)\sigma_\xi(j)}$$

f_{int} therefore equals

$$f_{int} = \frac{\mu_\xi(l)\sigma_\xi(j) + \mu_\xi(j)\sigma_\xi(l)}{\sigma_\xi(j) + \sigma_\xi(l)} \tag{D.5}$$

If $f = f_{int}$, then Equation D.4 reduces to the following

$$e^{\frac{-(f_{int}-\mu_\xi(j))^2}{2(\sigma_\xi(j))^2}} e^{\frac{-(f_{int}-\mu_\xi(l))^2}{2(\sigma_\xi(l))^2}} = \epsilon$$

$$\frac{-(f_{int}-\mu_\xi(j))^2}{2(\sigma_\xi(j))^2} - \frac{(f_{int}-\mu_\xi(l))^2}{2(\sigma_\xi(l))^2} = ln(\epsilon)$$

where $ln()$ is the natural log.

$$\begin{aligned} ln(\epsilon) &= \frac{-(f_{int}-\mu_\xi(j))^2}{2\sigma_\xi(j)^2} - \frac{(f_{int}-\mu_\xi(l))^2}{2\sigma_\xi(l)^2} \\ &= \frac{-(f_{int}^2 - 2\mu_\xi(j)f_{int} + \mu_\xi(j)^2)}{2\sigma_\xi(j)^2} - \frac{(f_{int}^2 - 2\mu_\xi(l)f_{int} + \mu_\xi(l)^2)}{2\sigma_\xi(l)^2} \\ &= \frac{-2(\sigma_\xi(j)^2 + \sigma_\xi(l)^2)f_{int}^2}{4\sigma_\xi(l)^2\sigma_\xi(j)^2} + \frac{4(\mu_\xi(j)\sigma_\xi(l)^2 + \mu_\xi(l)\sigma_\xi(j)^2)f_{int}}{4\sigma_\xi(l)^2\sigma_\xi(j)^2} + \\ &\quad \frac{-2(\mu_\xi(j)^2\sigma_\xi(l)^2 + \mu_\xi(l)^2\sigma_\xi(j)^2)}{4\sigma_\xi(l)^2\sigma_\xi(j)^2} \end{aligned}$$

Substituting f_{int} from Equation D.5 into the above reduces to

$$\frac{(\mu_\xi(l) - \mu_\xi(j))}{(\sigma_\xi(j) + \sigma_\xi(l))} = \sqrt{\frac{1}{\epsilon}} \tag{D.6}$$

Note that Equation D.6 is equal to Equation 2.37 from Chapter 2.

VITA

VITA

Anthony Frank Martone was born in Denville, New Jersey. He received the AS and AAS in 1999 at the County College of Morris in Randolph, New Jersey where he won the Phi Theta Kappa Award. He received the BS degree at Rensselaer Polytechnic Institute where he graduated first in his class with a 4.0/4.0 grade point average. His research interests included automatic control systems and robotics. While at Rensselaer, he received the Joseph H. Smith Scholarship, the 4.0 Award, and was a member of the National Dean's List eight times.

Since 2002, Anthony has studied in the direct Ph.D. program at Purdue University in West Lafayette, Indiana, where he received a one year graduate fellowship. He has worked as a research assistant for Professor Edward Delp, the Silicon Valley Professor of Electrical and Computer Engineering. From 2002 - 2005, he was supported by a project funded by the C-SPAN Archives located in West Lafayette, Indiana. During this time, he developed video and text analysis tools for the Archives. In the Spring 2004, Anthony and his four member team placed fifth among 50 competitors at the Burton D. Morgan Entrepreneur Business Competition in West Lafayette, Indiana. From 2005 - 2007, he was supported by a project funded by the U.S. Army MURI program. During this time, he developed methods to identify RF devices. In the Spring 2007, Anthony was a member of a three person team that entered the CERIAS Research Poster Competition, winning first place.

During his Ph.D. studies, Anthony has worked at the Army Research Labs (ARL) in Adelphi, Maryland. While at ARL, he developed tools to extract features of moving targets from synthetic aperture radar (SAR) images and designed classification systems to classify the features.

Journal Papers:

1. A.F. Martone and E.J. Delp, "Transcript Synchronization Using Local Dynamic Programming," IEEE Transactions on Multimedia (Pending Review).
2. A.F. Martone and E.J. Delp, "RF Fingerprinting Using Linear Chirp Signals," IEEE Transactions on Microwave Theory and Techniques (Pending Review).

Conference Papers:

1. A.F. Martone and E.J. Delp, "Characterization of RF Devices using Two-Tone Probe Signals," in Proceedings of the 2007 IEEE Workshop on Statistical Signal Processing, Madison, WI, August 2007.
2. K. Ranney, A. Martone, and M. Soumekh, "Indication of Slowly Moving Targets via Change Detection," in Proceedings of the SPIE Conference on Radar Sensor Technology XI, Orlando, Fl, April 2007, Volume 6547 - 65470L.
3. N. Khanna, A.K. Mikkilineni, A.F. Martone, G.N. Ali, G.T.C. Chiu, J.P. Allebach, and E.J. Delp, "A Survey of Forensic Characterization Methods for Physical Devices," in Proceedings of the 6th Workshop on Digital Forensics Research, Lafayette, Indiana, August 2006, pp. 17-28.
4. A.F. Martone, A.K. Mikkilineni, and E.J. Delp, "Forensics of things," in Proceedings of the 2006 IEEE Southwest Symposium on Image Analysis and Interpretation, Denver, Colorado, March 2006, pp. 149-152.
5. A.F. Martone and E.J. Delp, "Forensic characterization of RF circuits," in Proceedings of Government Microcircuit Applications and Critical Technology Conference 06 (GOMACTech06), San Diego, California, March 2006, pp. 224-227.
6. A.F. Martone and E.J. Delp, "An Overview of the Use of Closed Caption Information for Video Indexing and Searching," in Proceedings of the 4th International Workshop on Content-Based Multimedia Indexing (CBMI), Riga, Latvia, June 21-23, 2005.

7. A.F. Martone, C. Taskiran, and E.J. Delp, "Multimodal Approach for Speaker Identification in News Programs," in Proceedings of the SPIE International Conference on Storage and Retrieval Methods and Applications for Multimedia, San Jose, CA, January 2005.

8. A. Martone, C. Taskiran, R. Browning, and E. Delp, "A Toolset for Broadcast Automation for the C-SPAN Networks," in Proceedings of the 5th International Workshop on Image Analysis for Multimedia Interactive Services (WIAMIS), Lisbon, Portugal, April 21-23, 2004.

9. A.F. Martone, C. Taskiran, and E.J. Delp, "Automated closed-captioning using text alignment," in Proceedings of the SPIE International Conference on Storage and Retrieval Methods and Applications for Multimedia, San Jose, CA, Jan. 20-22, 2004, pp. 108-116.